

ISOTOPIC COMPOSITION OF
GADOLINIUM, SAMARIUM AND EUROPIUM
IN THE ABEE METEORITE

by

ARTHUR JOHN LOVELESS

B.Sc., The University of Toronto, 1966
M.Sc., The University of Toronto, 1967

A THESIS SUBMITTED IN PARTIAL FULFILMENT OF
THE REQUIREMENTS FOR THE DEGREE OF

DOCTOR OF PHILOSOPHY

in the Department
of
GEOPHYSICS

We accept this thesis as conforming to the
required standard

THE UNIVERSITY OF BRITISH COLUMBIA

October, 1970

In presenting this thesis in partial fulfilment of the requirements for an advanced degree at the University of British Columbia, I agree that the Library shall make it freely available for reference and Study.

I further agree that permission for extensive copying of this thesis for scholarly purposes may be granted by the Head of my Department or by his representatives. It is understood that copying or publication of this thesis for financial gain shall not be allowed without my written permission.

Department of Geophysics

The University of British Columbia
Vancouver 8, Canada

Date Oct. 27, 1970

ABSTRACT

The writer has measured the isotopic composition of gadolinium, europium and samarium in the Abee meteorite and in two terrestrial ores. Gd, Eu and Sm have large thermal neutron capture cross sections; they may therefore be used to reveal differences in the irradiation histories of samples containing trace amounts of these elements. It is widely believed that the contracting protosun passed through a phase of high energy particle radiation during the early history of the solar system. The interaction of these particles with the material of the solar nebula may have produced a large thermal neutron flux.

The Abee enstatite chondrite is representative of the most highly reduced class of chondritic meteorites. The chondrites are stones which are thought to be very primitive material of the solar system. Mason, Miyashiro and others have proposed that variations in the oxidation state of chondrites result from their formation in different regions of the nebula: the enstatite chondrites represent material which was derived from the hot inner region of the solar nebula, while the highly oxidized carbonaceous chondrites had their origin in the cooler, outer region. On the basis of this theory, the earth was probably derived from an intermediate region of the nebula.

Isotopic analyses were performed on microgram quantities of Gd, Eu and Sm. A precision of 0.02-0.2% (at the 95% confidence level) was achieved for all isotopic ratios of interest. Prior to 1970 the best published isotopic analyses of these elements had a precision of 1-2%. The higher precision reported here was made possible through improvements in the mass spectrometer ion optics and the use of digital recording of mass spectra. This work is comparable to recent meteorite analyses on Gd by Eugster, Tera, Burnett and Wasserburg at the California Institute of Technology, although their lunar analyses were of superior quality and had a precision of 0.01%.

No significant Gd, Eu or Sm isotopic anomalies were observed for the Abee and terrestrial samples. The Gd^{157}/Gd^{158} ratio, which is the most sensitive to neutron irradiation, was identical for the three samples studied within 0.1%. This places an upper limit of 3×10^{15} neutrons/cm² for the differential irradiation of the source material from which the earth and the Abee meteorite were derived. A similar conclusion was reported by the Caltech group. The absence of any anomalies may be attributed to uniform irradiation and dilution of the source material, efficient shielding inside large planetary bodies during the irradiation phase, the absence of an intense irradiation phase, or a common spatial origin within the solar nebula for chondritic and terrestrial matter.

TABLE OF CONTENTS

ABSTRACT	ii
TABLE OF CONTENTS	iv
LIST OF FIGURES	vii
LIST OF TABLES	ix
ACKNOWLEDGEMENTS	x
CHAPTER 1. INTRODUCTION	1
1.1 Chondrites - Remnants of Primitive Planetary Material	1
1.2 Quantization of the Oxidation State of Chondrites	2
1.3 High Energy Particle Irradiation and its Consequences	8
1.4 Delineation of the Present Study	13
CHAPTER 2. A REVIEW OF THE EVIDENCE CON- CERNING IRRADIATION ANOMALIES	18
2.1 Synthesis of the Elements and High Energy Particle Irradiation	18
2.2 A Review of the Search for Irradiation Anomalies	21
2.3 The Effect of Recent Cosmic Irradiation	29
CHAPTER 3. INSTRUMENTATION	32
3.1 Operational Principles of a Mass Spectrometer	32
3.2 Ion Optics	34
3.3 The Ionization Process	38

3.4 Digital Recording of Mass Spectra	42
3.5 Noise Rejection Using a Low-Pass Filter	45
CHAPTER 4. PREPARATION OF SAMPLES	47
4.1 Separation of the Rare Earth Elements	47
4.2 Preparation of Filaments	55
4.3 Production of Ion Spectra with Minimum Interference	57
CHAPTER 5. COMPUTER REDUCTION OF COMPLEX SPECTRA	59
5.1 Evaluation of Peak Heights	59
5.2 Least Squares Reduction of a Set of Scans	61
5.3 Calculation of Means and Standard Deviations of Isotopic Ratios for a Set of Scans	68
5.4 Calculation of Fractionation - Corrected Parameters	71
5.5 Correction for the Isotopic Composition of Oxygen	76
CHAPTER 6. INTERPRETATION OF METEORITIC & TERRESTRIAL ISOTOPIC RATIOS	78
6.1 Terrestrial Gadolinium	78
6.2 Gadolinium in the Abee Meteorite	84
6.3 Do Abee and Terrestrial Gadolinium have Similar Composition?	90
6.4 Interpretation of Europium Data	93
6.5 Interpretation of Samarium Data	95
6.6 Conclusions	99

APPENDIX I.	EFFECT OF NEUTRON CAPTURE ON GD, SM AND EU	102
APPENDIX II.	SECOND ORDER FOCUSING SHIMS	109
APPENDIX III.	MEASURED ISOTOPIC RATIOS FOR ALL GADOLINIUM ANALYSES	119
APPENDIX IV.	SLOPE OF THEORETICAL CORRELATION LINES FOR NEUTRON CAPTURE	129
BIBLIOGRAPHY		131

	Page
LIST OF FIGURES	
FIGURE 1-1 ABUNDANCES OF THE METALLIC ELEMENTS	3
FIGURE 1-2 OXIDIZED AND REDUCED IRON IN CHONDRITES	5
FIGURE 1-3 FREQUENCY OF OCCURRENCE VS OXIDATION STATE	5
FIGURE 1-4 THERMAL NEUTRON CAPTURE IN LUNAR GADOLINIUM	10
FIGURE 2-1 MODEL FOR WHICH 5% OF PRIMITIVE MATERIAL WAS IRRADIATED	24
FIGURE 2-2 UNIFORM IRRADIATION MODEL	25
FIGURE 3-1 CONTINUOUS SCANNING OVER THE GADOLINIUM SPECTRUM	35
FIGURE 3-2 ION BEAM PRODUCED BY NEW ION SOURCE	37
FIGURE 3-3 DISCONTINUOUS SCANNING OVER THE GADOLINIUM SPECTRUM	44
FIGURE 3-4 FREQUENCY RESPONSE OF DIGITAL FILTER	46
FIGURE 4-1 ELUTION CURVES FOR TB, GD, EU AND SM	54
FIGURE 5-1 SLOW DISCONTINUOUS SCANNING	60
FIGURE 5-2 POLYNOMIAL REPRESENTATION OF ION BEAM INTENSITY	65
FIGURE 5-3 MASS SPECTROMETER FRACTIONATION	73
FIGURE 6-1 ISOTOPIC ANALYSES ON TERRESTRIAL GADOLINIUM	80

	Page
FIGURE 6-2 CORRELATION BETWEEN B AND A FOR TERRESTRIAL GD	81
FIGURE 6-3 CORRELATION OF GD ISOTOPES IN METEORITES	88
FIGURE 6-4 CORRELATION BETWEEN A AND B IN METEORITES	89
FIGURE II-1 MODIFICATION OF MAIN ELECTROMAGNET TO ACCOMMODATE FOCUSING SHIMS	110
FIGURE II-2 FRINGING FIELD OF MAIN MAGNET	112
FIGURE II-3 CURVATURE OF SECOND ORDER FOCUSING SHIMS	114
FIGURE II-4 OPTIMUM CURVATURE OF SHIMS AS A FUNCTION OF BEAM DIVERGENCE	115
FIGURE II-5 PEAK SHAPE FOR TWO VALUES OF THE ANGULAR DIVERGENCE	116
FIGURE II-6 BEAM SPREADING AT THE COLLECTOR FOR FIRST AND SECOND ORDER FOCUSING	118

	Page
LIST OF TABLES	
TABLE 1-1 THERMAL NEUTRON CAPTURE CROSS SECTIONS	8
TABLE 2-1 MAXIMUM DIFFERENTIAL IRRADIATION OF PRE-TERRESTRIAL AND PRE- METEORITIC MATERIAL	28
TABLE 4-1 DESCRIPTION OF SAMPLES STUDIED	48
TABLE 4-2 INTERFERING IONS NEAR GD, EU AND SM SPECTRA	50
TABLE 4-3 BEAM INTENSITIES FOR SAMPLES CONTAINING ALL RARE EARTHS	51
TABLE 4-4 EXTRACTION OF GD, EU AND SM FROM ABEE	53
TABLE 5-1 FRACTIONATION CORRECTED PARAMETERS	75
TABLE 6-1 ISOTOPIC RATIOS OF GD IN TERRESTRIAL SAMPLES	79
TABLE 6-2 ADDITIONAL RESULTS FOR TERRESTRIAL GADOLINIUM	83
TABLE 6-3 ISOTOPIC COMPOSITION OF GD IN THE ABEE METEORITE	87
TABLE 6-4 ISOTOPIC COMPOSITION OF TERRESTRIAL AND ABEE EU	94
TABLE 6-5 ISOTOPIC COMPOSITION OF SM IN TERRESTRIAL SAMPLES	96
TABLE 6-6 ISOTOPIC COMPOSITION OF SAMARIUM IN THE ABEE METEORITE	97
TABLES III-1 to III-8 GD ISOTOPIC RATIOS FOR ALL TERRESTRIAL AND ABEE ANALYSES	121

ACKNOWLEDGEMENTS

The work reported in this thesis received considerable support from several persons in two different institutions.

The study of the Abee enstatite chondrite was first proposed by Dr. H. Mabuchi of the Department of Chemistry, University of Tokyo. He and Mr. S. Yanagita assumed responsibility for separating gadolinium, europium and samarium from a sample of the Abee meteorite. Their major contribution to this study is gratefully acknowledged.

The writer is indebted to Dr. M. Ozima of the Geophysical Institute, University of Tokyo, for his assistance with the mass spectrometry during the initial phase of this research. Dr. Ozima also coordinated the work of the two laboratories and was a visiting professor at U. B. C. from May to October, 1969. During this period the writer benefited from many profitable discussions with him.

Dr. Russell shared much of his experience in mass spectrometry with the writer and provided able supervision throughout this research. The writer is particularly grateful for Dr. Russell's assistance in solving many of the problems related to mass spectrometer instrumentation and data processing.

Without the generous cooperation of other graduate

students and faculty members this work would not have been possible. In particular, the close cooperation of John Ozard, John Blenkinsop and Lily Lee was a real asset.

The excellent services of the Computing Center at U. B. C. deserve a special word of thanks. Their facilities were used extensively and were always reliable.

Financial support came primarily from the National Research Council of Canada in the form of faculty grants and a studentship to the writer.

A 40 gram sample of the Abee meteorite was provided by the Geological Survey of Canada.

CHAPTER 1

INTRODUCTION

1.1 Chondrites - Remnants of Primitive Planetary Material

The study of meteorites has led to a vast amount of experimental data without much unanimity of interpretation. Yet, in many respects, the meteorites contain the best record available to us for events which occurred during the history of the solar system.

Meteorites consist primarily of silicate, metallic and sulphide phases; the three phases often occur together, in undifferentiated form. There are three main classes of meteorites which are based on the proportions of the silicate and metallic phases: stones, irons and stony-irons. The stones are further subdivided into chondrites (meteorites containing round silicate grains called chondrules in a matrix of silicates and metals) and achondrites (meteorites lacking chondrules). The achondrites resemble terrestrial igneous rocks, while the irons are thought to be similar to the material of the earth's core. It is widely believed that the achondrites and irons are broken fragments of one (or more than one) parent body having a diameter in excess of 10 km. Since the extent of differentiation into metallic and silicate fractions has not been firmly established, the stony-irons may represent either material from the vicinity of a

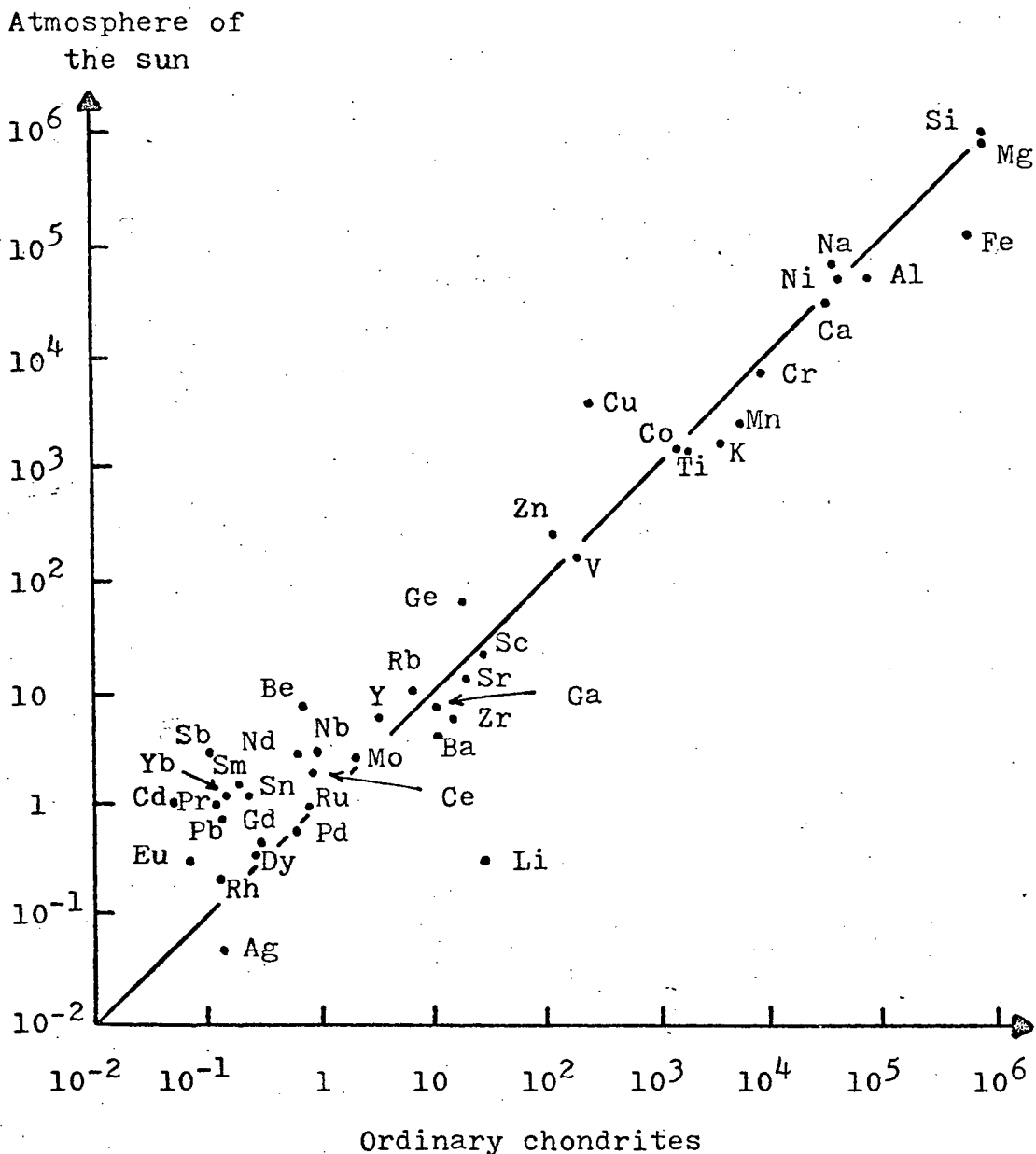
core-mantle boundary or fragments derived from the contact surfaces between metallic inclusions of meteoritic size and a stony matrix.

The remaining class of meteorites, the chondrites, comprises 85% of all meteorites, based on the number of recovered meteorites which were observed to fall. Detailed studies of their mineralogy and chemistry have led most researchers to believe that the chondrites represent the most primitive major class of meteorites (Anders, 1964; Wood, 1968). It is therefore this class which provides the crucial test of any theories for the origin of meteorites. The bulk chemical composition of the chondrites closely resembles the solar chemical composition, neglecting volatile elements. (Figure 1-1). This fact, in addition to the unique chondritic texture, strongly supports the belief that these are very primitive objects.

1.2 Quantization of the Oxidation State of Chondrites

Although the bulk chemical composition of chondrites is surprisingly uniform, there exist marked differences in their oxidation states. In fact, the oxidation states based on elemental and oxidized iron abundances appear to be quantized. Mason (1962) has plotted weight per cent iron (as metal or as FeS) against weight per cent oxidized iron (as silicates) for several precise analyses of chondrites (Figure 1-2). Six distinct groups are

FIGURE 1-1. ABUNDANCES OF THE METALLIC ELEMENTS



Elemental abundances in the atmosphere of the sun (relative to 10^6 Si atoms) are compared with those in ordinary (hypersthene and bronzite) chondrites. Elements with low boiling points have been excluded. Note the high abundance of Li in chondrites when compared with the sun. The diagram was reproduced from Meteorites and the Origin of Planets by John A. Wood, 1968.

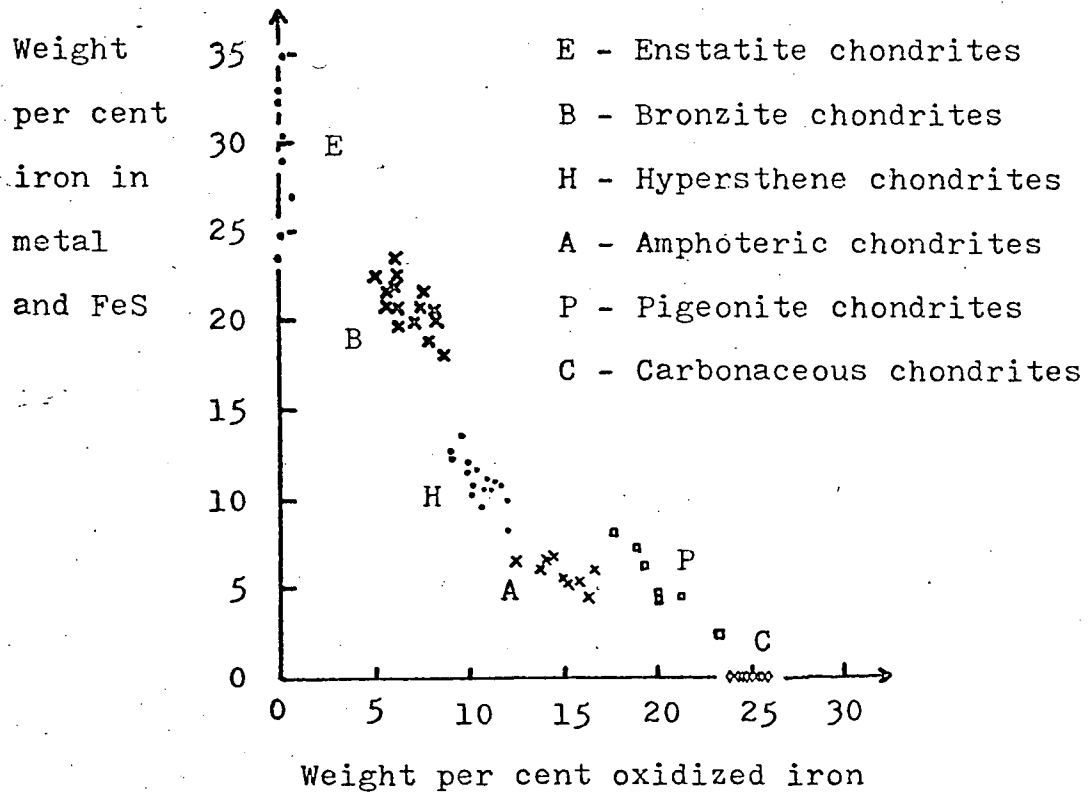
evident, ranging from fully reduced enstatite chondrites to fully oxidized carbonaceous chondrites.

Mason (1963) proposed that differences in oxidation state arose in the planetary nebula. The enstatite chondrites represent highly reduced material from the hot inner regions, while the carbonaceous chondrites represent more primitive, highly oxidized material which accreted in the cold outer regions of the nebula.

The quantization of the oxidation states may result from the accretion of material in the nebula to form planetary bodies, each of which possessed physical and chemical properties which were representative of the region from which it was derived. The chondritic meteorites may then represent a biased sample of collision fragments from only four or five planetary bodies.

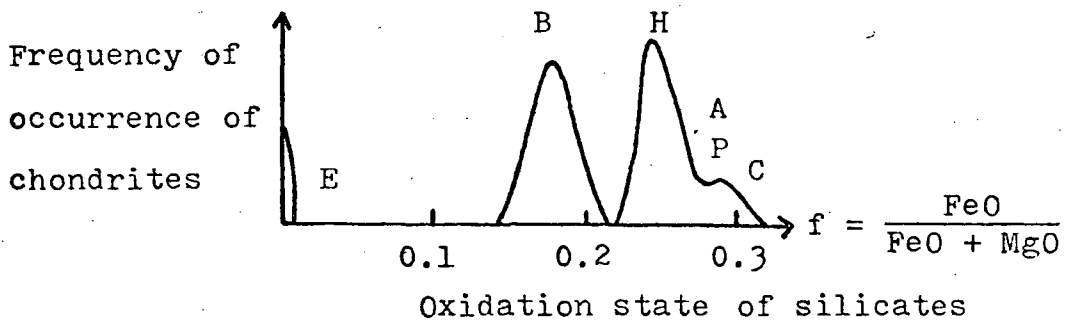
The reduction of iron-magnesium silicates proceeds by a decrease in the FeO content of the silicates and a corresponding increase in the amount of Fe in the metallic phase (Anders, 1964; Ringwood, 1966; Miyashiro, 1968). The MgO in the silicates remains essentially unaltered until extreme reduction has occurred. Therefore, the mole fraction $f = \text{FeO}/(\text{MgO} + \text{FeO})$ in silicates is a useful index of the degree of oxidation. By plotting frequency of occurrence against f for chondrites, Miyashiro (1968) drew attention to the large hiatus between enstatite chondrites and the other groups (Figure 1-3). He offered two possible

FIGURE 1-2. OXIDIZED AND REDUCED IRON IN CHONDRITES



Relationship between reduced iron (metal + FeS) and oxidized iron (FeO) in chondrites. The diagram was adapted from Mason (1962) and Anders (1964).

FIGURE 1-3. FREQUENCY OF OCCURRENCE VS OXIDATION STATE



The frequency of occurrence is plotted as a function of the f-value (oxidation state) for chondrites (after Miyashiro, 1967). See Figure 1-2 for identification of the chondrite classes.

explanations for this gap:

(a) Since carbon and hydrogen are the principle reducing agents, the large gap between the enstatite chondrites and the ordinary chondrites represents a marked difference in the reducing power of these two elements. Carbon was the principle reducing agent at higher temperatures close to the protosun while hydrogen reduction dominated in the cooler, outer regions.

(b) An alternative explanation is that the gap in the region $f = 0.01-0.14$ corresponds to the oxidation state of the primitive material from which the earth accreted. Birch (1964) reported an FeO content for the mantle of 10 ± 2 weight per cent. This implies that the amounts of oxidized and reduced iron for the earth as a whole (assuming the core contains 90% metallic iron) are approximately 4% and 23% respectively. On this basis, the oxidation state of the earth is intermediate between groups E and B in Figure 1-2. The f -value of the earth is less certain because of the unknown MgO content of the mantle.

If either of Miyashiro's explanations is valid, then variations in the oxidation state of chondrites result from differences in the amount of solar irradiation incident on the primitive material from which they were formed. It is generally accepted that the contracting protosun passed through a phase when its luminosity was

several hundred times its present-day value (Hayashi, 1966; Hoyle et al, 1968). The temperature distribution in the solar nebula has not been established, however.

On the basis of Miyashiro's hypothesis, one would expect the enstatite chondrites to show other evidence of their close proximity to the sun in their early history. Such evidence may be revealed through a comparison of the irradiation histories of meteoritic and terrestrial material. The earth provides a convenient standard of reference against which the orbital positions of other planetary bodies might be compared.

Several theories for the formation of the solar system postulate the existence of a period of high energy (~ 500 MeV) particle irradiation, of solar origin, during the collapse of the protosun and the transfer of angular momentum to the surrounding nebula via a magnetic coupling. The high energy particle flux would resemble the present-day primary cosmic ray flux, although its intensity was probably several orders of magnitude greater. When these particles (mainly protons and other light nuclei stripped of their electrons) bombard other nuclei they chip, or spall, nucleons from them, generating a large number of secondary particles. In particular, the number of neutrons produced by these spallation reactions would be comparable to the number of incident primary particles (Fowler et al, 1962). Both the primary

spallation reactions and secondary neutron capture processes are capable of altering the isotopic composition of the elements in the irradiated material.

1.3 High Energy Particle Irradiation and its Consequences

Gadolinium, samarium and europium are known to have enormously high thermal neutron capture cross sections which may be attributed to a few specific isotopes (Table 1-1). Hence

<u>Isotope</u>	<u>Cross Section</u>
Gd ¹⁵⁷	242,000 ± 4000 barns
Gd ¹⁵⁵	58,000 ± 3000
Sm ¹⁴⁹	40,800 ± 900
Eu ¹⁵¹	7,800 ± 200
Eu ¹⁵³	450 ± 20

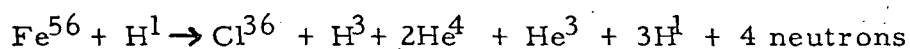
TABLE 1-1 Thermal (20° C) neutron capture cross sections for (n,γ) reactions (reported in Cook et al, 1968).

these may serve as highly sensitive neutron flux indicators. An examination of the isotopic compositions of Gd, Sm and Eu in meteorites and in terrestrial samples would reveal any significant differences in their irradiation histories. In particular, a study

of these elements in enstatite chondrites might provide a critical test of the hypothesis of Miyashiro.

Prior to 1969, no naturally-occurring isotopic anomalies had been detected for these elements, either in terrestrial or in meteoritic samples. No enstatite chondrites had been investigated, however. Recent advances in instrumentation have made it possible to measure isotopic ratios for microgram samples of Gd, Sm and Eu within 0.1% standard deviation. Using very precise techniques Eugster et al (1970a, 1970b) were able to detect a deficiency of Gd¹⁵⁷ in lunar rock and soil samples¹, as well as in the Norton County achondrite. The deficiency of Gd¹⁵⁷ relative to terrestrial Gd¹⁵⁷, and the corresponding enhancement in Gd¹⁵⁸ (Figure 1-4) may clearly be attributed to the Gd¹⁵⁷ (n, γ)Gd¹⁵⁸ reaction. The neutrons required for this process were produced by spallation reactions occurring in the surface layers of the moon and the parent meteorite fragment, due to bombardment by cosmic rays.

Cosmic rays in the 500 MeV range are capable of penetrating approximately 100g/cm² of matter. This is the mean free path for the primary particles which induce such spallation reactions as



¹ Both Eugster et al (1970b) and Lugmair (1970) reported errors of 0.01% (two standard deviations of the mean) for lunar Gd analyses.

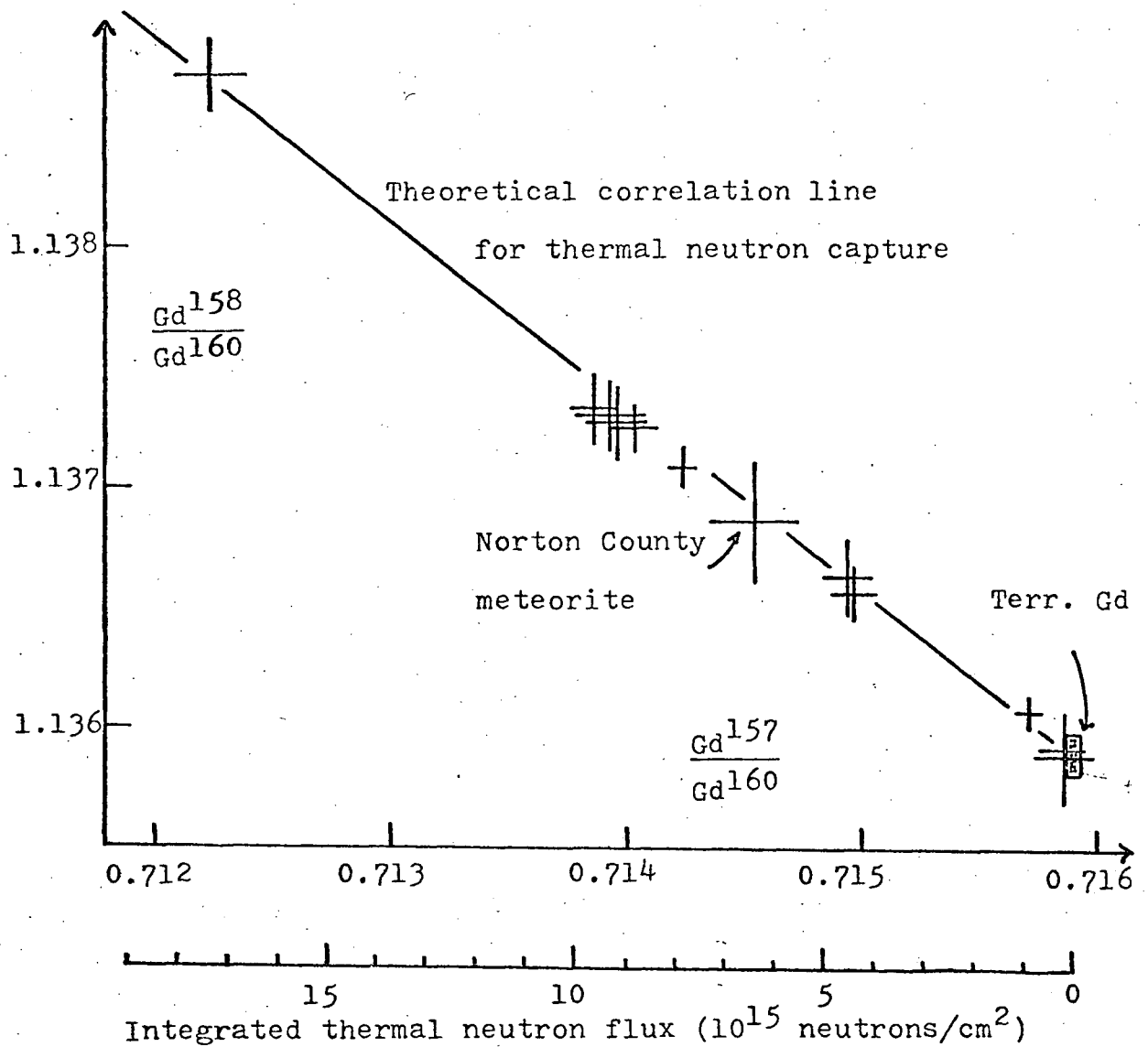


FIGURE 1-4. THERMAL NEUTRON CAPTURE IN LUNAR GADOLINIUM

$\text{Gd}^{158}/\text{Gd}^{160}$ vs $\text{Gd}^{157}/\text{Gd}^{160}$ (normalized to $\text{Gd}^{156}/\text{Gd}^{160} = .9361$) for several lunar samples from Apollo 11. Lunar samples include six rocks, one breccia, two core samples and soil. The Gd isotopic ratios are clearly shifted (relative to terrestrial Gd) due to neutron capture. Neutrons are continuously produced during bombardment of the lunar surface by cosmic rays. The correlation diagram and all data were published by Eugster et al (1970b).

High energy neutrons are a product of these reactions.

In the presence of light nuclei such as hydrogen, the neutrons are readily thermalized. The thermalization process involves slowing down high energy particles by multiple collisions with other nuclei, until energies in the thermal range ($\sim 20^\circ \text{C}$) have been reached.

Since reaction cross sections are much greater for slow neutrons, the majority of the neutrons will be captured only after reaching thermal velocities. In low density media, a significant fraction of the neutrons may undergo radioactive decay into protons and electrons, since the half-life of a neutron is only 11 minutes.

Neutron decay will be dominant only in dispersed media having mean densities $\lesssim 10^{-7} \text{ g/cm}^3$ (Fowler et al, 1962). The neutron thermalization and capture processes occur over a range of approximately 30 g/cm^2 . It is therefore evident that the secondary neutrons stray only a short distance from the primary cosmic ray path and are confined to the volume irradiated by the high energy particles. Although the penetration depth of cosmic rays varies with the energy of the primary particles and the composition of the irradiated material, a range of 1 to 4 meters is probable for $\sim 500 \text{ MeV}$ particles penetrating materials comparable to ordinary rock with a density of 2 to 4 g/cm^3 . The surface of the earth itself is largely shielded from cosmic rays by the 10^3 g/cm^2 of air in its atmosphere.

Outside the earth's atmosphere the present-day flux of primary cosmic rays having energies > 200 MeV is 1 to 10 particles/cm² sec. The bulk of this flux is of galactic origin and appears to have been of uniform intensity throughout the previous history of our solar system. Only a few per cent of the flux is derived from our sun. This fraction is of variable intensity, with maxima occurring during periods of intense solar flare activity.

Although the present-day high energy particle flux from the sun is small relative to the galactic flux, there is considerable evidence to suggest that this has not always been the case.

Several theories for the origin of the solar system propose the existence of an intense high energy particle flux during its early history (Burbidge et al, 1957; Fowler et al, 1962; Cameron, 1965; Hayashi, 1966). Although the irradiation times are short (10^4 to 10^7 years) the proposed values of the integrated high energy particle flux range from 10^{14} to 10^{22} protons/cm². This may be directly compared with the integrated cosmic ray flux of 10^{17} to 10^{18} protons/cm² since the formation of the earth and meteorite parent bodies approximately 4.5 billion years ago.

If an intense high energy proton flux was emitted from the protosun during the period prior to the formation of the major planetary bodies, then one would expect varying degrees of irradiation of the material of the nebula depending upon its distance from the protosun. The high energy particles would induce spallation

reactions in the material of the nebula which, in turn, would generate neutrons. Where local condensation of the material had occurred, a large fraction of the neutrons would be thermalized and captured; the remainder would decay.

The majority of the captured neutrons would react with H, O, Fe, Ni, S and Si nuclei which have high absolute abundances, although their cross sections are small (< 5 barns). These elements are not ideally suited for subsequent detection of the irradiation effects since the resulting changes in isotopic composition are small (except for H). The elements which show the largest memory effect after irradiation are those having isotopes with very high thermal neutron capture cross sections (e. g. Gd, Sm, Eu) or those having isotopes of low initial abundance (e. g. K, V). The isotopic abundances of several of the lighter elements (H, He, Li, B, C) are also very sensitive to particle irradiation, although the nuclear reactions in which they participate are much more difficult to resolve.

1.4 Delineation of the Present Study

The investigation of Gd, Sm and Eu in enstatite chondrites was first proposed to the writer by Dr. M. Ozima of the Geophysical Institute, University of Tokyo. Dr. Ozima was visiting professor in the Department of Geophysics at the University of British Columbia during the period May to October, 1969. He and Dr. Mabuchi

of the Department of Chemistry, University of Tokyo, initiated research into this problem. The present writer was invited to assume responsibility for the isotopic analyses of Gd, Sm and Eu because of his experience in mass spectrometry. The chemistry of the rare earth element separations was undertaken by Mr. Yanagita under the direction of Dr. Mabuchi. This research is therefore a joint project between the University of Tokyo and our own laboratory.

The previous research of the writer was in the field of ion optics at the University of Toronto. A computer program was written to calculate ion trajectories through two-dimensional electrostatic lenses. This method was sufficiently general to be applied to any realistic lens configuration encountered in mass spectrometer ion sources operating at low beam intensities. Ion beams were computed for three conventional ion sources which were shown to have low transmission efficiencies (Loveless, 1967). The first year of research at the University of British Columbia was devoted to the design of a more efficient ion source. This led to a clear definition of the fundamental limitation to the degree of focussing which may be achieved in an ion source. In particular, it was possible to estimate the maximum transmission efficiency of an ideal ion source in terms of basic parameters of the mass spectrometer and the ionization process (Loveless and Russell, 1969). This had not been reported before in the mass spectrometer literature.

A simple ion source having approximately one half the optimum transmission efficiency was then designed and built. This gave a factor of five increase in sensitivity (compared with the ion source previously in use) when tested on the available mass spectrometer (with a 12 in radius 90 deg sector, single stage mass analyzer). A further factor of two gain in sensitivity was achieved by attaching second order focussing shims to the analyzer magnet, so that a beam of higher angular divergence could be transmitted through the analyzer without loss of resolution. These fundamental improvements in instrument sensitivity, combined with the implementation of digital recording of mass spectra, were significant contributions by the writer in the field of mass spectrometer instrumentation. These modifications substantially increased the precision of isotopic analyses on the rare earth elements.

A 40 gram sample of the Abee enstatite chondrite was obtained from Dr. Douglas of the Geological Survey of Canada. This sample was part of specimen 13b taken from an equatorial slice through the meteorite. It was located 9-10 cm from the nearest fusion crust surface. (The meteorite was observed to fall on June 9, 1952 and was found five days later in a wheat field, near Abee, just north of Edmonton, Alberta (Millman, 1953). It had a recovery mass of 107 kg and a specific gravity of 3.5. The major constituents of the meteorite are enstatite (MgSiO_3) -

48%, kamacite-taenite (nickel-iron alloys) - 22%, and troilite (FeS) - 13%. Dawson et al (1960) report further details of the mineralogy, chemistry and petrology of the Abee meteorite.)

It is evident that several factors combined favourably to make this research practical. Although our laboratory has had considerable experience in the isotopic analysis of elements in the higher mass range (Rb, Sr, Pb, U), the rare earth elements had never been investigated previously at this institution. This challenge, in addition to the significance of the astrophysical problem itself, provided the interest and motivation for the writer's contributions to this study.

The specific contributions of the writer to the combined research project are:

(a) Improvements in instrumentation. An order of magnitude increase in sensitivity was achieved on the available mass spectrometer through improvements to the ion optics. The instrument was also interfaced with a magnetic tape recorder for digital recording of mass spectra.

(b) The development of procedures for analyzing the isotopic composition of 1 microgram quantities of Gd, Sm and Eu within a standard deviation of 0.1% or less. This includes experimental and computational techniques for removing the effects of trace quantities of interfering spectra from neighbouring elements, due to incomplete chemical separation.

(c) The precise isotopic analysis of Gd, Sm and Eu in terrestrial ores derived from two different geographic locations (USA and Brazil) and in the Abee enstatite chondrite.

The analysis of the above samples would reveal any isotopic anomalies as small as 0.1 - 0.3% due to variations in previous exposure to thermal neutrons. The two terrestrial ores were studied to establish the consistency of the terrestrial ratios, and to provide a reliable standard against which the meteoritic ratios could be compared.

The primary objective of this research is to search for an irradiation anomaly in the Abee enstatite chondrite. There is evidence which suggests that the protosun was a strong emitter of high energy particles during the early history of the solar system, prior to the formation of the planets and parent meteorite bodies. The existence of an irradiation anomaly for Abee would give strong support to the hypotheses of Mason and Miyashiro: that variations in the oxidation state of chondritic meteorites result from distinct differences in the mean distance from the sun of the primitive material from which the chondrites were derived.

CHAPTER 2

A REVIEW OF THE EVIDENCE CONCERNING IRRADIATION ANOMALIES

2.1 Synthesis of the Elements and High Energy Particle Irradiation

Burbidge, Burbidge, Fowler and Hoyle (1957) successfully explained the synthesis of most elements on the basis of chains of thermal nuclear reactions occurring in stellar interiors. Their theory is based on the assumption that only hydrogen is primeval. Successive stages of hydrogen burning, helium burning, and more complex nuclear processes are capable of synthesizing most elements in the interior of stars. However, the high temperature and pressure which play the essential role in their theory would destroy deuterium (D), lithium (Li), beryllium (Be) and boron (B) rather than synthesizing them. Even at moderately low temperatures these elements would be rapidly converted to helium by proton bombardment.

In order to explain the existence of these elements in meteorites and the earth (note the Li abundance in Figure 1-1) Fowler, Greenstein and Hoyle (FGH, 1962) proposed that the material of the solar nebula was subjected to high energy particle irradiation from the protosun prior to the formation of large planetary bodies. The most important interactions would be those of high energy (~ 500 Mev) protons and alpha-particles, with abundant nuclei such as O^{16} , Mg^{24} , Si^{28} and Fe^{56} . The elements D, Li, Be and B would be products

of such spallation reactions. The isotopic composition of some of these elements should differ from the terrestrial values, however, if they were produced by spallation alone. In particular, the terrestrial values of Li^6/Li^7 and $\text{B}^{10}/\text{B}^{11}$ are 0.08 and 0.23 respectively, whereas the predicted spallation yields should give ratios close to unity.

Fowler et al (1962) drew attention to the large thermal neutron cross sections for the reactions $\text{Li}^6(n, \alpha)\text{T}^3$ and $\text{B}^{10}(n, \alpha)\text{Li}^7$. They showed quantitatively that an integrated thermal neutron flux of 4×10^{21} neutrons/cm² would be capable of producing the observed isotopic ratios for Li and B. The assumption that thermal neutrons existed is entirely logical, since neutrons are direct products of spallation reactions, and thermalization of neutrons will occur prior to capture as long as there is a moderate excess of hydrogen in the irradiated material. (Fowler et al (1962) suggested a composition for the irradiated material of H₂O and the oxides of Mg, Si and Fe in the ratio two to one by volume.)

The terrestrial D^2/H^1 ratio of 1.5×10^{-4} was also explained by the neutron capture process $\text{H}^1(n, \gamma)\text{D}^2$, by imposing the additional condition that only 10% of terrestrial matter was exposed to the irradiation. Burnett, Fowler and Hoyle (1965) later revised this estimate to 5%. The fraction of terrestrial material which was irradiated was not relevant to the discussion of Li and B, since these elements were

assumed to have negligible abundances prior to irradiation. Their production was attributed entirely to irradiation processes, whereas H^1 was very abundant before irradiation.

In order to shield most of the terrestrial matter from the irradiation, Fowler et al (1962) proposed that the material of the nebula had condensed into solid planetesimals of dimensions from 1 to 50 metres. The high-energy particles could then penetrate the near-surface material to a depth of about one metre. The temperature of the planetesimals was estimated to be in the range 130-200° K.

The FGH theory for the synthesis of D, Li, Be, and B is supported by the observed high Li abundance in young (T Tauri) stars.

On the other hand, and contrary to prediction, very few variations in isotopic composition have yet been observed, between meteorites and the earth, for those nuclides which have very high neutron capture cross sections, low abundance ratios, or high spallation yields. A review of the search for such anomalies will be given in Section 2.2. For the moment, however, we suggest that one of the following alternatives must be true:

(a) The FGH process was operative but there are no significant irradiation anomalies between terrestrial and meteoritic samples because of uniform irradiation and dilution (Burnett et al, 1965).

(b) The FGH process was not operative; D, Li, Be and

B were not formed primarily by high energy particle irradiation during the early history of the solar system.

or (c) The search for anomalies has not been sufficiently thorough.

An alternative to the FGH theory for the synthesis of D, Li, Be and B has been given by Cameron (1962, 1965). He suggests that these elements are products of galactic nucleosynthesis and were already present in the interstellar medium from which the solar system was formed. Although Cameron dismisses the possibility of intense irradiation of the protoplanetary material as required by the FGH theory, he does postulate the existence of a moderate flux for the production of enough radioactive Al^{26} to melt bodies of asteroidal size (Cameron, 1965). Evidence of 'fossil' Mg^{26} , from the .72 m. y. decay of Al^{26} , has recently been reported for several meteorites by Clarke et al (1970).

2.2 A Review of the Search for Irradiation Anomalies

The search for irradiation anomalies has been restricted to terrestrial and meteoritic samples, although lunar rocks have become available within the past year. The only well-established anomalies which have been attributed to spallation reactions during (or prior to) the formation of the solar system were observed in the noble gases xenon and krypton (e. g. Reynolds, 1963; Merihue, 1963). Although these anomalies are large in a relative sense (enrichments

of up to 600%), they are small in an absolute sense (10^{-6} to 10^{-2} ppb of the meteorite mass).

Murthy (1960, 1962) reported anomalous isotopic compositions for silver (2 to 4%) and molybdenum (up to 7%) in certain iron meteorites, and an enrichment ($< 2\%$) in the light isotopes of barium was reported by Umemoto (1962). These apparent anomalies are all large in an absolute sense (0.1 to 170 ppb) but small in a relative sense. Recent attempts to verify these anomalies have largely discredited the earlier observations on the basis of mass spectrometer fractionation (Eugster et al, 1969; Chakraborty et al, 1964). Anomalies among the lighter elements have also been reported (references are given by Anders, 1964). Their interpretation is ambiguous, however, because of their susceptibility to chemical fractionation, addition of material from the solar wind, or bulk transfer in volatile gases.

Among the non-volatile elements, the isotopic ratios Li^7/Li^6 , $\text{K}^{40}/\text{K}^{41}$, $\text{V}^{50}/\text{V}^{51}$, $\text{Gd}^{157}/\text{Gd}^{158}$, $\text{Gd}^{155}/\text{Gd}^{156}$, $\text{Sm}^{149}/\text{Sm}^{150}$ and $\text{Eu}^{151}/\text{Eu}^{153}$ are particularly sensitive to irradiation. The isotopes of Li, K and V are direct products of spallation reactions, although their abundances are significantly altered by thermal neutron capture as well. For the rare earth elements (Gd, Sm and Eu) the isotopic abundances are much more strongly influenced by thermal neutrons than by direct spallation. Since these elements are of primary

interest in the present research, the results of investigations on Li, K and V will be interpreted in terms of the thermal neutron flux, rather than the primary high energy particle flux. This interpretation is based on the assumption of approximately a one to one correspondence between the thermal neutron flux and the primary flux > 200 Mev (after Fowler et al, 1962).

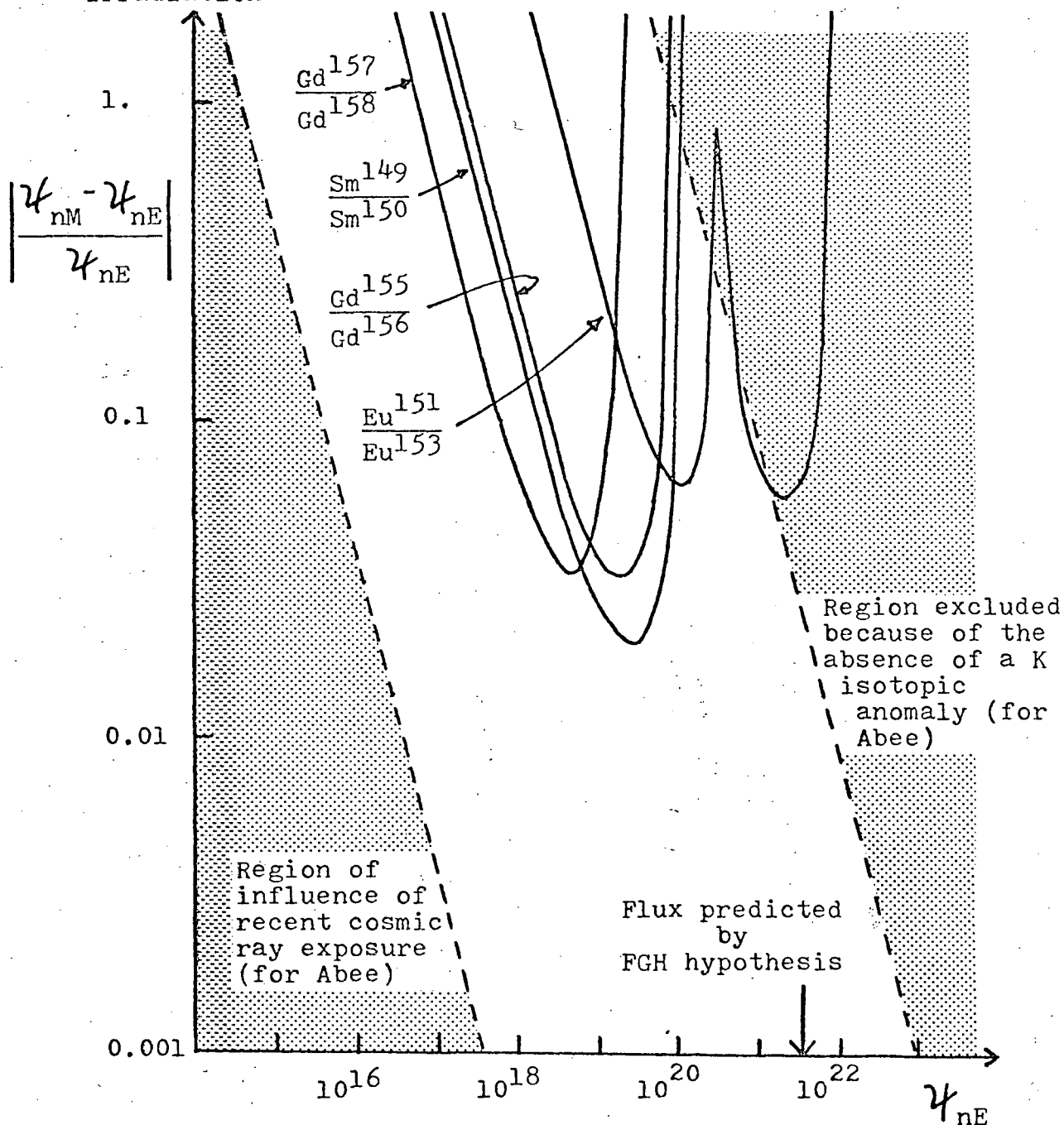
Figure 2-1 shows the relative sensitivity of the Gd, Sm and Eu isotopic ratios to differential irradiation of meteoritic and terrestrial material. In this diagram ψ_{nM} and ψ_{nE} represent the integrated thermal neutron flux irradiating meteoritic and terrestrial material respectively. The curves illustrate the range of values of $|\psi_{nM} - \psi_{nE}|/\psi_{nE}$ and ψ_{nE} for which a 0.1% anomaly would be observed in the relevant isotopic ratio. The area above each of these curves represents an anomaly $> 0.1\%$. (The procedure for computing the curves is outlined in Appendix I.) Figure 2-2 is a similar diagram except that only the most sensitive ratio, Gd^{157}/Gd^{158} , has been illustrated.

Figure 2-1 illustrates a model for which only 5% of the primitive material was irradiated, while the remainder was shielded in the interior of planetesimals several meters in radius. This model is consistent with the FGH hypothesis when $\psi_{nE} = 4 \times 10^{21}$ neutrons/cm². It does not assume that all planetesimals had the same dimensions, but rather that the distribution of planetesimal

FIGURE 2-1. MODEL FOR WHICH 5% OF PRIMITIVE MATERIAL

Differential
irradiation

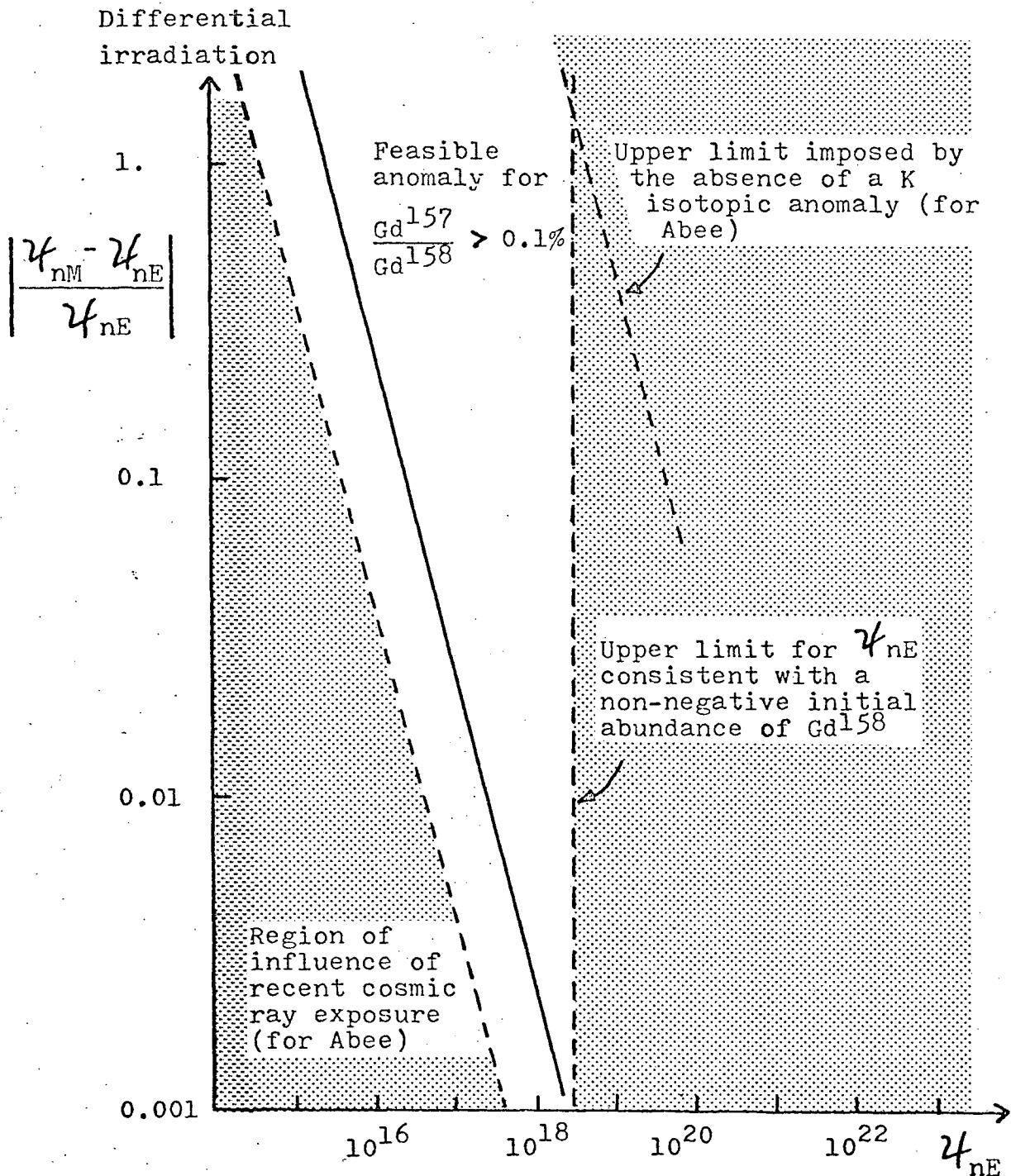
WAS IRRADIATED



Time-integrated neutron flux which irradiated primordial material from which the earth was formed (n/cm^2).

Curves show the sensitivities of the Gd, Eu and Sm isotopic ratios to a difference in the thermal neutron fluxes which irradiated primitive meteoritic (M) and terrestrial (E) matter prior to the formation of large planetary bodies. The area above each curve represents $>0.1\%$ isotopic anomaly.

FIGURE 2-2. UNIFORM IRRADIATION MODEL



Time-integrated neutron flux which irradiated primordial material from which the earth was formed (n/cm^2)

The region above the solid line represents a $\text{Gd}^{157}/\text{Gd}^{158}$ anomaly $> 0.1\%$ due to differential irradiation of primitive meteoritic (M) and terrestrial (E) matter. The other ratios are less sensitive to neutron capture (see Figure 2-1).

sizes and shapes was the same for both the pre-meteoritic and pre-terrestrial material. Presumably, the planetesimals later accreted to form larger planetary bodies in which mixing of the irradiated and non-irradiated fractions could occur.

The second model (Figure 2-2) assumes uniform irradiation of primitive material. This corresponds to planetesimals having a maximum radius of approximately one metre. For this model an upper limit for ψ_{nE} of 2×10^{18} neutrons/cm² can be set on the basis of the present-day Gd¹⁵⁷/Gd¹⁵⁸ ratio. A higher flux would imply a negative Gd¹⁵⁸ abundance initially.

Figures 2-1 and 2-2 are representative of several possible models; another important possibility is that the fraction irradiated was different for primordial meteoritic and terrestrial material.

On the basis of the FGH hypothesis, Burnett et al (1965) estimated that a given percentage variation in the integrated neutron flux would produce approximately the same percentage variation in Li⁷/Li⁶. The fact that Krankowsky et al (1964, 1967) observed no variations in this ratio in several meteorites (including the Abee enstatite chondrite) within an experimental uncertainty of 2% was therefore interpreted as placing an upper limit of 2% on the value of $|(\psi_{nM} - \psi_{nE})/\psi_{nE}|$. This is only true, however, if most of the terrestrial Li was produced by spallation within the solar system, and $\psi_{nE} = 4 \times 10^{21}$ neutrons/cm².

The limits on the differential irradiation history based on a 5% irradiation model (Figure 2-1) and a uniform irradiation model (Figure 2-2) are given in Table 2-1.

An investigation of the V^{50}/V^{51} ratio in several meteorites, including the Abee enstatite chondrite, revealed no anomalies within an experimental uncertainty of 2% (Balsiger et al, 1969).

Burnett et al (1966) searched for an anomaly in the K^{40}/K^{41} ratio in many classes of meteorites, again including Abee. They observed no anomalies, within an experimental uncertainty of 0.5%, which could be attributed to anomalous irradiation during the early history of the solar system. Small anomalies in the Norton County meteorite (a highly reduced achondrite), an iron meteorite, and a stony-iron, were attributed to recent cosmic ray exposure prior to capture by the earth. Estimates of the upper limit to the differential particle flux associated with a 0.5% anomaly for K^{40}/K^{41} are given in Table 2-1 (after Burnett et al, 1969).

The absence of an irradiation anomaly for K in the Abee enstatite chondrite places an upper limit on the differential irradiation $|\psi_{nM} - \psi_{nE}|$ of $\sim 1 \times 10^{20}$ neutrons/cm² for the 5% irradiation model and $\sim 5 \times 10^{18}$ neutrons/cm² for the uniform irradiation model. These are order of magnitude estimates only. The shaded regions on the right side of Figures 2-1 and 2-2 indicate unreasonable values of ψ_{nM} and ψ_{nE} based on the above limits for

TABLE 2-1. MAXIMUM DIFFERENTIAL IRRADIATION OF PRE-
TERRESTRIAL AND PRE-METEORITIC MATERIAL

Isotopic ratio	Uncertainty in published experimental abundance measurements	Energy range of particle flux	5% irrad. model (part/cm ²)	Uniform irrad. model (part/cm ²)
Li ⁷ /Li ⁶ *a	2%	≥ 75 Mev	2 x 10 ¹⁹	1 x 10 ¹⁸
K ⁴⁰ /K ⁴¹ *b	0.5-1%	≥ 500 Mev	6 x 10 ¹⁹	3 x 10 ¹⁸
		Thermal neut.	1 x 10 ²⁰	5 x 10 ¹⁸
		2-20 Mev neut.	6 x 10 ¹⁹	3 x 10 ¹⁸
V ⁵⁰ /V ⁵¹ *cd	2%	≥ 50 Mev	8 x 10 ¹⁸	4 x 10 ¹⁷
Gd ¹⁵⁷ /Gd ¹⁵⁸ #e	1%	Thermal neut.	-----	4 x 10 ¹⁶
Gd ¹⁵⁷ /Gd ¹⁵⁸ #f	0.1%	Thermal neut.	-----	3 x 10 ¹⁵

* Including Abee enstatite chondrite.

Excluding all enstatite chondrites.

a Krankowsky et al (1964).

b Burnett et al (1966).

c Balsiger et al (1969).

d Albee et al (1970).

e Murthy et al (1963).

f Eugster et al (1970a).

$|\chi_{nM} - \chi_{nE}|$ and, in the case of the uniform irradiation model, on the maximum value of χ_{nE} consistent with the present-day Gd^{157}/Gd^{158} ratio.

Murthy and Schmitt (1963) investigated Gd, Sm and Eu isotopic ratios for a recent Hawaiian basalt, three ordinary chondrites (i. e. hypersthene and bronzite chondrites), and one carbonaceous chondrite. They found no significant variation in the isotopic ratios within an experimental uncertainty of 1%. Although their observations suggest the absence of any large anomalies among the chondrites, they do not rule out the possibility of finding a significant anomaly for the Abee enstatite chondrite, since this class of chondrites was not investigated.

More recently, Eugster et al (1970) have measured the isotopic composition of Gd in several meteorites with a precision of 0.1%. Their results show agreement with terrestrial Gd within the experimental uncertainty, except for the Norton County achondrite which showed a decrease in the Gd^{157}/Gd^{158} ratio of $(0.27 \pm .04)\%$. They attributed this anomaly to the very large (230 m. y.) cosmic ray exposure age (Begemann et al, 1957) of the Norton County meteorite. Again, it is of significance to the present study that no enstatite chondrites were included in their investigations.

2.3 The Effect of Recent Cosmic Irradiation

Any interpretation of irradiation anomalies in meteorites

requires a knowledge of the extent of recent exposure to cosmic rays, prior to capture by the earth. Several methods have been developed for determining the cosmic ray exposure age of meteorites. Most methods employ two cosmogenic nuclides, one radioactive and one stable (e.g. $A^{39}-A^{38}$, $Cl^{36}-Ne^{21}$, $Al^{26}-Ne^{21}$ and $K^{40}-K^{41}$). Spallation reactions generate the nuclides at relative rates which can be estimated from controlled experiments with cyclotron beams. Assuming a constant cosmic ray flux, the rate of production of the radioactive nuclide will approach its decay rate after a few half-lives of exposure. If this steady state had been reached prior to capture by the earth, then the present-day abundances of the nuclides provide an estimate of the total exposure age. A comparison of the apparent exposure ages using different nuclide pairs provides a check on the accuracy of the method and the long term uniformity of the cosmic ray flux.

The cosmic ray exposure ages of meteorites are short ($< 10^9$ years) compared to the solidification and gas retention ages of the meteorite parent bodies. Most stone meteorites have cosmic ray exposure ages less than 60 m. y. (Anders, 1964). Evidently, the meteorites have spent most of their existence (after cooling, but before exposure to cosmic radiation) inside cold, inert bodies, or sizeable collision fragments of these bodies.

The Abee enstatite chondrite has a cosmic ray exposure

age of 13 m. y. (Begemann et al, 1959). If we assume a mean thermal neutron production rate of one neutron/cm²sec (after Eugster et al, 1970a, 1970b) then the integrated thermal neutron flux generated in Abee during recent exposure to cosmic radiation is $\sim 4 \times 10^{14}$ neutrons/cm². This flux would induce (n, γ) reactions in meteoritic material which would be indistinguishable from irradiation effects during the early history of the solar system. Since the earth itself is shielded from such processes, we may conclude that a differential irradiation $|\psi_{nM} - \psi_{nE}|$ less than 4×10^{14} neutrons/cm², between the Abee meteorite and the earth could not be interpreted in terms of the hypotheses of Mason and Miyashiro. This limitation is illustrated in Figures 2-1 and 2-2.

CHAPTER 3

INSTRUMENTATION

The aim of the present research is to precisely determine the isotopic composition of Gd, Sm, and Eu in a few selected samples. Particular attention will be focussed on those isotopes whose abundances would be changed by neutron irradiation: Gd^{155} , Gd^{156} , Gd^{157} , Gd^{158} , Sm^{149} , Sm^{150} , Eu^{151} , Eu^{153} .

3.1 Operational Principles of a Mass Spectrometer

The most common method of determining the isotopic composition of the metallic elements in general employs a solid-source mass spectrometer. The basic operational principles of this instrument are:

(a) The element to be studied is concentrated into a few drops of solution and deposited on one or two ribbon filaments, depending upon whether a single or triple filament configuration is to be used. The filaments are typically made of high work-function metals such as tungsten, rhenium, tantalum or platinum. The drops are evaporated to dryness by passing a current through each filament while exposed to the atmosphere. This leaves a salt, containing the element of interest, on the surface of the filament(s).

(b) The filament(s) are then positioned in a mass

spectrometer and the system is evacuated to a low pressure ($\leq 10^{-7}$ torr).

(c) The sample is slowly evaporated and partially ionized at high filament temperatures. If a single filament is used, both processes occur on the same surface. In the case of the triple filament configuration (after Inghram et al, 1953) the sample is evaporated from two side filaments and ionized mainly by a third (center) filament which is at a much higher temperature. The type of ions produced, and their relative abundances, will depend upon the composition of the salt, the filament temperatures (and work function); the ionization potentials of the components and the total geometry.

(d) An electrostatic lens is used to accelerate the resulting positive ions through a potential difference, which is typically a few kilovolts. The lens also focusses and collimates the beam into a ribbon-shaped stream of monoenergetic ions. The combined filament assembly and electrostatic lens is commonly referred to as an ion source.

(e) The monoenergetic ion beam is transmitted through a magnetic field which separates the beam into several components with different charge-to-mass ratios. For a suitable value of the magnetic field each component beam can be focussed independently onto a current sensing device (e.g. a Faraday cup or electron multiplier).

(f) By slowly varying the accelerating voltage or the magnetic field intensity, the relative intensities of the component ion beams can be monitored. Figure 3-1 shows a sample spectrum for Gd^{+} ions (omitting the mass 152 peak). In the absence of mass discrimination effects, or interference by other spectra, the relative peak heights are directly related to the relative isotopic abundance values in the original sample. It is often necessary to apply a correction for the growth (or decay) of the ion beam intensity as a function of time. This is sometimes accomplished by using a polynomial representation of the total beam intensity and transforming all measured peak heights to their effective values at a common point in time.

The above discussion outlines the basic operational principles of a single-stage mass spectrometer. As with any experimental technique there are many practical difficulties associated with each new application. There are also fundamental limitations of the instrument itself regardless of the problem under investigation. Some of the problems which received particular attention during the present research will now be reviewed.

3.2 Ion Optics

"The ion source is clearly the 'heart' of the (mass) spectrometer and is, as might be expected, the part exhibiting the greatest complexity of action." (Barnard, 1953, p. 47)

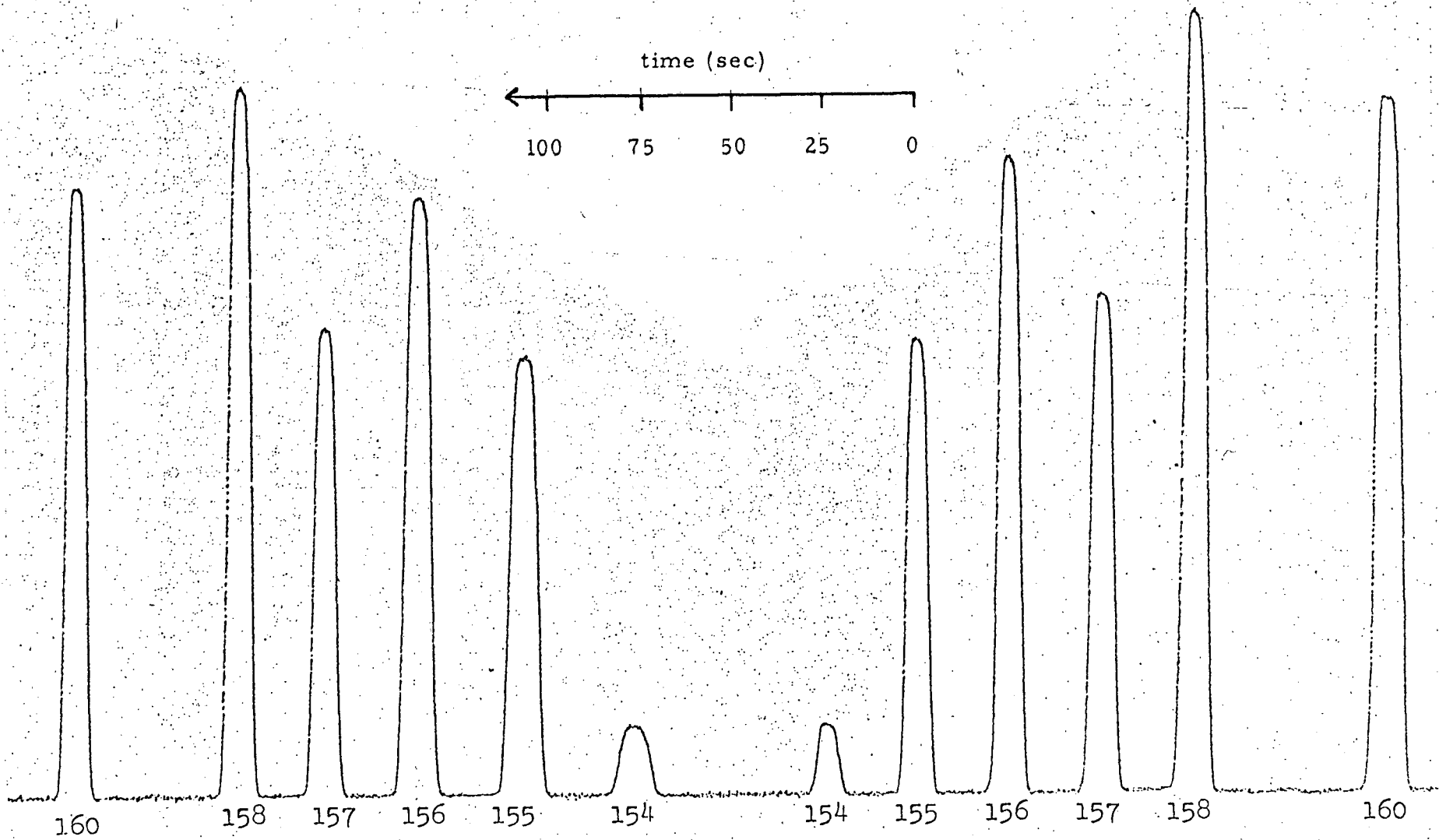


FIGURE 3-1. CONTINUOUS SCANNING OVER THE GADOLINIUM SPECTRUM

Prior to investigating the rare earth elements, the writer's interests were directed toward the ion optical properties of ion sources, i. e. their ability to focus and transmit ions. To study this problem, ion trajectories were calculated through several two-dimensional ion sources. Laplace's equation was solved by a finite-difference method and ion paths were computed by numerical integration of the trajectory equation (Loveless, 1967).

These investigations led to the design of the lens system shown in Figure 3-2. The trajectories illustrated were calculated assuming an initial ion energy $kT = .015$ eV (corresponding to $T = 1750^\circ$ K on the center ionizing filament - .001 x .030 inch ribbon) and angles of inclination to the lens axis from 0 to ± 75 deg. This lens was shown to be capable of transmitting 70% of the ions produced at the center filament (for the most critical focussing plane illustrated in Figure 3-2). Loveless and Russell (1969) compared the properties of this lens with those of an ideal lens, using the concepts of beam emittance and instrument acceptance which had not been applied before to mass spectrometer ion sources. Through the use of these concepts it was possible to clearly define the limitation to beam focussing and transmission efficiency in terms of basic instrument parameters. An understanding of this limitation will be of considerable value in the future design of mass spectrometers, and will avoid wasted effort in attempting to achieve what is theoretically impossible.

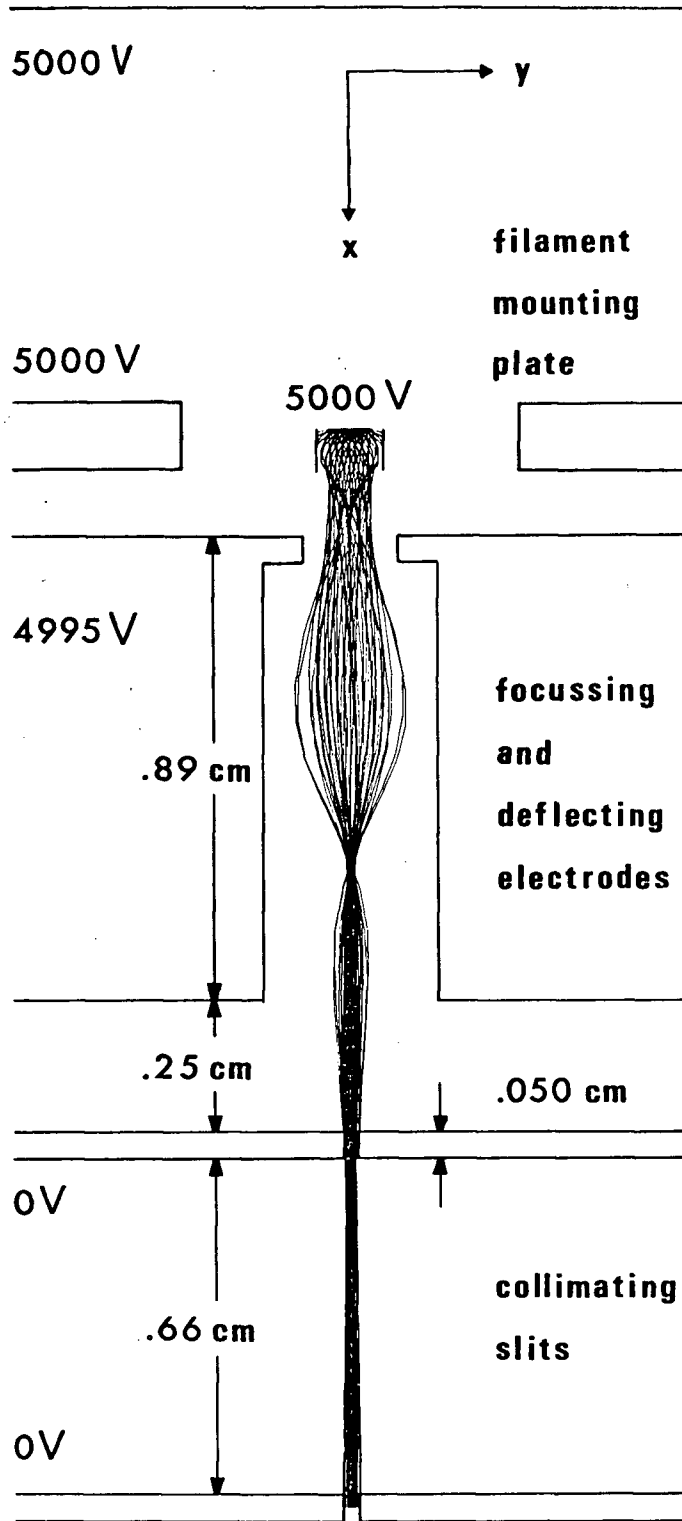


FIGURE 3-2. ION BEAM PRODUCED BY NEW ION SOURCE

The ion source in Figure 3-2 is a simple design, with strong focussing properties (because of the use of thick electrodes) which has proved its effectiveness in practice and has consistently provided satisfactory peak shape and resolution when the focussing electrodes are tuned to give maximum beam intensity. It replaces a complex stack of thin slits which were acting essentially as a collimating system, with minimal focussing capability. The new source gave a factor of five increase in sensitivity, with comparable resolution.

This achievement was coupled with a factor of two increase in sensitivity through the use of second order focussing shims which enabled a beam of higher angular divergence to be used. This method of achieving second order focussing is attractive because it uses only a single pair of shims on one side of the analyzer magnet, and requires no modification of the basic magnet. It is discussed in Appendix II.

The increased sensitivity resulting from fundamental improvements in the ion optics of the available mass spectrometer represents a significant contribution by the present writer. Although the analysis of the rare earth elements would still have been possible without these modifications, the precision of the results would have been somewhat poorer.

3.3 The Ionization Process

The most inefficient process occurring in the mass spectrometer was the conversion of neutral atoms into positively-charged ions which can be accelerated and injected into the analyzer magnet. With the triple (rhenium) filament arrangement, only about 15% of the evaporated atoms succeeded in hitting the hot ionizing filament. Of these, only 1% or less were emitted from the center filament as Gd^+ ions. The ionization efficiency was greater for Sm and Eu.

Three possible ways of improving the ionization efficiency will be briefly reviewed.

(a) The single filament technique has been shown, at least in certain configurations, to produce an ion beam which is an order of magnitude more intense than that produced by the triple filament method (Eugster et al, 1970a). Both Eugster et al (1970a, 1970b) and Lugmair (1970) have extensively used single, zone-refined (high purity) rhenium filaments for the isotopic analysis of Gd. Since their work has been published, the present writer has used the single filament method for several Gd analyses, including Abee.. Although comparable sensitivity was achieved for both the single and triple filament techniques, the former did not appear to be significantly better, even when zone-refined rhenium filaments were used. Since very few single filament analyses were performed, however,

this may reflect a lack of experience with this technique.

Alternatively, the poor triple filament sensitivity observed by Eugster et al (1970) may result from low transmission efficiency in their ion source when using this filament configuration.

One minor complication with the single filament technique is the fact that GdO^+ ions are much more abundant than Gd^+ ions. For this reason the GdO^+ spectrum was analyzed, and a correction was made for the isotopic composition of oxygen. This actually proved to be an advantage in the analysis of the Abee sample which produced interfering LaO^+ ions in the Gd^+ spectrum but no significant interference in the GdO^+ spectrum.

The magnitude of mass fractionation is generally greater for single filament analyses, making this method less precise for the determination of absolute isotopic abundances. (Mass fractionation, or discrimination, commonly occurs on hot filament surfaces due to preferential evaporation of the lighter isotopes of an element.)

(b) The use of a porous filament surface (e. g. Goris, 1962) or the retention of the sample in a silica gel (Cameron et al, 1969) are promising ways of increasing the yield of positive ions from a single filament. The writer has not

investigated these techniques because of the highly specialized filament treatment or sample preparation required.

(c) A third possible improvement involves the use of two partially-closed (canoe-shaped) sample filaments with slit openings aimed directly at the centre ionizing filament. This method should greatly increase the probability that an evaporated atom will strike the centre filament. Several attempts were made by the writer to use this technique, but no significant improvement was evident. Apparently, this method has promise but requires close control during each stage of preparation: making a V-shaped crease along the length of the filament, shaping and mounting it on posts, outgassing it without loss of ductility, depositing and evaporating the sample inside the 'canoe', closing the filament sides without loss of sample, and carefully alligning them with respect to the centre filament. It is believed that fractionation would not be enhanced by this technique.

Although the ionization process is recognized as being the least efficient process occurring in the instrument, the writer has not made significant progress on this problem. The triple filament technique was used for most analyses because an elemental Gd^+ ion beam of sufficient intensity could be produced by this method, and mass discrimination effects were expected to be less.

3.4 Digital Recording of Mass Spectra

No modifications were made to the existing collector system of the mass spectrometer. The electronic circuitry and the electrode configurations were designed by other workers in our laboratory (R. D. Russell, J. Blenkinsop, J. S. Stacey, and J. M. Ozard)

The entrance slit of the collector had a width of 0.020 inch. A standard Faraday cup and 10^{11} ohm resistor served as an ion detector. The voltage developed across the resistor was amplified by an adjustable gain (5 ranges), hybrid d. c. amplifier, and fed both to a chart recorder and to a digital voltmeter. The chart recorder provided a visual display of the beam intensity at the collector while the digital voltmeter was used primarily to output data in a digital (binary-coded decimal) format.

An interfacing device was designed and built by the writer to enable continuous recording of spectra on a seven track magnetic tape recorder. The data could then be processed by computer (see Section 3.5 and Chapter 5).

The output from the mass spectrometer measuring system was integrated over $\sim \frac{1}{7}$ second intervals by the digital voltmeter and transferred to magnetic tape at the rate of 7 data/sec. Each datum consisted of 6 characters: $3\frac{1}{4}$ binary-coded decimal digits from the digital voltmeter, 1 control character giving shunt information and scan direction (up, down or stationary), and an end-of-word character.

The Gd^+ spectrum of Figure 3-1 was taken by continuous magnetic scanning over the mass ranges 160-154 and 154-160 in succession. However, because of the steady decay of the Gd^+ beam as a function of time, this does not represent an efficient way of utilizing the available beam. Little time is spent measuring the peak intensities, while much time is lost between the peaks measuring baselines which are relatively stable.

More efficient use of the ion beam is illustrated in Figure 3-3. In this case the baselines are measured for computational purposes at positions $\frac{1}{2}$ mass above and $\frac{1}{2}$ mass below the highest and lowest masses respectively. This is done for both the down-mass and up-mass portions of the scan. Between peaks the magnet current is advanced manually. Slow continuous scanning may then be employed over the peaks only. This scanning technique, hereafter referred to as discontinuous slow scanning, was used for all analyses reported here.

Each scan comprises the following records:

- (a) Measurement of baselines on each shunt for a minimum of 5 seconds at a position $\sim \frac{1}{2}$ mass above the high-mass peak in the spectrum to be recorded. (Scan direction: stationary).
- (b) Discontinuous slow scan down the spectrum to a position $\sim \frac{1}{2}$ mass below the low-mass peak. (Scan direction: down).
- (c) Measurement of baselines on each shunt for a minimum

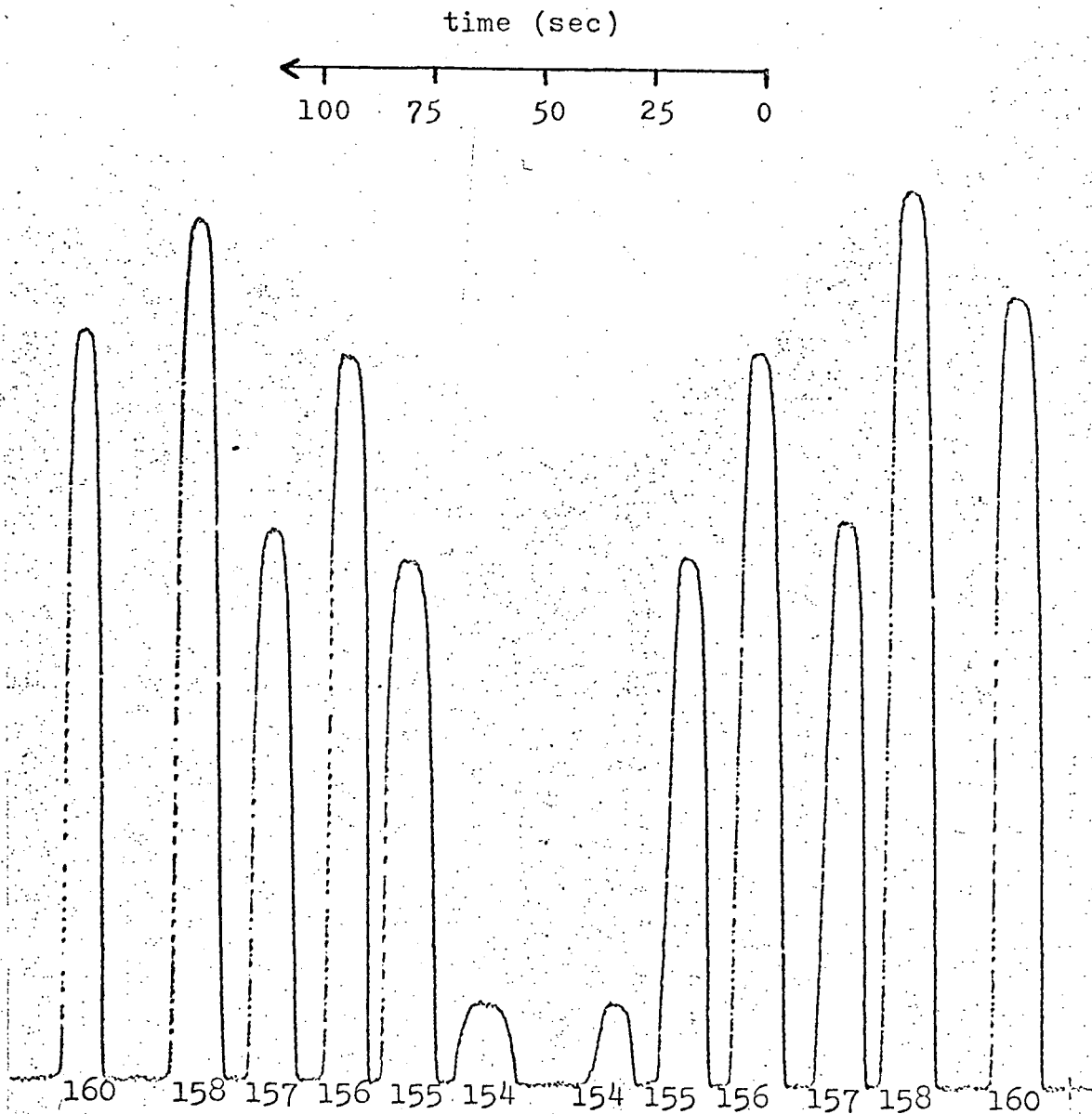


FIGURE 3-3. DISCONTINUOUS SCANNING OVER THE GADOLINIUM SPECTRUM

The diagram represents one scan of the Gd^+ spectrum. In this thesis a scan is defined as one down-mass sweep of the spectrum plus one up-mass sweep. Baselines are measured above the high-mass peak of the spectrum and below the low-mass peak.

of 5 seconds. (Scan direction: stationary).

(d) Discontinuous slow scan up the spectrum to a position $\sim \frac{1}{2}$ mass above the high-mass peak. (Scan direction: up).

(e) Same as (a).

During subsequent reduction of the data, baselines were recognized by the fact that the scan direction was stationary.

The effective peak intensity and the time of measurement could readily be deduced from the recorded data (see Chapter V).

3.5 Noise Rejection Using a Low-Pass Filter

It is evident from Figure 3-3 that high frequency noise is superimposed on the mass spectrum. Since we are interested in computing peak heights, rather than the area under each peak, it is particularly important to smooth out the effect of noise by using a suitable filter. The local maxima of the filtered spectrum will then be a truer representation of the signal intensity of the spectral peaks.

A low-pass filter was designed for this specific application by R. D. Russell and J. Blenkinsop. The frequency response function of the filter is illustrated in Figure 3-4. The data window has a width of 2.4 sec, which is consistent with the minimum width of peak-tops of 3 sec. The filtered data consists of $\frac{7}{6}$ data points/sec.

The filtering process was only the first stage in the reduction of the recorded data. All processing was performed on an IBM 360 computer through the facilities of the Computing Centre at U. B. C.

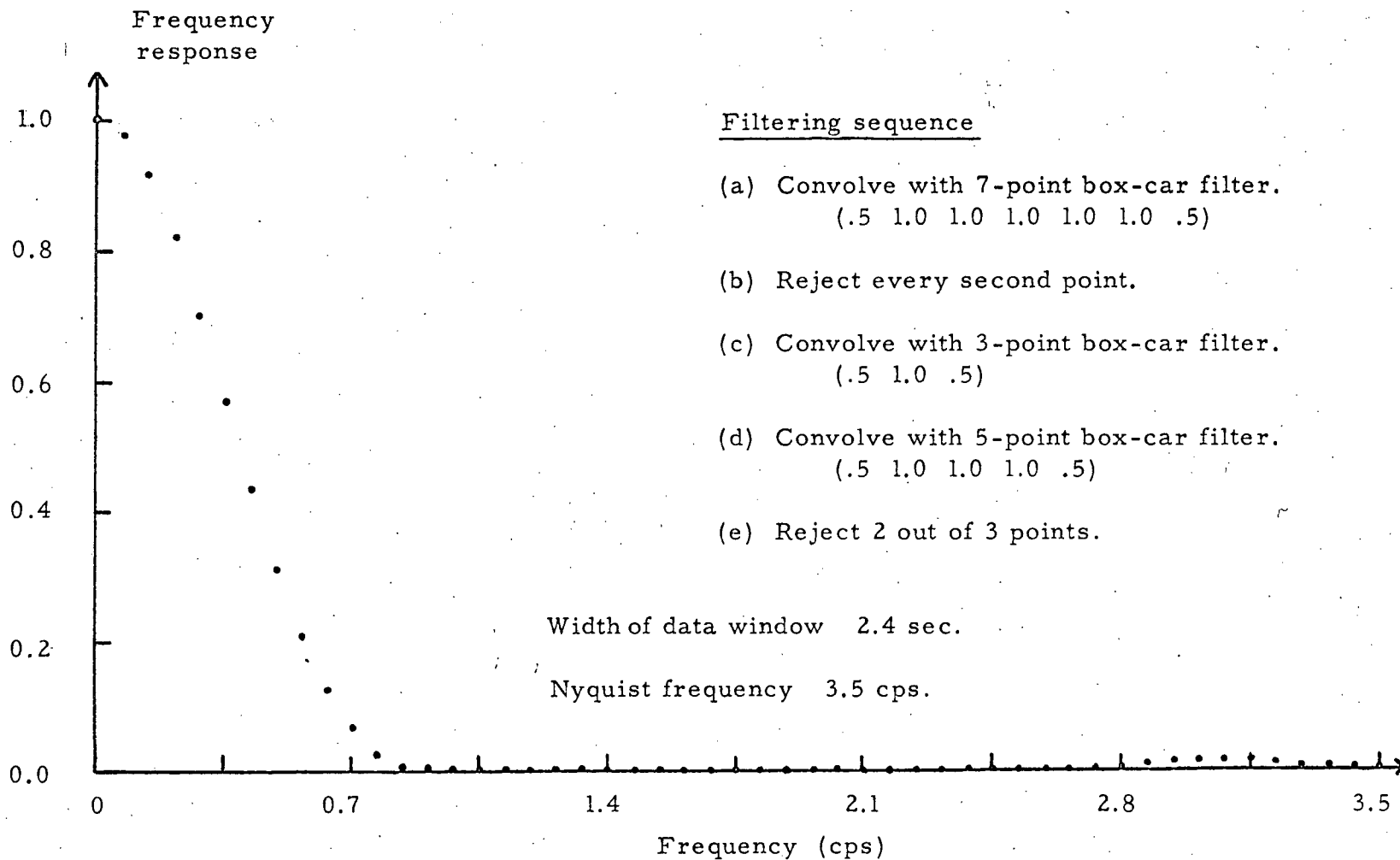


FIGURE 3-4. FREQUENCY RESPONSE OF DIGITAL FILTER

The filter was designed by R. D. Russell and J. B. Blenkinsop to reject high frequency noise from the recorded data.

CHAPTER 4

PREPARATION OF SAMPLES

Terrestrial ore samples were obtained in the form of reagent Gd_2O_3 , Sm_2O_3 , and Eu_2O_3 from Matheson Coleman and Bell, Cincinnati, Ohio, and the Shinetsu Kagaku Co., Tokyo, Japan. All reagents had a specified purity of 99.9%. A sample name was assigned to each of the reagents for convenience of reference (see Table 4-1).

A basalt sample from Kitamatsu-ura, Japan (JB1) was used to gain experience in the chemical separation and mass spectrometry of the rare earth elements. Although the experimental techniques were tested on this sample, no precise analyses were performed to determine its isotopic composition.

The concentration of the rare earths was an order of magnitude greater in the basalt than in the Abee meteorite. In order to consistently use microgram samples of Gd in all mass spectrometer analyses approximately 10 grams of the meteorite were processed for analysis, whereas only 1 gram samples of the basalt were used.

4.1 Separation of the Rare Earth Elements

The extraction of Gd, Sm and Eu from the basalt and meteorite samples was performed by S. Yanagida and Dr. H. Mabuchi

TABLE 4-1. DESCRIPTION OF SAMPLES STUDIED

<u>Sample</u>	<u>Specifications</u>	<u>Source</u>
Gd-US	$Gd_2O_3^a$	Matheson Coleman & Bell, U.S.A. - derived from Humphrey's Mine, Folkston, Georgia, U.S.A.
Eu-US	$Eu_2O_3^a$	
Sm-US	$Sm_2O_3^a$	
Gd-J	$Gd_2O_3^a$	Shinetsu Kagaku Co., Japan - derived from a mine near Rio de Janeiro, Brazil.
Eu-J	$Eu_2O_3^a$	
Sm-J	$Sm_2O_3^a$	
JBl	$\left\{ \begin{array}{l} 4^b \text{ ppm Gd} \\ 1^b \text{ ppm Eu} \\ 5^b \text{ ppm Sm} \end{array} \right\}$	Kitamatsu-ura, Japan
Abee	$\left\{ \begin{array}{l} 0.3^c \text{ ppm Gd} \\ 0.06^c \text{ ppm Eu} \\ 0.2^c \text{ ppm Sm} \end{array} \right\}$	Geological Survey of Canada - part of specimen 13b

a All terrestrial samples were in the form of reagents having a specified purity of 99.9%.

b Abundances correspond to terrestrial mean values for diabases.

c Based on analyses of the Abee meteorite by Shima and Honda (1967).

of the Department of Chemistry, University of Tokyo. The mass spectrometry was undertaken by the present writer in the Department of Geophysics, University of British Columbia.

The rare earth elements in the lanthanide series (La, Ce, Pr, Nd, Pm, Sm, Eu, Gd, Tb, Dy, Ho, Er, Tm, Yb, Lu) have similar chemical properties, making the separation of one element, from the remainder of the elements in the series, difficult. In order to assess whether separation of these elements was essential, the first analyses on Gd, Eu and Sm were performed on samples containing the complete lanthanide series of elements (samples JB1-1 and JB1-2). Although Gd, Sm and Eu ion beams were successfully produced in the mass spectrometer, the abundance of interfering ion spectra inhibited reliable interpretation of the isotopic composition of these elements. Tables 4-2 and 4-3 indicate some of the ions which were identified during the mass spectrometer analyses. Apart from the rare earth elements and their oxides, the most critical contaminant was barium which produced Ba^+ , BaF^+ and $BaCl^+$ ion beams. The abundance of these ions was attributed to the low ionization potential of barium and its compounds. Even small traces of barium were sufficient to generate intense ion beams.

Several modifications were made to the separation techniques until a three-stage ion exchange process was adopted. This technique

TABLE 4-2. INTERFERING IONS NEAR GD, EU AND SM SPECTRA

<u>Mass</u>	<u>Ions</u>
143	Nd(12.17)
144	Sm(3.09),Nd(23.85)
145	Nd(8.20)
146	Nd(17.22),BaO(.11)
147	Sm(14.97)
148	Sm(11.24),Nd(5.73),BaO(.10)
149	Sm(13.83),BaF(.11)
150	Sm(7.44),Nd(5.62),BaO(2.41)
151	Eu(47.82),BaO(6.58),BaF(.10)
152	Sm(26.72),Gd(.20),CeO(.19),BaO(7.84)
153	Eu(52.18),BaO(11.22),BaF(2.42)
154	Sm(22.71),Gd(2.15),LaO(.09),CeO(.25),BaO(71.55),BaF(6.59)
155	Gd(14.73),LaO(99.67),BaO(.05),BaF(7.85)
156	Gd(20.47),Dy(.05),CeO(88.27),LaO(.04),BaO(.15),BaF(11.23)
157	Gd(15.68),PrO(99.76),CeO(.03),LaO(.20),BaF(71.70)
158	Gd(24.87),Dy(.09),CeO(11.23),NdO(27.04),PrO(.04)
159	Tb(100.00),NdO(12.15),PrO(.20)
160	Gd(21.90),Dy(2.29),NdO(23.85),SmO(3.08),CeO(.02)
161	Dy(18.88),NdO(8.31)

Each type of ion is listed with its percentage abundance as given in the Handbook of Chemistry and Physics (1970). Barium abundances were taken from Eugster et al (1969). All oxygen isotopes were considered when calculating the abundances of the oxide ions. Some of the abundances may be in error by as much as 1-2%.

Sample & Filament Configuration	Fil. Current (amps)	Ba ⁺ 138	BaF ⁺ 157	LaO ⁺ 155	CeO ⁺ 156	Eu ⁺ 153	Sm ⁺ 152	Gd ⁺ 158	Other
JB1-1a tantalum closed canoe	2.1	4.0	.05	.2	.5	.04	.002	<.005	GdO ⁺ (174) = .07
	3.0					.05	.05		
JB1-1b tantalum flat	1.4	2.0	<.003	.02	.04				Nd ⁺ (144) = .01
	2.6	>10.	.1	.08	10.	.02	.02	<.003	
	2.8					.1	.08		
JB1-2a tantalum part. closed	1.3	.3				.001			Tb ⁺ (159) <.001
	2.6					.04	.01		
	3.0		.02	.2	.7	.06	.03	<.1	
JB1-2b rhenium flat	1.1	.2		.001	.008	.02			Cs ⁺ (133) = .05
	1.5	.2		<.0005	.01	.1	.1	<.0005	GdO ⁺ (174) = .01
	1.8	.2							Dy ⁺ (162) = .03
	1.9							<.003	GdO ⁺ (174) <.005
	2.2	>10.	>10.	1.	4.				

TABLE 4-3. Examples of beam intensities observed (using variations of the triple filament technique) when Gd, Eu and Sm were not separated from the other rare earth elements. Beam intensities are specified in units of 10^{-11} amps. Filament currents cannot be directly compared between analyses because of different configurations and sample histories. Blank entries in the table do not imply the absence of an ion beam.

attempted complete separation of Gd, Eu and Sm into three different fractions for independent analysis in the mass spectrometer. The analytical scheme is summarized in Table 4-4.

The 9.5 gram Abee sample was completely dissolved in HF and HClO_3 , evaporated to dryness, and redissolved in 0.5 N HCl. The solution was loaded onto a cation exchange column containing Diaion SK#1 resin. Most of the rare earths were separated from all major constituents by elution with 2 N HCl followed by 6 N HCl.

A second column was then used to separate Gd, Eu and Sm from the other rare earths using 0.5 M 2-methyl lactic acid. The rare earth elements were eluted in order of decreasing atomic number (or increasing ionic radius). Calibration of the exchange column was performed using a solution containing artificially-produced radioactive isotopes of the rare earth elements. The activity of the eluate was monitored to yield the elution curves in Figure 4-1.

After separation of Gd, Eu and Sm into three separate fractions, a third ion exchange process (similar to the first one) was used to further reduce the concentration of alkalis and alkaline earths in the individual fractions. The separated Gd, Eu and Sm fractions were then converted into perchlorate salts in preparation for loading in the mass spectrometer.

Although the separation technique succeeded, the elution

TABLE 4-4. EXTRACTION OF GD, EU AND SM FROM ABEE

1. Dissolve 9.5 gram Abee sample in 300 ml HF and 20 ml HClO₄ and evaporate to dryness.
2. Dissolve in 20 ml 6 N HCl and evaporate to dryness.
3. Dissolve in 400 ml 0.5 N HCl and store in polyethylene bottle.
4. Pack resin in 45 x 1.6 cm column and precondition with 1500 ml 6 N HCl and 1500 ml H₂O to a height of 43 cm.
5. Load 400 ml solution (containing sample) onto column.
6. Elute with 840 ml 2 N HCl to remove major constituents.
7. Elute with 150 ml 6 N HCl and collect eluate containing all rare earth elements.
8. Evaporate to dryness and dissolve in a few drops of HNO₃.
9. Repeat procedure 8.
10. Dissolve in 2.5 ml H₂O in preparation for loading on second ion exchange column.
11. Precondition resin to remove traces of rare earth elements and barium. Wash with approximately 1000 ml 6 N HCl and then remove acid with 3x distilled H₂O. Convert resin to NH₄⁺ form by adding 500 ml 7.5 N NH₄OH. Wash with H₂O. Preconditioning gives a resin height of 22 cm.
12. The sample solution (from 10 above) was loaded onto the second (25 x 0.4 cm) cation exchange column.
13. Elute with 0.5 M 2-methyl lactic acid (pH of 3.20).
14. Collect the Gd, Eu and Sm fractions from the eluate as specified in Figure 4-1.
15. Add 1 N HCl to each fraction to lower the pH to 2.5 ; then dilute (by a factor of two) by adding an equal volume of H₂O.
16. Load each fraction onto a third column to remove the 2-methyl lactate from the solutions. For each fraction in turn, precondition resin with 100 ml 6 N HCl and 50 ml H₂O to a resin height of 10 cm in a 15 x 0.4 cm cation exchange column. Load the fraction onto the column and wash with 5 ml 2 N HCl. Elute with 10 ml 6 N HCl to release the rare earth content of the column.
17. Evaporate each fraction to dryness and redissolve in a drop of HClO₄. Evaporate to dryness in a teflon beaker.

Gadolinium, europium and samarium were separated from the Abee sample by ion exchange, using a three column operation. Diaion SK#1, 100-200 mesh resin was used in all columns; the cation exchange columns were made of acril. The separation was performed by S. Yanagita, Department of Chemistry, University of Tokyo.

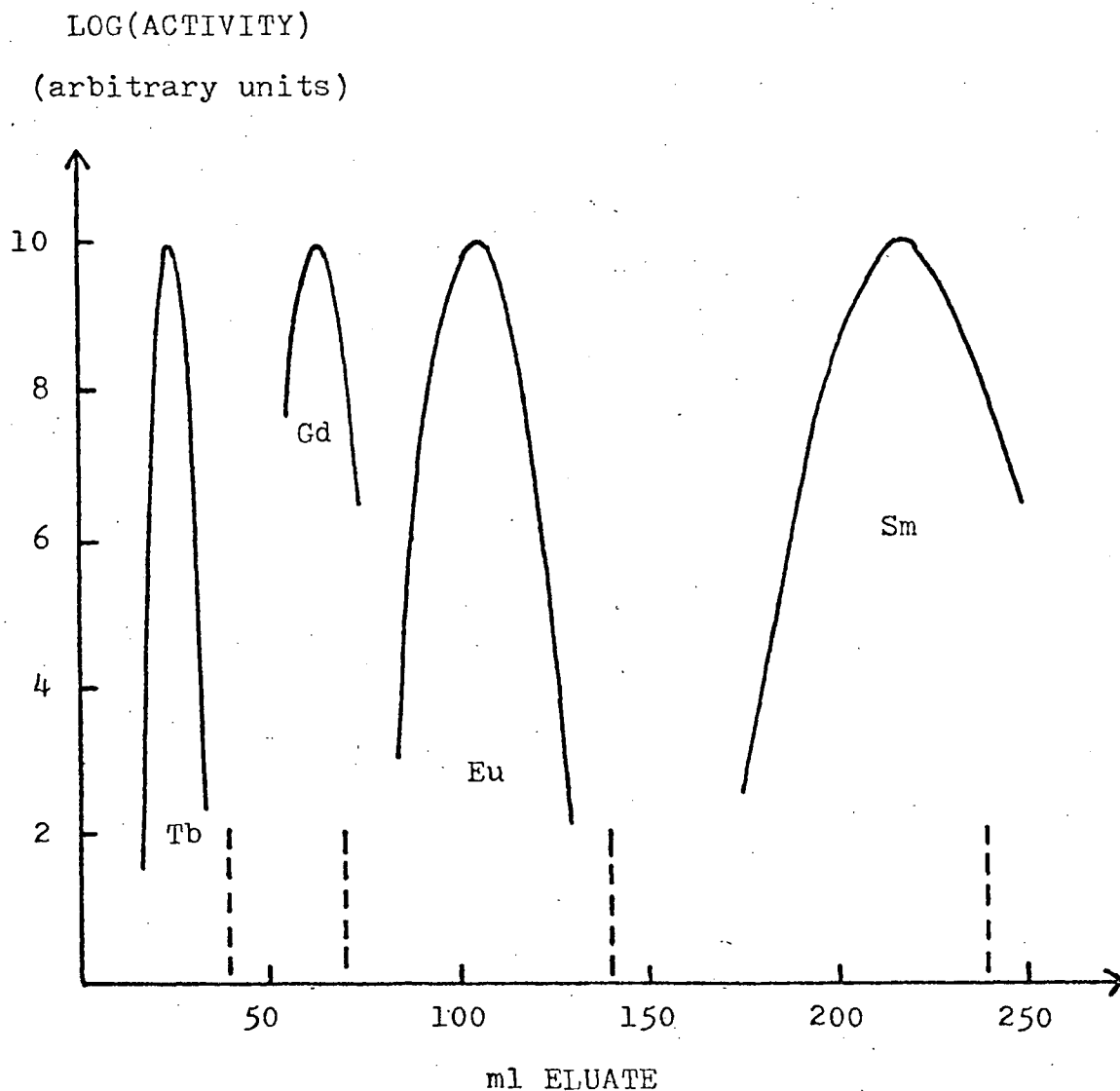


FIGURE 4-1. ELUTION CURVES FOR TB, GD, EU AND SM

Artificially-produced radioactive isotopes were used to calibrate the second ion exchange process (see Table 4-4). The elution curves were determined by monitoring the activity of the eluate and identifying individual radioactive isotopes of Tb, Gd, Eu and Sm. During the subsequent Abee separation, the Gd-AB, Eu-AB and Sm-AB fractions correspond to the 40-70, 70-140 and 140-240 ml fractions of the eluate. The calibration was performed by S. Yanagita, Department of Chemistry, University of Tokyo.

curves for the meteorite sample and the calibration run were not identical, possibly because of different concentrations of the rare earth elements in the two solutions. The three fractions Gd-AB, Eu-AB and Sm-AB were selected from the eluate to coincide with the calibrated elution curves for Gd, Eu and Sm respectively (see Figure 4-1). However, subsequent analyses in the mass spectrometer showed that most of the Gd from the meteorite was collected in the fraction Eu-AB, and a large portion of the Eu was in the fraction Sm-AB. The Gd-AB fraction contained some Gd (estimated to be $< .1 \mu\text{g}$) as well as Tb.

Small quantities of Eu, Sm, Nd, Ce, La and Ba were observed in all three fractions. Special care was required during the mass spectrometer analyses to minimize the effect of interfering elements on the spectra of Gd, Eu and Sm.

4.2 Preparation of Filaments

Although tantalum filaments were used for some of the preliminary analyses listed in Table 4-3, all other analyses were performed with rhenium filaments. The rhenium metal had a specified purity of 99.9%. Two single filament analyses (Gd-JZ1 and GE-AB) made use of zone-refined rhenium of very high purity. For these two analyses, GdO^+ ions were observed in the mass spectrometer at much lower temperatures ($\sim 1350^\circ \text{C}$) than was observed when the other (99.9% purity) rhenium was used ($\sim 1700^\circ \text{C}$).

The most critical impurities in the rhenium metal were Ba, La and Ce. These were reduced to tolerable levels by outgassing all filaments at 2000° C for one hour. This eliminated La and Ce completely while Ba was reduced to a contamination level which was only a small fraction of the Ba contamination in the samples themselves. The purity of all filaments used for analyses on the Abee meteorite was checked in the mass spectrometer, at temperatures well above operating conditions, prior to loading the samples.

All reagent analyses were performed with microgram quantities of Gd, Sm or Eu. The elements were studied separately, except for Sm and Eu which were occasionally analyzed together because of the lack of isobars for these elements. The samples were deposited on outgassed filaments as chlorides, and then converted to perchlorate salts on the filaments. For Gd single filament preparations, the filaments were subsequently heated in air to a dull red glow (in a dark room) to convert the salt to the oxide form, thereby increasing the production of GdO^+ ions in the mass spectrometer.

The Abee fractions were taken up in a drop of 3x distilled water, deposited on outgassed filaments, and evaporated to dryness. The complete Sm-AB fraction was loaded for one triple filament analysis of Sm. Most of the Eu-AB fraction was loaded for one triple filament analysis of Eu (at low side filament temperatures),

followed by an analysis of Gd in the same fraction (at higher temperatures). Approximately one half of the Gd-AB fraction was loaded for one triple filament analysis of Gd. The remainder of fractions Eu-AB and Gd-AB was combined for one single filament analysis of Gd. This latter analysis will be referred to as GE-AB.

4.3 Production of Ion Spectra with Minimum Interference

Operating pressures of 10^{-7} torr were maintained for all mass spectrometer analyses. Pressures approaching 2×10^{-8} torr were achieved for many analyses on the Abee fractions by thoroughly outgassing the instrument, and by allowing several hours for barium and other contaminants to be driven out of each sample at low filament temperatures. There was no substitute for slow heating of the filaments to increase the purity of the Gd, Sm and Eu in each sample.

None of the contaminants in the reagent samples caused significant spectral interference which could not be eliminated by careful heating of the sample filaments in the mass spectrometer.

For the meteorite analyses, however, it was not always possible to eliminate all interfering ions in this way. LaO^+ and Nd^+ ions interfered with the measurement of the Sm^+ spectrum during analysis Sm-AB, and LaO^+ ions interfered with the Gd^+ spectrum during analyses Eu-AB and Gd-AB. Fortunately, it was possible to monitor the intensity of the Nd^+ and LaO^+ ion beams

at masses 146 and 155 respectively, so that a correction could be made to separate these spectra from the Sm^+ spectrum computationally. The method of applying these corrections is discussed in Chapter 5. A similar correction for LaO^+ interference (at mass 155) with the Gd^+ spectrum could not be made because of the similar mass ranges for both ions. The only way in which the Gd^{155} isotopic abundance could be determined for the meteorite sample was by using the GdO^+ spectrum produced during the single filament analysis GE-AB.

CHAPTER 5

COMPUTER REDUCTION OF COMPLEX SPECTRA

5.1 Evaluation of Peak Heights

The method of recording spectra, and the definition of a scan (the unit record on magnetic tape) were discussed in Section 3.4. A representative scan of the Gd^+ spectrum was shown in Figure 3-3. A combined Eu^+ and Sm^+ spectrum is illustrated in Figure 5-1.

Data was recorded in digital form and a low-pass filter was used to remove high frequency noise from the spectrum (see Section 3.5). After filtering the data, a moving 5-point average was computed for the purpose of locating the time coordinates of the various peaks. At a position where the 5-point average was a maximum, the associated peak height (without the baseline removed) was chosen to be the largest value of the five points comprising the moving average. The true peak height was then computed by subtracting the recorded baseline which was represented, for each shunt in turn, by the best least-squares straight line fitting all (baseline) data (within a single scan) which was recorded while the scan direction was stationary. The corrected peak height and its associated time coordinate were subsequently used to represent the intensity and time of measurement of the component ion beam

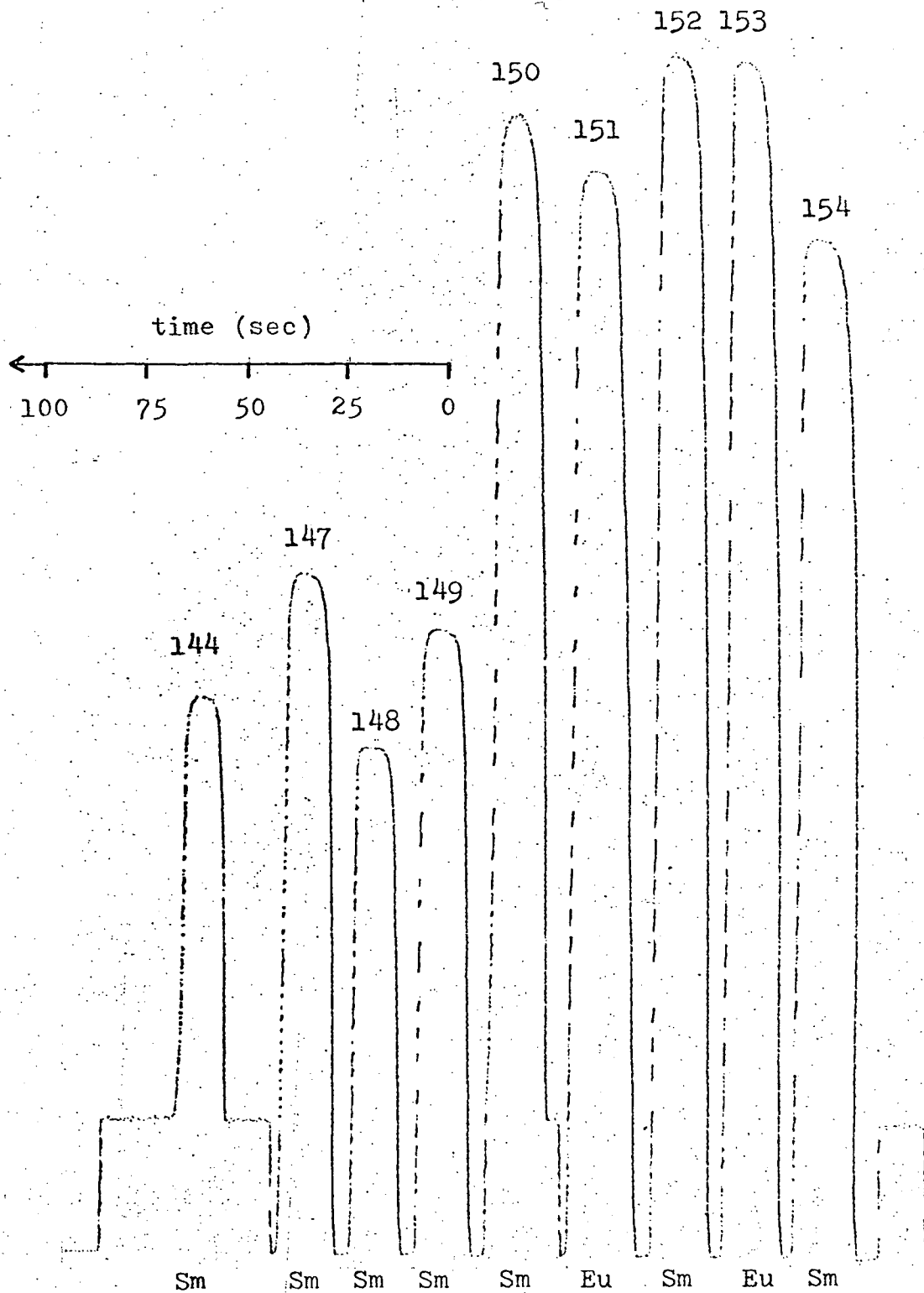


FIGURE 5-1. SLOW DISCONTINUOUS SCANNING

Down-mass portion of a scan showing the Eu and Sm spectra.

at a particular mass number.

The reduction of data from a single scan gave two measurements of the intensity of each peak in the spectrum.

By retaining a running time coordinate it was possible to combine measurements derived from a set of several successive scans and apply a correction for the continuous growth or decay of each type of ion during the set of scans.

5.2 Least Squares Reduction of a Set of Scans

Past experience in our mass spectrometer laboratory has shown that a third order polynomial provides a fairly good representation of the intensity of a single peak as a function of time t , i. e.

$$I(t) = a_1 + a_2 t + a_3 t^2 + a_4 t^3 \quad (5-1)$$

In order to minimize the errors introduced by this type of approximation it is desirable to make use of the fact that the isotopic composition of each type of ion remains essentially constant during a set of scans at fixed filament temperatures. As an example, the intensities I_1 and I_2 of the Eu^{151} and Eu^{153} component ion beams may be represented in the form

$$I_1(t) = r_1(b_1 + b_2 t + b_3 t^2 + b_4 t^3) \quad (5-2)$$

$$I_2(t) = r_2(b_1 + b_2 t + b_3 t^2 + b_4 t^3)$$

where r_1 and r_2 are proportional to the relative isotopic abundance values (one of which must be arbitrarily fixed, e. g.

$r_1 = 1.0$). These parameters are constant for the duration of a set of scans at fixed filament temperatures, except for minimal fractionation effects which are generally small ($< 0.05\%$ per unit mass difference) compared with statistical errors. The term in brackets is a polynomial representation of the growth or decay characteristics of both the Eu^{151} and Eu^{153} ion beams. Representation (5-2) requires the determination of only 5 parameters whereas 8 parameters would have been required if the constancy of the isotopic ratio had not been used as a constraint.

A suitable method for determining the optimum values of the parameters r_2, b_1, b_2, b_3, b_4 is one which minimizes the variance between the measured peak heights and their polynomial representation in equations (5-2). If p_{1k} and t_{1k} are the peak height and time of measurement of the Eu^{151} peak during the k^{th} measurement of that peak, and p_{2k}, t_{2k} are similar quantities for the Eu^{153} peak, then the function to be minimized may be represented in the form

$$\begin{aligned}
g(r_2, b_1, b_2, b_3, b_4) &= \sum_{k=1, 2n} \left\{ \left[p_{1k}^{-r_1} (b_1 + b_2 t_{1k} + b_3 t_{1k}^2 + b_4 t_{1k}^3) \right]^2 + \left[p_{2k}^{-r_2} (b_1 + b_2 t_{2k} + b_3 t_{2k}^2 + b_4 t_{2k}^3) \right]^2 \right\} \\
&= \sum_{k=1, 2n} \sum_{j=1, 2} \left[p_{jk}^{-r_j} \sum_{w=1, 4} b_w t_{jk}^{w-1} \right]^2 \quad (5-3)
\end{aligned}$$

where n is the number of scans in the set.

There are several possible sources of error when experimentally measuring any single peak intensity on the mass spectrometer: overshooting a peak when manually advancing the magnet current, making an error in shunt selection, sudden line transients, etc. These can readily be recognized on the chart record during an analysis. Provision has therefore been made for eliminating faulty peak measurements from the right hand side of equation (5-3). Such errors were, however, infrequent in practice.

The conditions which must be satisfied in order for $g(r_2, b_1, b_2, b_3, b_4)$ to be a minimum are:

$$\frac{\partial g}{\partial r_2} = \frac{\partial g}{\partial b_1} = \frac{\partial g}{\partial b_2} = \frac{\partial g}{\partial b_3} = \frac{\partial g}{\partial b_4} = 0 \quad (5-4)$$

These give rise to five non-linear equations in the variables r_2, b_1, b_2, b_3, b_4 . A solution is possible by a perturbation method provided a good first approximation may be obtained.

This is possible since the isotopic ratio r_1/r_2 is known to within a few per cent. If r_2 is initially treated as a constant $= \bar{r}_2$, then four linear equations may be obtained in the variables $\bar{b}_1, \bar{b}_2, \bar{b}_3, \bar{b}_4$. These can easily be solved directly to give good estimates of b_1, b_2, b_3, b_4 .

At this stage, equations (5-4) may be linearized using the new variables $\Delta r_2, \Delta b_1, \Delta b_2, \Delta b_3, \Delta b_4$ where

$$\begin{aligned} r_2 &= \bar{r}_2 + \Delta r_2 & b_3 &= \bar{b}_3 + \Delta b_3 \\ b_1 &= \bar{b}_1 + \Delta b_1 & b_4 &= \bar{b}_4 + \Delta b_4 \\ b_2 &= \bar{b}_2 + \Delta b_2 \end{aligned} \quad (5-5)$$

The linearized equations (5-4) may be solved to get an improved estimate of r_2, b_1, b_2, b_3, b_4 . Several iterations may be performed in this way until r_2, b_1, b_2, b_3, b_4 are all known with sufficient precision ($< .01\%$ was considered more than adequate).

Figure 5-2 shows a direct comparison between the measured peak heights and the solution polynomials $I_1(t)$ and $I_2(t)$ for a set of scans of the Eu^+ spectrum. The quality of the polynomial fit is quite good, even when the beam intensity shows strong growth and/or decay characteristics. In practice, however, the beam intensity usually changed monotonically during a set of scans, with a total variation of 20% or less.

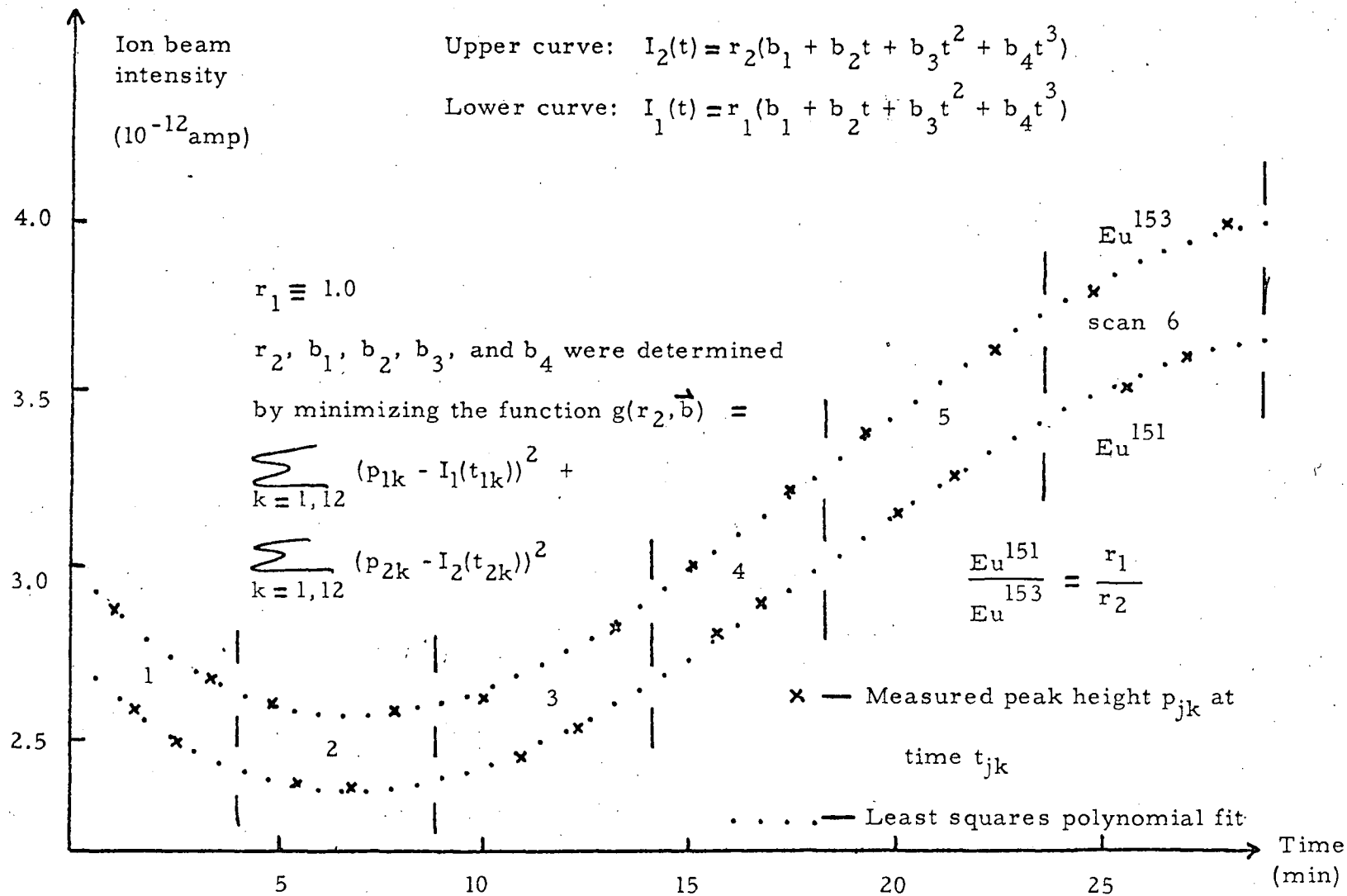


FIGURE 5-2. POLYNOMIAL REPRESENTATION OF ION BEAM INTENSITY

The Eu^{151} and Eu^{153} ion beams have been represented by polynomials of degree 3 for a set of scans.

The above example illustrates the basic numerical procedure employed in this research to compute the least squares polynomial representation of the various peak intensities associated with ions of a single element. For the majority of analyses it was not necessary to apply a correction for the effect of interfering ion spectra. However, whenever spectral interference was observed, care was taken to record additional peaks if possible, so that the growth or decay characteristics of each additional ion species could be determined and subsequently removed.

Where several ion spectra occur in a set of scans the equations to be solved are more complex. Also, not all isotopic ratios should be treated as variables. Where interfering ions form only a small percentage of the total beam, it is more reliable to fix their isotopic composition at published values than to treat them as additional variables in the least squares solution.

In the general case, where there are m elements and q different peaks, the function which replaces (5-3) as the sum of squares to be minimized is

$$g(\vec{r}, \vec{b}) = \sum_{j=1, q} \sum_{k=1, 2n} \left[p_{jk} - \sum_{i=1, m} r_{ij} \sum_{w=1, 4} b_{iw} t_{jk}^{w-1} \right]^2$$

(5-6)

where p_{jk} is the k^{th} measurement of the j^{th} peak at time

t_{jk} ; r_{ij} is the relative isotopic abundance associated with peak j and element i ; and b_{i1} , b_{i2} , b_{i3} , b_{i4} are the coefficients of the growth polynomial for element i .

The vector \vec{b} represents all b_{iw} ($i = 1, m$; $w = 1, 4$) while the vector \vec{r} represents only those abundance values which are to be treated as variables in the least squares solution. For convenience, a new logical function f_{ij} may be defined such that f_{ij} is false only when r_{ij} is to be treated as a variable. This means that \vec{r} represents all r_{ij} ($i = 1, m$; $j = 1, q$) for which f_{ij} is false. (Note that equation (5-6) includes the common situation where isotopes of more than one element exist at a given mass number.)

The function $g(\vec{r}, \vec{b})$ is a minimum when

$$\frac{\partial g}{\partial b_{iw}} = 0 \quad i = 1, m; \quad w = 1, 4 \quad (5-7)$$

$$\text{and } \frac{\partial g}{\partial r_{ij}} = 0 \quad i = 1, m; \quad j = 1, q; \quad f_{ij} = \text{false}$$

These equations reduce to

$$\sum_{j=1, q} \sum_{k=1, 2n} (p_{jk} - \sum_{i=1, m} r_{ij} \sum_{w=1, 4} b_{iw} t_{jk}^{w-1}) r_{uj} t_{jk}^{v-1} = 0$$

$$u = 1, m; \quad v = 1, 4$$

$$\sum_{k=1, 2n} (p_{vk} - \sum_{i=1, m} r_{iv} \sum_{w=1, 4} b_{iw} t_{vk}^{w-1}) (\sum_{w=1, 4} b_{uw} t_{vk}^{w-1}) = 0$$

$$u = 1, m; \quad v = 1, q; \quad f_{uv} = \text{false} \quad (5-8)$$

Equations (5-8) may be linearized and solved by a perturbation method similar to the previous example, in order to obtain solution vectors \vec{r} and \vec{b} .

5.3 Calculation of Means and Standard Deviations of Isotopic Ratios for a Set of Scans

It is evident from the discussion in the previous section that isotopic ratios resulted directly from the solution of equations (5-8). In the case of the example given earlier one could readily calculate the isotopic ratio $\text{Eu}^{151}/\text{Eu}^{153} = r_1/r_2$. However, there is no easy way to estimate the error in this ratio apart from comparing results from several sets of scans. This was considered inadequate because of large variations in the stability of an ion beam from one set of scans to another. Differences in sample purity and abundance, and variations in the operating characteristics of the mass spectrometer also contribute to real variations in the precision achieved. (When isotopic ratios and standard deviations were calculated by the method to be described in this section, a test for homogeneity of variance from one set of scans to another showed convincingly that there were real variations in the variance.) A method was therefore devised for estimating the standard deviation of each isotopic ratio for a set of scans.

The polynomial representation of the intensity of peak j as a function of time is

$$I_j(t) = \sum_{i=1,m} r_{ij} \sum_{w=1,4} b_{iw} t^{w-1} \quad (5-9)$$

Suppose the dominant component in this peak belongs to the element represented by subscript $i = s$. The isotopic abundance coefficient associated with peak j and element s is r_{sj} . If we assume that, on the k^{th} measurement of peak j , the difference between the measured peak height p_{jk} and the polynomial value $I_j(t_{jk})$ may be regarded as a semi-independent measurement of r_{sj} , then we can transform equation (5-9) into the form

$$p_{jk} = r'(s, j, k) \sum_{w=1,4} b_{sw} t_{jk}^{w-1} + \sum_{\substack{i=1,m \\ i \neq s}} r_{ij} \sum_{w=1,4} b_{iw} t_{jk}^{w-1}$$

$$\Rightarrow r'(s, j, k) = (p_{jk} - \sum_{\substack{i=1,m \\ i \neq s}} r_{ij} \sum_{w=1,4} b_{iw} t_{jk}^{w-1}) / \sum_{w=1,4} b_{sw} t_{jk}^{w-1} \quad (5-10)$$

where $r'(s, j, k)$ is a semi-independent measurement of the coefficient r_{sj} at time t_{jk} .

Consider the case where we are interested in measuring the isotopic ratio $R = r_{sj_1} / r_{sj_2}$, the ratio of isotopes of element s occurring at peaks j_1 and j_2 . Because of the symmetry of spectra within a single scan it is reasonable to compute one estimate of R for each scan. Let R_i ($i = 1, 2, \dots, n$) be the computed estimate of

R during scan i. Then

$$R_1 = \frac{r'(s, j_1, 1) + r'(s, j_1, 2)}{r'(s, j_2, 1) + r'(s, j_2, 2)}$$

$$R_2 = \frac{r'(s, j_1, 3) + r'(s, j_1, 4)}{r'(s, j_2, 3) + r'(s, j_2, 4)} \quad (5-11)$$

etc.

This method of computing semi-independent estimates of each isotopic ratio was applied to all ratios of interest for the three elements Eu, Sm and Gd. The combined data, for each isotopic ratio, was then presented in the form

$$\bar{R} = \sum_{i=1, n} R_i / n$$

$$\sigma = \left(\sum_{i=1, n} (R_i - \bar{R})^2 / (n-1) \right)^{\frac{1}{2}}$$

$$\bar{\sigma} = \sigma / \sqrt{n} \quad (5-12)$$

where \bar{R} is the mean value of the isotopic ratio, σ is an estimate of the standard deviation of each measurement R_i , and $\bar{\sigma}$ is an estimate of the standard deviation of the mean.

5.4 Calculation of Fractionation-Corrected Parameters

In the precise determination of isotopic abundances, care must be taken to account for any processes which might cause mass discrimination in the sample at any stage prior to, or during, the measurement of an ion beam in the mass spectrometer. In the present research, mass fractionation was detected by comparing isotopic ratios for several sets of scans obtained at one or more filament temperatures. The largest fractionation effect observed was 0.3% per unit mass difference. This represents the change in isotopic composition of the ion beam over the extremes of sample filament temperatures for which a measureable ion beam could be produced. For all three elements, Eu, Sm, and Gd, the process proceeded toward the enrichment of the heavier isotopes in the ion beam (or the depletion of the lighter isotopes) with increasing filament temperatures and time.

In agreement with simple theory (see Ozard and Russell, 1970) and common experience, the fractionation effect for a particular element was observed to satisfy the equations

$$X \doteq X_N (1 + (m_2 - m_1) \beta)$$

$$Y \doteq Y_N (1 + (m_4 - m_3) \beta) \quad (5-13)$$

where X and Y are measured isotopic ratios (for the same element)

corresponding to the mass ratios m_1/m_2 and m_3/m_4 respectively; X_N and Y_N are normalized (or fractionation-corrected) isotopic ratios; β is the fractional change in the isotopic ratios per unit mass difference (due to fractionation). $\beta \ll 1$.

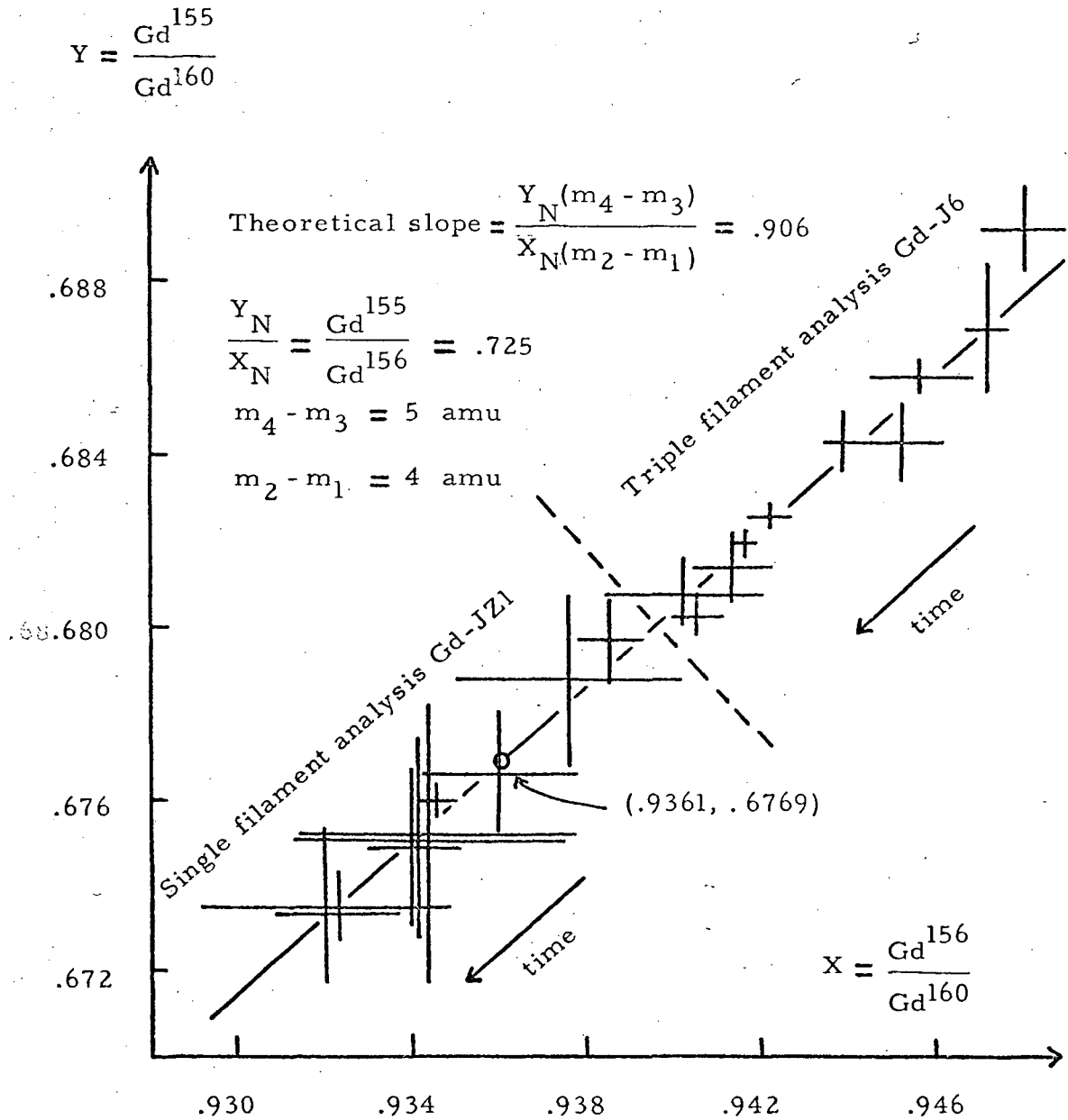
The quantity β may be eliminated from equations (5-13) to give

$$\bar{Y} = Y_N + \frac{Y_N(m_4 - m_3)}{X_N(m_2 - m_1)} (X - X_N) \quad (5-14)$$

Figure 5-3 shows the close agreement between the slope predicted by equation (5-14) and the measured isotopic ratios. The solid line illustrated in this plot was forced to pass through the point (.9361, .6769) adopted by Eugster et al (1970a) for terrestrial gadolinium. The published standard deviation of the latter coordinate is 0.01% while the ratio $Gd^{156}/Gd^{160} = .9361$ is the value which they used for normalization of all other Gd isotopic ratios. The normalization process involves measuring two isotopic ratios, X and Y, assigning a specific value to X_N (e. g. $X_N = Gd^{156}/Gd^{160} = .9361$) and solving equation (5-14) for Y_N .

An alternative method may be used to remove the effect of fractionation from measured isotopic ratios. Equation (5-14) may be rewritten in the form

FIGURE 5-3. MASS SPECTROMETER FRACTIONATION



The data points represent measured isotopic ratios for individual sets of scans (usually 6 scans per set). Data are shown for one single filament analysis (after correction for the isotopic composition of oxygen) and for one triple filament analysis on the same sample. The solid line has the theoretical fractionation slope and passes through the point (.9361, .6769).

$$\begin{aligned}
 \left(\frac{Y}{Y_N}\right) &= 1 + \alpha \left(\frac{X-X_N}{X_N}\right) \\
 &\doteq \left[1 + \left(\frac{X-X_N}{X_N}\right)\right]^\alpha \\
 &= \left(\frac{X}{X_N}\right)^\alpha \\
 \Rightarrow \frac{Y}{X^\alpha} &= \frac{Y_N}{X_N^\alpha} \equiv \gamma = \text{constant} \quad (5-15)
 \end{aligned}$$

where $\alpha = (m_4 - m_3)/(m_2 - m_1)$.

By measuring appropriate isotopic ratios for the elements Gd and Sm it is possible to evaluate parameters which are corrected for fractionation and are also very sensitive to the neutron capture processes $\text{Gd}^{155}(n, \gamma)\text{Gd}^{156}$, $\text{Gd}^{157}(n, \gamma)\text{Gd}^{158}$ and $\text{Sm}^{149}(n, \gamma)\text{Sm}^{150}$. Three parameters which satisfy these conditions are given in Table 5-1. Each parameter is sensitive to only one capture process. The value of all three parameters (A, B and C) will be greater for samples which have been exposed to a larger neutron flux. They should be constant, however, for all analyses performed on the same sample. Since there are only two isotopes of Eu, no correction for fractionation was possible.

The method of computing a normalized ratio Y_N or

TABLE 5-1. FRACTIONATION-CORRECTED PARAMETERS

X	Y	$\alpha = \frac{m_4 - m_3}{m_2 - m_1}$	$\chi = \text{Constant}$
$\frac{\text{Gd}^{156}}{\text{Gd}^{155}}$	$\frac{\text{Gd}^{160}}{\text{Gd}^{156}}$	$\frac{1}{4}$	$A = \frac{\text{Gd}^{156}}{\text{Gd}^{155}} \left(\frac{\text{Gd}^{156}}{\text{Gd}^{160}} \right)^{\frac{1}{4}}$
$\frac{\text{Gd}^{158}}{\text{Gd}^{157}}$	$\frac{\text{Gd}^{160}}{\text{Gd}^{158}}$	$\frac{1}{2}$	$B = \frac{\text{Gd}^{158}}{\text{Gd}^{157}} \left(\frac{\text{Gd}^{158}}{\text{Gd}^{160}} \right)^{\frac{1}{2}}$
$\frac{\text{Sm}^{150}}{\text{Sm}^{149}}$	$\frac{\text{Sm}^{152}}{\text{Sm}^{150}}$	$\frac{1}{2}$	$C = \frac{\text{Sm}^{150}}{\text{Sm}^{149}} \left(\frac{\text{Sm}^{150}}{\text{Sm}^{152}} \right)^{\frac{1}{2}}$

Each of the fractionation-corrected parameters A, B and C is sensitive to a particular neutron capture process. The sensitivities of the parameters are somewhat greater than the simple ratios (X in above table) from which they are derived. The sensitivities relative to the isotopic ratios $\text{Gd}^{155}/\text{Gd}^{156}$, $\text{Gd}^{157}/\text{Gd}^{158}$ and $\text{Sm}^{149}/\text{Sm}^{150}$ are $\frac{9}{8}$, $\frac{5}{4}$ and $\frac{5}{4}$ respectively. The isotopes Gd^{160} and Sm^{152} are not significantly changed by neutron irradiation.

a fractionation-corrected parameter γ will now be given.

Let X_i and Y_i be the appropriate isotopic ratios computed for scan i ($i = 1, 2, \dots, n$) from equations (5-11). The corresponding normalized ratio Y_{Ni} (or parameter γ_i) was computed from equation (5-14) (or equation (5-15)). The mean \bar{Y}_N (or $\bar{\gamma}$) and standard deviations σ and $\bar{\sigma}$ were then computed from equations (5-12).

5.5 Correction for the Isotopic Composition of Oxygen

All triple filament analyses were performed on elemental Eu^+ , Sm^+ or Gd^+ ions. A few single filament analyses were performed using the GdO^+ spectrum, and a subsequent correction was required for the small contribution of the O^{17} and O^{18} isotopes. The corrections required for all isotopes at masses where GdO^{16+} ions were measured are given by the equations

$$\begin{aligned}
 (168/176)_{\text{corr}} &= 1.00232 \times (168/176)_{\text{meas}} \\
 (170/176)_{\text{corr}} &= 1.00213 \times (170/176)_{\text{meas}} \\
 (171/176)_{\text{corr}} &= 1.00226 \times (171/176)_{\text{meas}} \\
 (172/176)_{\text{corr}} &= 1.00183 \times (172/176)_{\text{meas}} \\
 (173/176)_{\text{corr}} &= 0.99990 \times (173/176)_{\text{meas}} \\
 (174/176)_{\text{corr}} &= 1.00040 \times (174/176)_{\text{meas}} \quad (5-16)
 \end{aligned}$$

The ratios indicated by the subscript 'meas' are the measured ratios (uncorrected for mass fractionation) while those indicated by the subscript 'corr' are the ratios which would have been measured if oxygen were monoisotopic (i. e. only GdO^{16+} ions present). The corrections in equations (5-16) are based on the isotopic ratios $\text{O}^{18}/\text{O}^{16} = .00204$ and $\text{O}^{17}/\text{O}^{16} = .00037$ given by Nier (1950). Eugster et al (1970a) have estimated that the maximum error in any of the correction factors in equations (5-16) is less than 0.005%, which is negligible compared to the experimental uncertainty.

CHAPTER 6

INTERPRETATION OF METEORITIC AND TERRESTRIAL ISOTOPIC
RATIOS6.1 Terrestrial Gadolinium

The results of several isotopic analyses on terrestrial samples Gd-J and Gd-US are summarized in Table 6-1 and Figures 6-1 and 6-2. (Complete data for individual scans is given in Appendix III). Within the experimental uncertainty of the measured isotopic ratios (shown as two standard deviations of the mean) there is no significant difference between the terrestrial samples derived from two different geographic locations (eastern US and Rio de Janeiro). Furthermore, the good agreement with the terrestrial ratios obtained by Eugster et al (1970a) supports the view that terrestrial Gd is of fairly uniform isotopic composition when samples representing large segments of the earth are compared.

It is interesting to note that the displacement between the mean terrestrial values obtained by Eugster et al (1970a) and those obtained by the present writer (Figures 6-1 and 6-2) is similar to that which would be produced by a difference in exposure to thermal neutrons. (The calculation of the slope of each of the theoretical correlation lines for thermal neutron capture is given in Appendix IV.) In the writer's opinion, no significance can be attached to this apparent

TABLE 6-1. ISOTOPIC RATIOS OF GD IN TERRESTRIAL SAMPLES

Analyses	$\frac{\text{Gd}^{155}}{\text{Gd}^{160}}$ *	$\frac{\text{Gd}^{157}}{\text{Gd}^{160}}$ *	$\frac{\text{Gd}^{158}}{\text{Gd}^{160}}$ *	A	B
	Gd-J1, J4, J5 triple fil.	.67686 ±.00015	.71620 ±.00016	1.13620 ±.00044	1.36030 ±.00027
Gd-J6 triple fil.	.67685 ±.00026	.71593 ±.00014	1.13566 ±.00021	1.36029 ±.00054	1.69038 ±.00054
Gd-JS1, JS2 single fil.	.67693 ±.00022	.71575 ±.00029	1.13586 ±.00063	1.36001 ±.00042	1.6910 ±.0013
Gd-JZ1 single fil. zone-ref. Re	.67702 ±.00025	.71591 ±.00023	1.13570 ±.00018	1.35999 ±.00050	1.69070 ±.00069
Gd-US triple fil.	.67682 ±.00015	.71639 ±.00048	1.13595 ±.00034	1.36026 ±.00027	1.6900 ±.0016
Average (this work)	.67688 ±.00008	.71601 ±.00009	1.13576 ±.00012	1.36021 ±.00016	1.69060 ±.00034
Eugster et al (1970a) single fil. zone-ref. Re	.67692 ±.00009	.71589 ±.00004	1.13590 ±.00009	1.36024 ±.00018	1.69108 ±.00031
Collins et al (1956)	.683	.717	1.124	1.348	1.662

* Fractionation correction normalized to $\text{Gd}^{156}/\text{Gd}^{160} = .9361$.

All single filament analyses used the Gd^{156} spectrum, and a correction was made for the isotopic composition of oxygen.

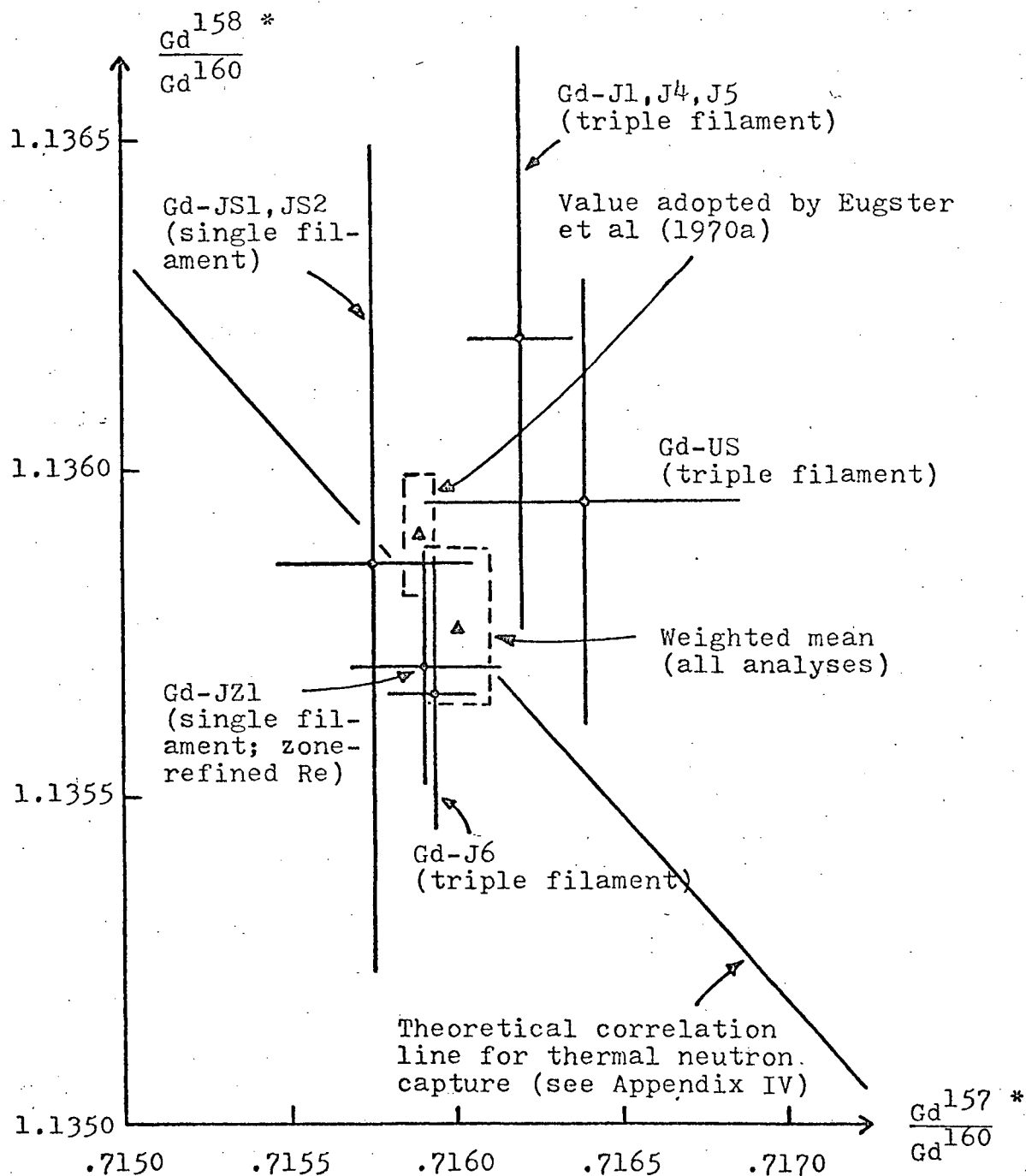
The fractionation-corrected, irradiation-sensitive parameters A and B have the values

$$A = \frac{\text{Gd}^{156}}{\text{Gd}^{155}} \left(\frac{\text{Gd}^{156}}{\text{Gd}^{160}} \right)^{\frac{1}{4}}$$

$$B = \frac{\text{Gd}^{158}}{\text{Gd}^{157}} \left(\frac{\text{Gd}^{158}}{\text{Gd}^{160}} \right)^{\frac{1}{2}}$$

Only statistical errors are shown. They correspond to two standard deviations of the mean.

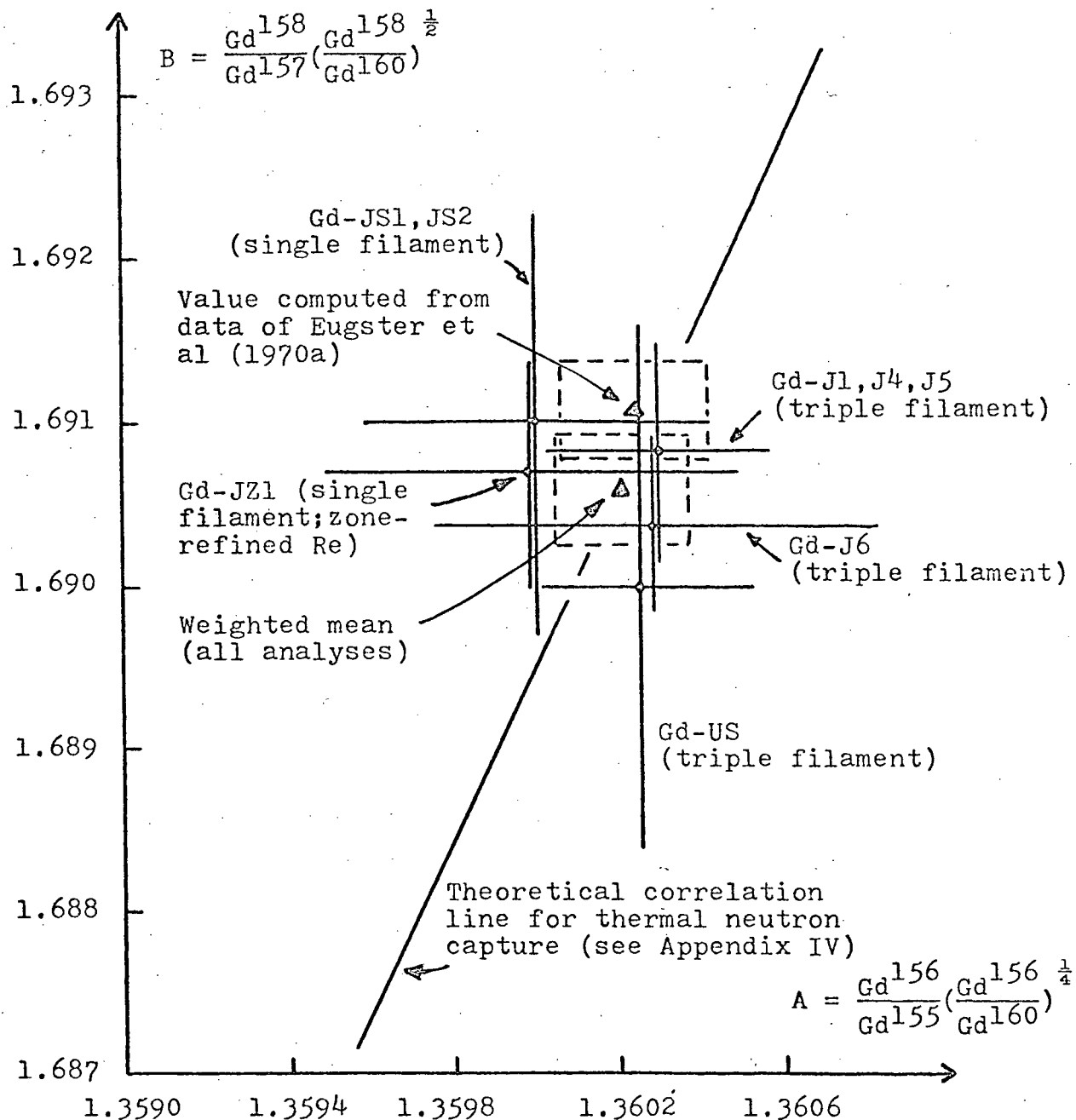
FIGURE 6-1. ISOTOPIC ANALYSES ON TERRESTRIAL GADOLINIUM



Gd^{158}/Gd^{160} * vs Gd^{157}/Gd^{160} * for all terrestrial analyses.

* Fractionation correction normalized to $Gd^{156}/Gd^{160} = .9361$.

FIGURE 6-2. CORRELATION BETWEEN B AND A FOR TERRESTRIAL GD



Correlation between irradiation-sensitive parameters B and A for all terrestrial analyses.

correlation since all the isotopic ratios agree within the 95% confidence limits shown. Also, the specified errors correspond to statistical errors only. The analyses were performed on different mass spectrometers using significantly different techniques for scanning, recording and reducing mass spectra. The good agreement for all isotopic ratios suggests that any external errors must be small; however, the existence of any bias in measurement on either instrument could only increase the absolute error of the isotopic ratios.

For the purpose of comparison between Gd in terrestrial and meteoritic samples, terrestrial Gd will be assumed to have the isotopic composition given by the average values in Table 6-1. The mean μ and standard deviation σ_{μ} were computed, for each column in turn, from the equations

$$\mu = \frac{\sum_{i=1,n} \frac{x_i}{\sigma_i^2}}{\sum_{i=1,n} \frac{1}{\sigma_i^2}}$$

$$\sigma_{\mu} = \frac{1}{\sum_{i=1,n} \frac{1}{\sigma_i^2}} \quad (6-1)$$

where x_i and σ_i are the mean and standard deviation for the i^{th} entry in the column.

TABLE 6-2. ADDITIONAL RESULTS FOR TERRESTRIAL GADOLINIUM

	$\frac{\text{Gd}^{152} \text{ *+}}{\text{Gd}^{160}}$	$\frac{\text{Gd}^{154} \text{ *+}}{\text{Gd}^{160}}$	$\frac{(\text{Gd}^{156})}{\text{Gd}^{160} \text{ meas}}$
This work ^a	.00918 ^b ±.00005	.09961 ^c ±.00007	.943 ^d ±.004 ^e
Eugster et al (1970a)	.00928 ±.00002	.09975 ±.00002	
Value currently used for normali- zation of all other ratios			.9361 ^f (adopted arbitrarily)

Per cent abundances of terrestrial Gd

	<u>Gd¹⁵²</u>	<u>Gd¹⁵⁴</u>	<u>Gd¹⁵⁵</u>	<u>Gd¹⁵⁶</u>	<u>Gd¹⁵⁷</u>	<u>Gd¹⁵⁸</u>	<u>Gd¹⁶⁰</u>
This work #	.203	2.191	14.86	20.52	15.67	24.80	21.76
Eugster et al (1970a) *	.2029	2.1809	14.800	20.466	15.652	24.835	21.863
Collins et al (1956)	.205	2.23	15.1	20.6	15.7	24.5	21.6

* Fractionation correction normalized to $\text{Gd}^{156}/\text{Gd}^{160} = .9361$.

+ Errors represent two standard deviations of the mean.

Normalized to $\text{Gd}^{156}/\text{Gd}^{160} = .943$.

a Based on all triple filament analyses on terrestrial samples Gd-J and Gd-US.

b Average of three data sets (representing three different analyses)

c Average of eight data sets (more than one analysis).

d Simple average for 23 data sets (several analyses).

e One standard deviation of a set (not of the mean).

f Based on single filament analyses.

Analyses on the terrestrial sample Gd-J also showed the absence of any detectable bias between data obtained by the triple filament method (using the Gd^+ spectrum) and single filament data (using the GdO^+ spectrum and correcting for the isotopic composition of oxygen). Furthermore, there was no significant inter-analysis error which could be attributed to loading the same sample (Gd-J in solution form) onto different filaments.

There are two additional Gd isotopes which were seldom measured: Gd^{152} and Gd^{154} . Their terrestrial abundances are reported in Table 6-2. Also, the mean value of the unnormalized Gd^{156}/Gd^{160} ratio is reported in Table 6-2 for all triple filament analyses on terrestrial Gd. This value is 0.7% higher than the value currently used for normalization of all other ratios (after Murthy et al, 1970, and Eugster et al, 1970); the current value was determined from single filament analyses only. The triple filament value is undoubtedly closer to the absolute abundance ratio, and should therefore be used when calculating the absolute abundance of the Gd isotopes (see Table 6-2).

6.2 Gadolinium in the Abee Meteorite

Three separate analyses were performed on Gd from the Abee meteorite. Two of these used the triple filament configuration and the Gd^+ spectrum. Because of LaO^+ interference at mass 155 (see Tables III-6 and III-7 of Appendix III) it was not

possible to measure the Gd^{155} abundance. Consequently, only Gd^{157}/Gd^{160} *, Gd^{158}/Gd^{160} * and the parameter B could be determined. The third analysis was performed by the single filament technique. Because the GdO^+ spectrum was employed, there was no interference from LaO^+ ions, and it was possible to determine both the Gd^{155}/Gd^{160} * ratio and the parameter A. The average values for the three analyses were computed from equations (6-1) and are shown in Table 6-3.

It is apparent that none of the Gd isotopic ratios differs by more than 0.06% from the terrestrial value. This also applies to the irradiation-sensitive parameters A and B. A plot of Gd^{157}/Gd^{160} * vs. Gd^{158}/Gd^{160} * (Figure 6-3) shows that the 95% confidence limits for the Abee and terrestrial data overlap, and the slope of the line passing through the two points is not the same as the slope of the theoretical correlation line for thermal neutron capture. On a plot of B vs A, the data points for Abee and for terrestrial Gd appear to be distinctly different on the basis of the 95% confidence limits. However, the slope of the line through the two points is almost perpendicular to the theoretical correlation line for thermal neutron capture.

Within the experimental uncertainty, there is no significant thermal neutron irradiation anomaly for Gd in the Abee sample (when compared with the earth). This result is disappointing because of its implications for the class of enstatite chondrites as a whole.

The failure to observe an anomaly means that there is no definitive experimental evidence to support the theories of Miya-shiro and Mason: that differences in the oxidation state of chondrites result from differences in their mean distances from the sun during the early history of the solar system. At the same time, their theories have not been disproved since other essential conditions must also have been satisfied in order to produce a detectable irradiation anomaly. These will be discussed in Section 6.6.

Precise analyses on meteorites have also been performed by Eugster et al (1970a). Their results are plotted in Figures 6-3 and 6-4. (The data for Pasamonte and Norton County are weighted means of several published analyses.) Only the Norton County achondrite contains Gd of significantly different isotopic composition from terrestrial Gd. It lies along the theoretical correlation line for thermal neutron capture. An irradiation anomaly clearly exists; it has been attributed to the long cosmic ray exposure age of the Norton County meteorite. The Weekeroo Station iron has an even longer cosmic ray exposure age, but its smaller mass and inferior moderating properties presumably resulted in the production of very few thermal neutrons (Eugster et al 1970a). The other meteorites include another iron (Copiapo), an achondrite (Pasamonte) and a bronzite chondrite (Forest City).

TABLE 6-3. ISOTOPIC COMPOSITION OF GD IN THE ABEE METEORITE

Chemical fraction	$\frac{\text{Gd}^{155} *}{\text{Gd}^{160}}$	$\frac{\text{Gd}^{157} *}{\text{Gd}^{160}}$	$\frac{\text{Gd}^{158} *}{\text{Gd}^{160}}$	A	B
Eu-AB ^a triple fil.		.71614 ±.00024	1.13533 ±.00035		1.68987 ±.00065
Gd-AB ^b triple fil.		.71607 ±.00032	1.1351 ±.0011		1.6878 ±.0036
GE-AB ^c single fil. zone-ref. Re	.67652 ±.00024	.71598 ±.00012	1.13557 ±.00031	1.36092 ±.00044	1.68991 ±.00058
Average (this work)	.67652 ±.00024	.71602 ±.00010	1.13545 ±.00023	1.36092 ±.00044	1.68986 ±.00043
Terrestrial (this work)	.67688 ±.00008	.71601 ±.00009	1.13576 ±.00012	1.36021 ±.00016	1.69060 ±.00034

* Fractionation correction normalized to $\text{Gd}^{156}/\text{Gd}^{160} = .9361$.

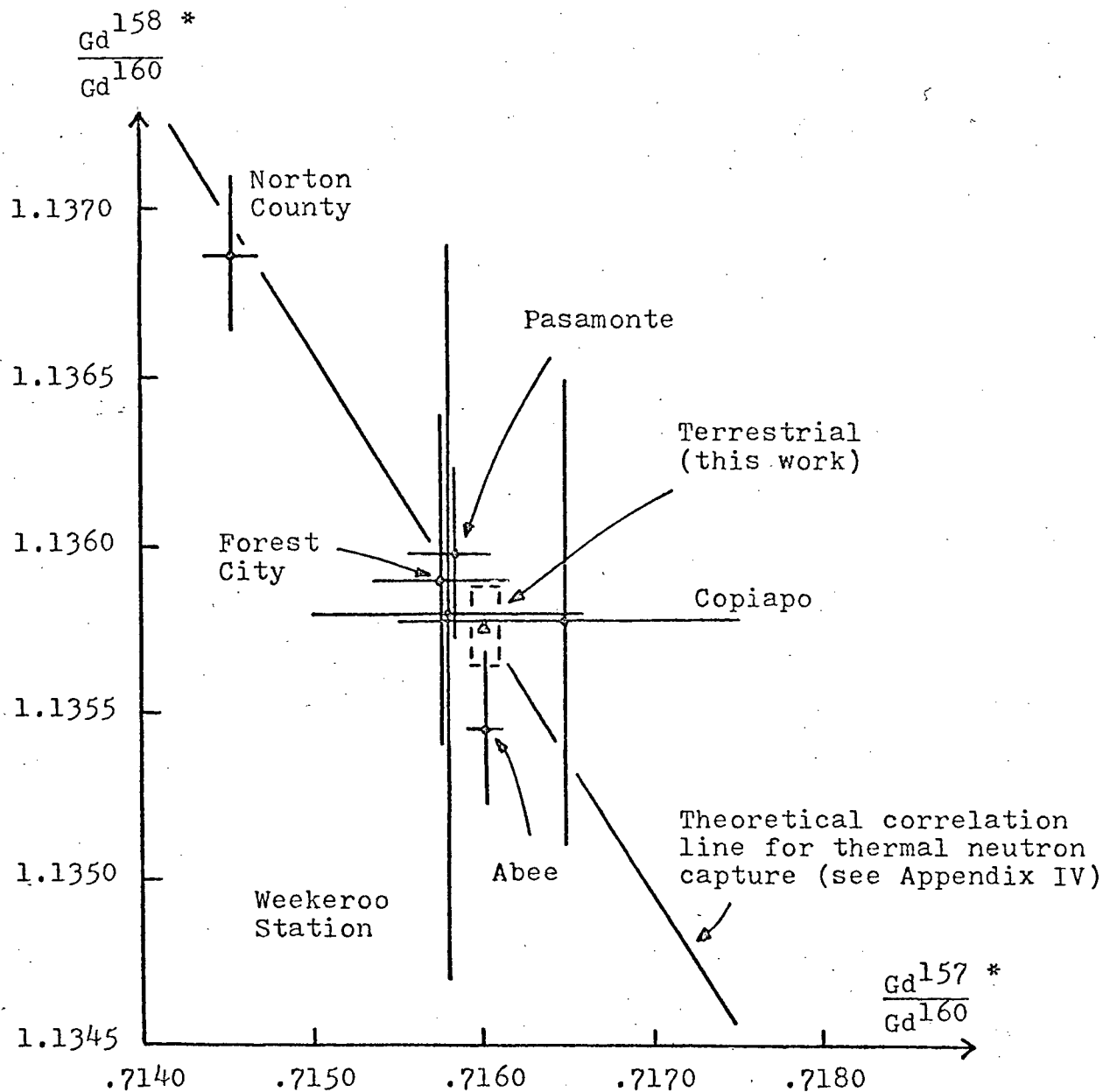
a The fraction Eu-AB contained most of the Gd as well as the Eu from the original 9.5 g Abee sample. There was no spectral interference between Eu^+ and Gd^+ ions.

b The fraction Gd-AB contained very little Gd (estimated to be $< 0.1 \mu\text{g}$ on the basis of the observed Gd^+ beam intensity).

c Not all of the Eu-AB and Gd-AB fractions were loaded for the first two analyses above. The remainder, approximately 20% of fraction Eu-AB and 30% of fraction Gd-AB, was combined on a single (zone-refined) rhenium filament for analysis GE-AB.

See the footnotes to Table 6-1 for definitions of A and B.

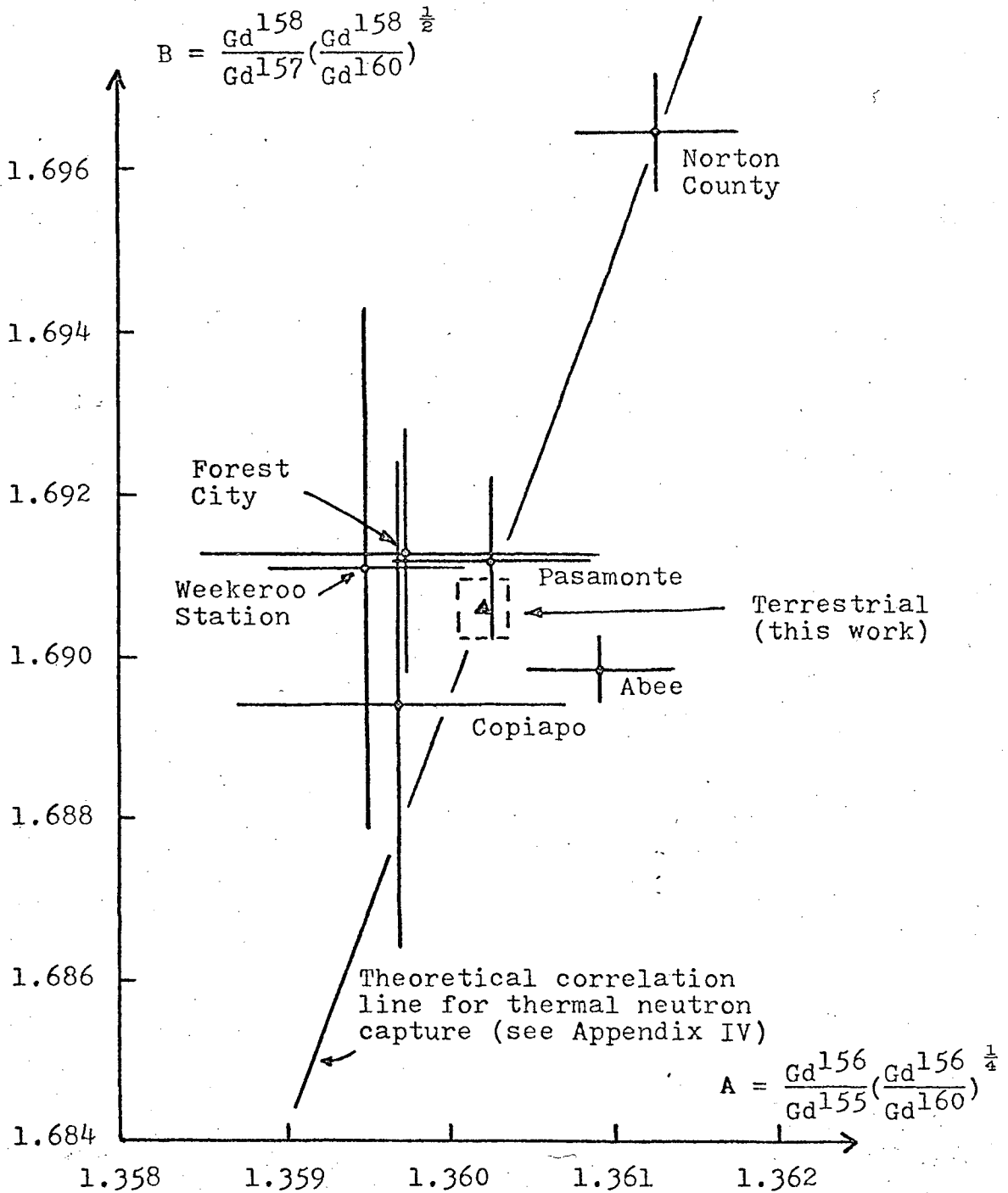
FIGURE 6-3. CORRELATION OF GD ISOTOPES IN METEORITES



Gd^{158}/Gd^{160} * vs Gd^{157}/Gd^{160} * for Abee (this work) and previous meteorite analyses (Eugster et al, 1970a).

* Fractionation correction normalized to $Gd^{156}/Gd^{160} = .9361$.

FIGURE 6-4. CORRELATION BETWEEN A AND B IN METEORITES



Correlation between irradiation-sensitive parameters B and A for Abee (this work) and previous meteorite analyses (Eugster et al, 1970a).

6.3 Do Abee and Terrestrial Gadolinium have Similar Composition?

The apparent difference between the values of A and B for the Abee and terrestrial samples may be significant. It cannot be explained by thermal neutron capture alone. Nor can it be the result of mass fractionation during the chemical preparation of the Abee sample, provided the fractionation process was governed by a simple mass dependence.

It is possible that the Abee meteorite was derived from a region where the relative abundance of the nuclides was slightly different from that of pre-terrestrial matter. Apart from meteorite analyses, the only other Gd isotopic studies on extra-terrestrial samples are the lunar analyses of Eugster et al (1970b) and Lugmair (1970). Their lunar and terrestrial data clearly lie along the correlation line for thermal neutron capture (see Figure 1-4). This is to be expected if the earth and moon are genetically related, and were produced from the same pool of nuclides. The meteorites may, however, have been produced from slightly different source material.

Alternatively, the apparent difference between the terrestrial and Abee values of A and B may be the result of poor statistical estimates of the standard deviations for the Abee data, or they may result from additional sources of error.

There are three possible sources of error which may have introduced a bias in the measurement of Abee Gd relative to terrestrial

Gd. Trace amounts of one or more interfering ions may have been superimposed upon the Gd^+ or GdO^+ spectra. The most probable ions are BaF^+ , BaCl^+ , LaCl^+ and LaO_2^+ . None of these alone would give the observed anomaly, however, and no systematic change in any of the $\text{Gd}^{155-158}/\text{Gd}^{160}$ * ratios was observed. Nevertheless, the possibility of ion interference cannot be ruled out completely.

A second possibility is that the baseline was not constant over the mass range 155-160 (or 171-176 for GdO^+ ions). Since baselines were measured only at the ends of each spectrum (see Section 3.4), the existence of any baseline irregularity within the spectral range would not have been detected. Baselines were routinely checked between peaks at the beginning of each analysis, but distortion of up to 0.1 to 0.2% would not have been detected during a visual reading of the digital voltmeter. The most probable causes of baseline distortion are secondary electrons and/or scattered ions (most likely Ba^+) in the vicinity of the ion detector.

Baseline distortion was a major source of error for Sm^+ analyses (see Section 6.5); it was attributed to Ba^+ ions. However, the mass range of Sm is much closer to that of Ba; distortion from Ba^+ ions should be significantly less in the higher Gd mass range. Also, Gd was vapourized at higher filament temperatures than Sm; it was therefore possible to burn off more of the residual Ba before

producing a Gd^+ ion beam. Although baseline distortion may be a source of error during Gd analyses, it does not explain the similar isotopic ratios obtained for Abee when using the Gd^+ and GdO^+ spectra.

A third source of error is pressure scattering in the mass spectrometer. This creates a slight tail on either side of the spectral peaks. Direct measurement of peak profiles showed that the height of the tail at a position $\frac{1}{2}$ mass unit above or below a spectral peak was $< 0.1\%$ of the peak height for operating pressures $\leq 1.0 \times 10^{-7}$ torr. The corresponding tail height 1 mass unit away was $< 0.03\%$. These errors represent a significant bias in measurement which varied with the operating pressure. The maximum errors, which could be attributed to pressure scattering, in the ratios Gd^{155}/Gd^{160}^* , Gd^{157}/Gd^{160}^* , Gd^{158}/Gd^{160}^* , A and B were 0.01%, 0.04%, 0.03%, 0.05% and 0.01% respectively. The slope of the error line associated with pressure scattering would be similar to that of a line passing through the Abee and Copiapo data points in Figures 6-3 and 6-4. The intersections of these error lines with the theoretical correlation lines for thermal neutron capture are below the terrestrial points. This would suggest, if anything, that Abee was exposed to fewer thermal neutrons during its history than the earth was. However, the most sensitive parameter B would not change by more than 0.01%, and the difference

between the mean terrestrial and Abee values would not exceed 0.06%.

6.4 Interpretation of Europium Data

When the present study of the rare earths was initiated, the extent of mass spectrometer fractionation was not known for the triple filament technique. The magnitude of the fractionation effect (i. e. the deviation from the absolute ratios) was less than that which was observed with the single filament technique, but the variation during an analysis was the same for both techniques: approximately 0.3% variation per unit mass difference (see Figure 5-3).

Since Eu has only two isotopes, a simple normalization process could not be used. Table 6-4 shows the mean values obtained for all analyses on terrestrial (Eu-J and Eu-US) and Abee (Eu-AB) samples. Two selective methods of combining the data decreased the dispersion due to fractionation, but it was not completely eliminated. The first method combined data which was obtained for the initial 10-20% of the sample (based on the time-integrated beam intensity). The second method used only the results of analyses for which the data-taking intervals were uniformly distributed over the lifetime of the Eu^+ ion beam. Recording data for the full duration of the sample minimized bias due to fractionation and provided the most reliable estimate of the absolute isotopic ratio for each sample.

It is apparent that there is no gross difference between terrestrial and Abee Eu. The slightly higher ratio for the Abee sample

TABLE 6-4. ISOTOPIC COMPOSITION OF TERRESTRIAL AND ABEE EU

<u>Data selection</u>	<u>Average Eu¹⁵¹/Eu¹⁵³ isotopic ratio</u>		
	<u>Eu-J</u> (Brazil ore)	<u>Eu-US</u> (U.S. ore)	<u>Eu-AB</u> (Abee)
Average for all analyses	.917 (20) ±.001	.914 (20) ±.004	.918 (38) ±.002
Average for sets obtained with initial 10-20% of sample only	.9182 (5) ±.0006	.9183 (4) ±.0010	.9195 [#] (24) ±.0004
Average for analyses for which data was obtained for the full duration of the sample	.9155 (9) ±.0009	.9160 (9) ±.0018	.9173 [#] (11) ±.0022

Errors correspond to one standard deviation of a set. The standard deviation of the mean would not be a suitable representation of the error because it would not account for real variations in the isotopic ratio in the Eu⁺ ion beam due to mass fractionation.

The numbers in brackets represent the total number of sets (usually 6 scans per set) used to calculate the means and standard deviations.

Murthy et al (1970) found that $\text{Eu}^{151}/\text{Eu}^{153} = .9147$ for single filament analyses on terrestrial europium.

The analysis of the Eu-AB fraction extended over three days. Since the mass spectrometer was turned off overnight, sample emission was not continuous. This appears to have introduced an error in determining the sample depletion from the time-integrated beam intensity.

probably reflects a bias in measurement: most data sets for analysis Eu-AB were obtained with the initial portion of the sample. In view of the large variation caused by fractionation (0.6%) during the analyses, no significance can be assigned to the apparent difference of 0.14 - 0.17% between terrestrial and Abee Eu.

6.5 Interpretation of Samarium Data

The combined results of several analyses of samples Sm-J and Sm-US are recorded in Table 6-5. Each entry is the weighted mean of a minimum of six sets of scans of the Sm^+ spectrum. The two terrestrial samples have the same isotopic composition within the experimental uncertainty (shown as two standard deviations of the mean). The average terrestrial value was calculated for each ratio in turn from equations (6-1).

A comparison between terrestrial and Abee Sm is shown in Table 6-6. Although the irradiation-sensitive parameter D appears to have the same value for both samples, several of the isotopic ratios appear to differ. The apparent difference cannot be attributed to thermal neutron capture.

The discrepancy between the terrestrial and Abee results is almost certainly due to baseline distortion. A depression of the baseline in the mass range 144 - 147, and a moderate enhancement at higher masses, was clearly observed in association with an intense Ba^+ ion beam. However, the characteristic shape and

TABLE 6-5. ISOTOPIC COMPOSITION OF SM IN TERRESTRIAL SAMPLES

Sample	$\frac{\text{Sm}^{144} *}{\text{Sm}^{152}}$	$\frac{\text{Sm}^{148} *}{\text{Sm}^{152}}$	$\frac{\text{Sm}^{149} *}{\text{Sm}^{152}}$	$\frac{\text{Sm}^{150} *}{\text{Sm}^{152}}$	$\frac{\text{Sm}^{154} *}{\text{Sm}^{152}}$	$D = \frac{\text{Sm}^{150}}{\text{Sm}^{149}} \left(\frac{\text{Sm}^{150}}{\text{Sm}^{152}} \right)^{\frac{1}{2}}$
Sm-J # (Brazil ore)	.11647 ±.00015	.42323 ±.00013	.51943 ±.00013	.27725 ±.00009	.84836 ±.00026	.28106 ±.00014
Sm-US # (U.S. ore)	.11689 ±.00031	.42322 ±.00025	.51936 ±.00031	.27728 ±.00023	.84852 ±.00080	.28096 ±.00040
Average #	.11655 ±.00014	.42323 ±.00012	.51942 ±.00012	.27725 ±.00008	.84838 ±.00025	.28105 ±.00013
Murthy et al (1963)	.118	.426	.522	.280	.858	.283

* Fractionation correction normalized to $\text{Sm}^{147}/\text{Sm}^{152} = .5650$ (mean value for all terrestrial analyses for this work).

Baseline distortion was recognized to be a source of bias in measurement for all of these analyses. This was substantiated by comparing the values obtained for the parameter D when using the two spectral ranges 149-152 and 144-154. In both cases the baseline was measured at positions $\frac{1}{2}$ mass above the high mass peak and $\frac{1}{2}$ mass below the low mass peak only. No subsequent correction for the distortion was possible without having measured baselines between intermediate peaks.

TABLE 6-6. ISOTOPIC COMPOSITION OF SAMARIUM IN THE ABEE METEORITE

Sample	$\frac{\text{Sm}^{144} \star}{\text{Sm}^{152}}$	$\frac{\text{Sm}^{148} \star}{\text{Sm}^{152}}$	$\frac{\text{Sm}^{149} \star}{\text{Sm}^{152}}$	$\frac{\text{Sm}^{150} \star}{\text{Sm}^{152}}$	$\frac{\text{Sm}^{154} \star}{\text{Sm}^{152}}$	$D = \frac{\text{Sm}^{150}}{\text{Sm}^{149}} \left(\frac{\text{Sm}^{150}}{\text{Sm}^{152}} \right)^{\frac{1}{2}}$
Abee # (Sm-AB)	.11585 ^a ±.00009	.42284 ^a ±.00016	.51871 ±.00022	.27709 ^a ±.00017	.84976 ^b ±.00061	.28116 ^a ±.00023
Terrestrial #	.11655 ±.00014	.42323 ±.00012	.51942 ±.00012	.27725 ±.00008	.84838 ±.00025	.28105 ±.00013

* Fractionation correction normalized to $\text{Sm}^{147}/\text{Sm}^{152} = .5650$.

Baseline distortion (mainly secondary electrons from Ba^{138} ions) is the probable cause of the major discrepancies between Abee and terrestrial samples. The distortion was greatest in the lower mass range 144-147.

a After computationally subtracting the Nd^+ spectrum which was monitored at mass 146. ($\text{Nd}^+/\text{Sm}^+ < 0.02$).

b After computationally subtracting the LaO^+ spectrum which was monitored at mass 155. ($\text{LaO}^+/\text{Sm}^+ < 0.005$).

magnitude of the distortion were highly variable from one analysis to another, so that a correction could not be made without having measured baselines between individual peaks. The good agreement obtained for the two terrestrial samples is probably a result of their similar chemical composition. Baseline distortion introduced a bias in measurement, but it was approximately the same for both samples.

The existence of baseline distortion was proven by analyzing terrestrial Sm samples using only the shorter mass range 149-152, and computing the parameter D. This was observed to have the values $.28038 \pm .00019$ for Sm-J and $.28036 \pm .00010$ for Sm-US. The difference between these values, which are undoubtedly closer to the true value, and the average value in Table 6-6 is significant. It can only be explained by the fact that the baselines were measured at different places for the two spectral ranges.

The existence of baseline distortion would lead to a further source of error for the Abee analyses. A correction for the Nd^+ beam was made by monitoring the intensity of the peak at mass 146. Since baseline distortion was greatest in the vicinity of this peak, the intensity of the Nd^+ ion beam would not have been correctly determined, and a subsequent error would result wherever isobars of Nd and Sm occurred. The largest error for Sm would occur at mass 144.

6.6 Conclusions

An investigation of Gd, Eu and Sm in the Abee enstatite chondrite, and in two terrestrial ores, has shown that there are no significant isotopic anomalies for Abee which could be attributed to one or more of the thermal neutron capture processes: $Gd^{155}(n, \gamma)Gd^{156}$, $Gd^{157}(n, \gamma)Gd^{158}$, $Sm^{149}(n, \gamma)Sm^{150}$, $Eu^{151}(n, \gamma)Eu^{152}$, $Eu^{153}(n, \gamma)Eu^{154}$. The isotopic ratios Gd^{155}/Gd^{156} , Gd^{157}/Gd^{158} , Sm^{149}/Sm^{150} and Eu^{151}/Eu^{153} are identical for the three samples studied within maximum experimental uncertainties of 0.15%, 0.10%, 0.3% and 0.3% respectively. These estimates include statistical errors, as well as errors introduced by possible sources of bias in measurement (e. g. baseline distortion, pressure scattering and/or uncorrected fractionation).

On the basis of the Gd^{157}/Gd^{158} ratio, we may conclude that the maximum differential thermal neutron irradiation between the terrestrial and Abee samples is 3×10^{15} neutrons/cm² for the uniform irradiation model of Figure 2-2. It is reasonable to assume that this conclusion applies to the Abee meteorite as a whole, when compared with the earth. In terms of the irradiation models discussed in Chapter 2, we may exclude the regions above the curves in Figures 2-1 and 2-2 corresponding to a Gd^{157}/Gd^{158} anomaly $> 0.1\%$ from the family of possible solutions for the irradiation histories of the Abee meteorite and the earth.

If the time-integrated thermal neutron flux associated with the irradiation phase was as large as the FGH hypothesis predicted (i. e. $\int_{nE} = 4 \times 10^{21}$ neutrons/cm²), then the Gd¹⁵⁷/Gd¹⁵⁸ ratio is more sensitive to the fraction of the material which was irradiated than to the differential irradiation of the primitive chondritic and terrestrial matter (Fowler et al, 1962; Burnett et al, 1966; Murthy et al, 1963). The absence of a Gd anomaly > 0.1% implies that the irradiated fractions of the Abee and terrestrial source material were identical within 2%. This applies to the FGH model only, where it has been assumed that approximately 5% of the primitive terrestrial matter was irradiated.

Apart from uniform irradiation and/or dilution of the source material, alternative explanations could account for the absence of significant Gd¹⁵⁷/Gd¹⁵⁸ anomalies: efficient shielding of most planetary material inside large bodies having diameters >> 50 meters; the lack of sufficient hydrogen to thermalize spallation-produced neutrons; or the absence of an irradiation phase of sufficient intensity to generate detectable anomalies.

Apart from the highly reduced state of the Abee meteorite, there is no clear evidence to suggest that this extra-terrestrial object originated in the inner region of the solar system. If anything, the isotopic composition of Gd in the meteorite suggests that Abee received less irradiation than the earth during its previous

history. This evidence would therefore favour the view that Abee had its origin at a greater distance from the sun, possibly in the asteroid belt.

Since the asteroid belt is a natural source of meteorites, any explanation of the gradation in the oxidation states of chondrites would receive stronger support from the available evidence if it assumed an origin in this region of the solar system. One interesting possibility which has received considerable attention recently (see Larimer et al, 1970) is that variations in the oxidation state of chondrites result from differences in their spatial distribution during gravitational settling of primordial material toward the orbital plane of the nebula.

APPENDIX I

EFFECT OF NEUTRON CAPTURE ON GD, SM AND EU

The probability of a nuclear process is generally expressed in terms of a cross section σ which has the dimensions of an area. The unit commonly used is the barn, which is defined as 10^{-24} cm^2 .

A simple definition of the thermal neutron capture cross section of a specific nuclide (e. g. Gd^{157}) may be deduced from classical theory. Consider a beam of thermal neutrons striking a thin target in which the beam is attenuated only infinitesimally. If R_i is the number of capture processes occurring in the target per unit time for nuclide i then the corresponding reaction cross section is defined by the equation

$$R_i = I n_i \sigma_i d$$

where I is the number of incident thermal neutrons per unit time

n_i is the number of target nuclei of nuclide i per unit volume

σ_i is the thermal neutron capture cross section for nuclide i

d is the target thickness.

In this thesis we are interested in thermal neutron capture processes occurring in the primitive material of the solar system.

The size of the planetesimals, the duration of the assumed irradiation period, and the magnitude of the neutron flux are all unknown.

However, for heavy isotopes with large thermal neutron capture cross sections it is possible to establish a clear relationship between isotopic composition and the time-integrated thermal neutron flux.

Let N_0 be the initial atom abundance of a particular nuclide in primordial material which later accreted to form a planetary body (e. g. the earth or the parent body of the Abee meteorite). The quantity N_0 represents the total number of atoms of the nuclide prior to irradiation. If thermal neutron capture is the dominant process causing a change in the abundance of the nuclide during irradiation, then the atom abundance N_i after irradiation by n neutrons may be deduced from the differential equation (after Fowler et al, 1962)

$$\frac{dN_i}{dn} = - \frac{\sigma_i N_i f_r}{\sum_A \sigma_A N_A} \quad (I-1)$$

where σ_i is the thermal neutron capture cross section for the nuclide under consideration

f_r is the fraction of the incident neutrons which is captured by the irradiated material. The remaining fraction $(1-f_r)$ includes those neutrons which escape from the irradiated material or undergo β decay.

$\sum_A \sigma_A N_A$ represents the total cross sectional target area presented by all nuclides.

Let n_{total} be the total number of neutrons produced during irradiation. Then, integration of equation (I-1) yields

$$N_f = N_o \exp \left\{ \frac{-\sigma_i f_r n_{\text{total}}}{\sum_A \sigma_A N_A} \right\} \quad (\text{I-2})$$

where N_f is the final atom abundance of the nuclide i which has been depleted by neutron capture.

So far, no mention has been made of the energy distribution of the neutrons. In the thermal range, the neutron capture cross sections of most nuclides are inversely proportional to the velocity of the incident neutrons. Hence, it is evident from equation (I-2) that the velocity terms would cancel out, leaving N_f essentially independent of the neutron energy distribution, provided it is in the thermal range. For the purposes of this thesis, however, we have chosen to separate the exponent in equation (I-2) into two factors: σ_i and ψ_n . We have chosen σ_i to be the cross section for neutron capture, assuming a thermal neutron velocity of 2200 m/sec (or 20°C). The parameter ψ_n is defined as

$$\psi_n = \left\{ \frac{f_r n_{\text{total}}}{\sum_A \sigma_A N_A} \right\}_{20^\circ\text{C}} \quad (\text{I-3})$$

This is simply the time-integrated thermal neutron flux (at 20°C)

for all neutrons which undergo capture. We may now write equation (I-2) in the form

$$N_f - N_o = - N_o \left[1 - \exp(-\sigma_i \psi_n) \right] \quad (\text{I-4})$$

By introducing another parameter, the dilution factor F_d (after Fowler et al, 1962), we may account for the possibility that only a fraction $\frac{1}{F_d}$ of the primordial material was irradiated. The remainder was effectively shielded within planetesimals having dimensions of the order of one meter or greater. Subsequent mixing of the two fractions during accretion to form a larger planetary body would yield

$$\Delta N = N_f - N_o = -\frac{N_o}{F_d} \left[1 - \exp(-\sigma_i \psi_n) \right] \quad (\text{I-5})$$

Equation (I-5) gives the net decrease in the abundance of a nuclide undergoing neutron capture. For (n, γ) reactions (which includes all reactions on Gd, Sm and Eu under consideration here), equation (I-5) also gives the net increase in the neighbouring higher mass nuclide resulting from this process. Let R_o and R be the initial and final isotopic abundance ratios for masses m and $m+1$. Then

$$R = \frac{N_{fm}}{N_{f,m+1}} = \frac{N_{om} - (N_{om}/F_d) [1 - \exp(-\sigma_m \psi_n)]}{N_{o,m+1} + (N_{om}/F_d) [1 - \exp(-\sigma_m \psi_n)]}$$

$$\Rightarrow R = \frac{F_d R_o - R_o [1 - \exp(-\sigma_m \psi_n)]}{F_d + R_o [1 - \exp(-\sigma_m \psi_n)]} \quad (I-6)$$

Equation (I-6) may be applied to each of the isotopic ratios Gd^{155}/Gd^{156} , Gd^{157}/Gd^{158} and Sm^{149}/Sm^{150} . Two independent (n, γ) reactions may contribute to a change in the Eu^{151}/Eu^{153} ratio (see Table 1-1). Therefore, for this ratio we have

$$R = \frac{F_d R_o - R_o [1 - \exp(-\sigma_{151} \psi_n)]}{F_d - [1 - \exp(-\sigma_{153} \psi_n)]} \quad (I-7)$$

It is evident from equations (I-6) and (I-7) that each of the present-day isotopic ratios mentioned above may be regarded as a function of R_o , F_d and ψ_n . The cross sections are all known. Let R_E and R_M be the present-day values of a particular ratio in terrestrial ores and in meteoritic material respectively. If these materials were exposed to previous irradiation by integrated neutron fluxes of ψ_{nE} and ψ_{nM} , where the dilution factors were F_{dE} and F_{dM} respectively, then

$$R(R_o, F_{dE}, \psi_{nE}) = R_E \quad (I-8)$$

$$R(R_o, F_{dM}, \psi_{nM}) = R_M \quad (I-9)$$

In equations (I-8) and (I-9) it has been assumed that the initial isotopic ratios were the same for both pre-terrestrial and pre-meteoritic materials.

Consider the case where it is just possible to detect a difference of 0.1% between the terrestrial and meteoritic isotopic ratios R_E and R_M respectively. The lower limit of detection is given by

$$\left| \frac{R_M - R_E}{R_E} \right| = \left| \frac{R(R_o, F_{dM}, \psi_{nM}) - R(R_o, F_{dE}, \psi_{nE})}{R(R_o, F_{dE}, \psi_{nE})} \right| = .001$$

$$(\text{= } 0.1\% \text{ detectable difference}) \quad (I-10)$$

Figures 2-1 and 2-2 illustrate particular solutions of equations (I-8) and (I-10) for specific values of the dilution factors. The curves for Figure 2-1 represent the solution of the equations

$$R(R_o, 20, \psi_{nE}) = R_E \quad (I-11)$$

$$(\text{= } .632 \text{ for the } Gd^{157}/Gd^{158} \text{ ratio})$$

and

$$\left| \frac{R(R_o, 20, \psi_{nM}) - R(R_o, 20, \psi_{nE})}{R(R_o, 20, \psi_{nE})} \right| = .001 \quad (I-12)$$

The parameter R_o was eliminated from equations (I-11) and (I-12), and the solution curve for ψ_{nE} and ψ_{nM} was plotted in the form

$$\left| (\psi_{nM} - \psi_{nE}) / \psi_{nE} \right| \text{ vs } \psi_{nE}$$

The sensitivity of the Gd^{157} / Gd^{158} ratio to differential irradiation of pre-meteoritic and pre-terrestrial material is illustrated for the case $F_{dE} = F_{dM} = 1$ in Figure 2-2. The requirement that $R_o \geq 0$, combined with the present-day ratio $R_E = .632$, places an upper limit on the value of ψ_{nE} which will satisfy the equation

$$R(R_o, 1, \psi_{nE}) = .632 \quad (I-13)$$

This is illustrated in Figure 2-2.

APPENDIX II

SECOND ORDER FOCUSsing SHIMS

Increased sensitivity, without loss of resolution may be achieved by improving the focussing properties of the analyzer magnet to permit the use of an ion beam with larger angular divergence. First order focussing results from using plane surfaces at the pole faces where the ion beam enters and leaves the magnet (at normal incidence and emergence). By suitably contouring one or both of these surfaces it is possible to produce a sharper focus at the collector. A variety of methods for achieving second order focussing have been reviewed by Barnard (1953).

One simple method involves the use of cylindrical rather than plane surfaces for the magnet pole faces. For a symmetric 90 deg sector magnet, similar to the one used by the present writer, the ideal radius of curvature of the pole faces is identical to the orbital radius of the central ion trajectory within the magnet. An alternative procedure adopted by the writer is to use one plane surface and one cylindrical surface, where the latter has a radius equal to one half the orbital radius (Figure II-1).

Two cylindrical shims were designed to fit onto the existing pole face on the collector side of the main electromagnet. The shims were positioned on either side of the analyzer tube, and provision was made for adjusting them to enable precise focussing

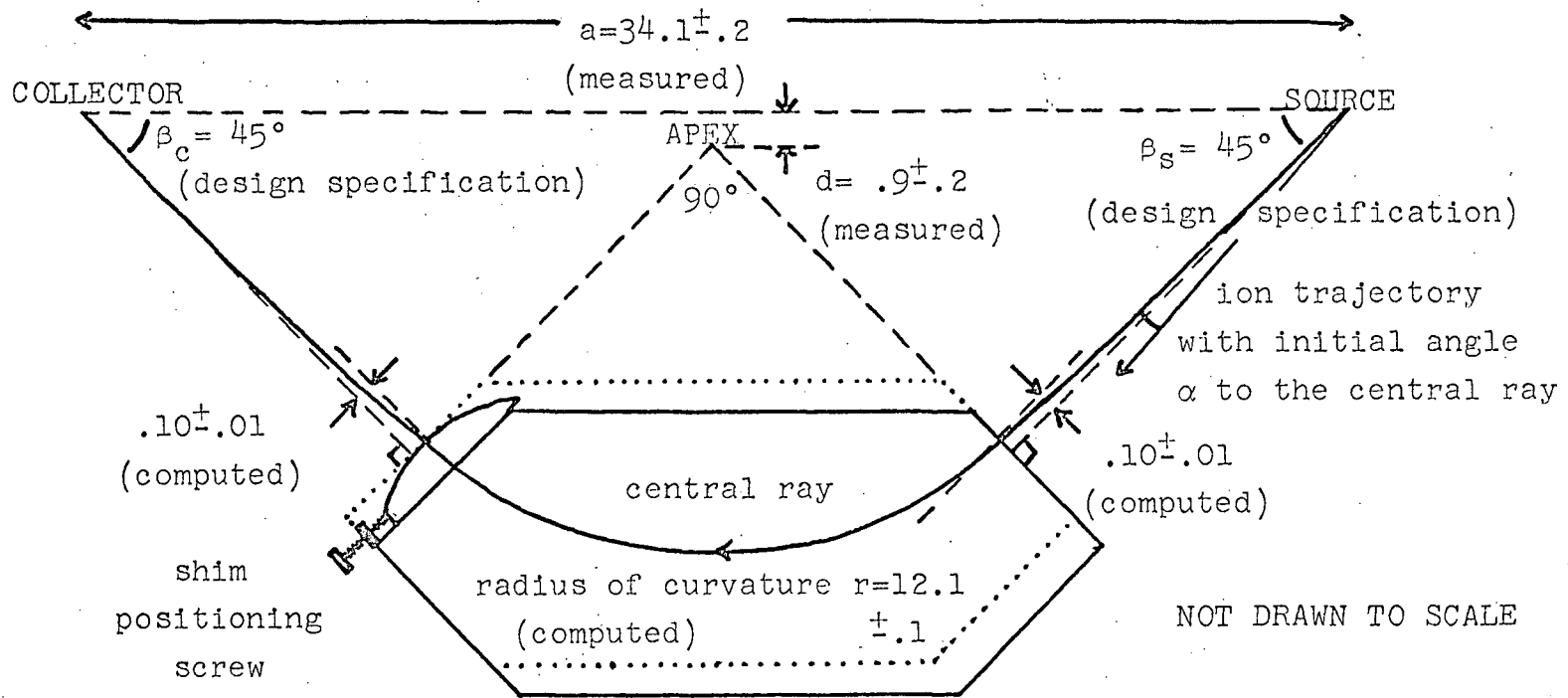


FIG. II-1 MODIFICATION OF MAIN ELECTROMAGNET TO ACCOMMODATE FOCUSING SHIMS

The dotted contour shows the original magnet position. By moving the main magnet and adding two cylindrical shims (7.0 inch radius) the path of the central ray remains unchanged. All distances are specified in inches.

experimentally. No alteration of the main magnet was necessary except for repositioning to compensate for the additional thickness of the magnet shims.

In order to apply a correction for the effect of the fringing magnetic fields on both sides of the magnet, the field intensity was determined in the median plane along the path of the central ray. The theoretical method of Coggeshall (1947) was used to calculate the field close to the magnet, and measured field values were employed at distant points. The resulting contour of the fringing field is shown in Figure II-2.

While the magnet was in the position of best focus for first order focussing, the parameters a and d (see Figure II-1) were measured. The large error of .2 inch in each measurement reflects the uncertainty in determining the effective positions of minimum beam width at the source and collector. Taking into account the uncertainties in a and d , the trajectory equation was integrated through the known magnetic field, and the radius of curvature of the central ray was computed to be $r = 12.1^{+.1}$ inch. Trajectories were computed for several ions having initial angles of inclination to the central ray in the range $-4^\circ < \alpha < 4^\circ$. For each trajectory the required change in path length (within the magnetic field) which would bring the trajectory to perfect focus at the collector, was computed. This led to the determination of the

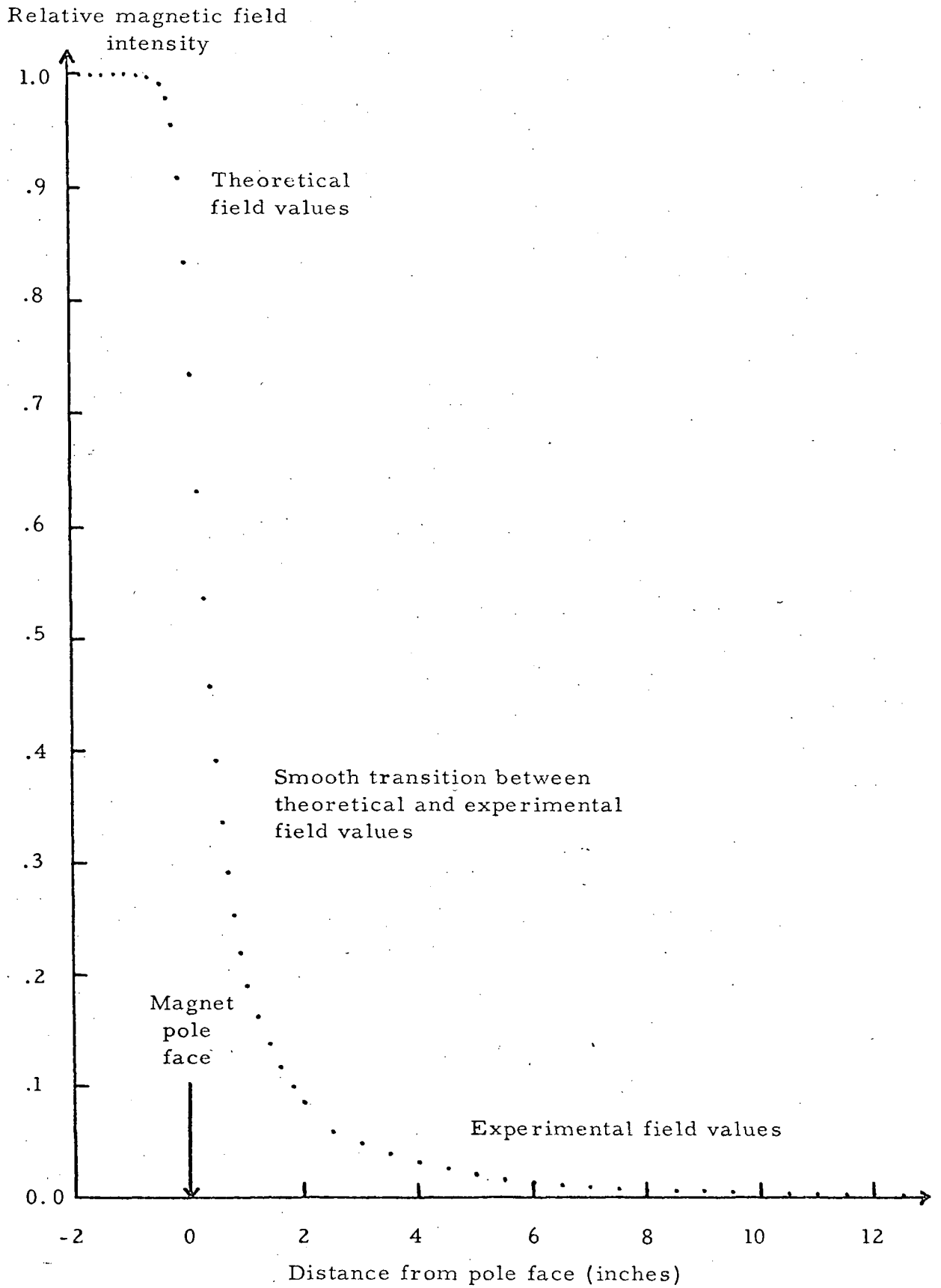


FIGURE II-2. FRINGING FIELD OF MAIN MAGNET

contour for the magnet surface which would give perfect focus at the collector (see Figure II-3). A least squares circle (in the sense of minimizing $\sum_i [\Delta t - \Delta t_i]^2$) was computed through the surface points to determine the best radius associated with ion beams of varying angular divergence α_{\max} (Figure II-4). For values of the angular divergence exceeding 2 deg it is apparent that 7.0 inches is the ideal curvature for the magnet shims. This may be compared with the value of 6.0 inches where the effect of fringing fields is neglected (see Figure II-4).

The magnet shims were designed to have a cylindrical surface of 7.0 inch radius. They were accurately machined from grade 1010 hot rolled carbon steel plate obtained from Dr. Auld of the TRIUMF group at U. B. C. Provision was made for holding the shims rigidly in position on the main magnet pole faces, although adjustment of their position along the pole face was possible.

After mounting the shims the magnet was positioned as shown in Figure II-1. Precise alignment was then achieved experimentally by adjusting the shim position and the vertical position of the magnet to give optimum peak shape. Figure II-5 shows the peak quality obtained for beams of angular divergence 1.9 and 3.0 deg respectively.

Although the resolution was excellent (400-450), the higher angular divergence, coupled with wider source slits, gave rounded

Required reduction in path length (in the magnetic field) to give perfect focus at the collector

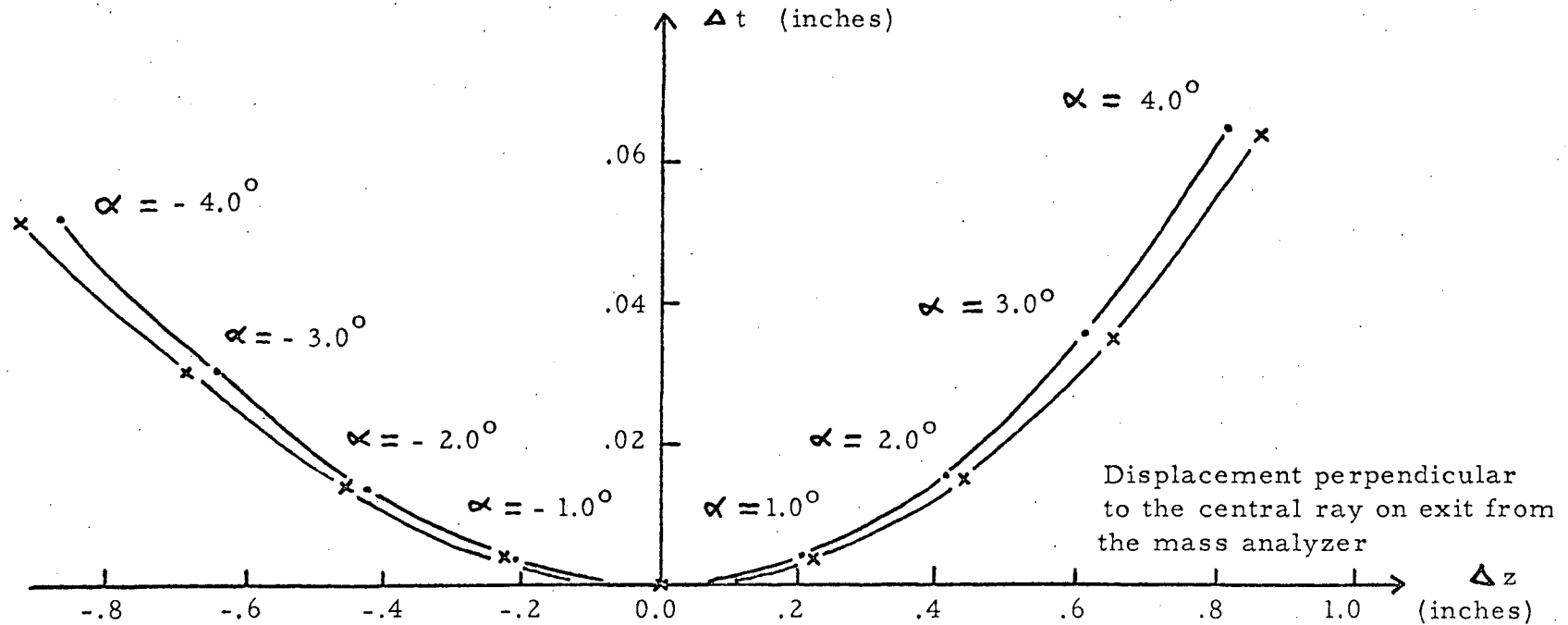


FIGURE II-3. CURVATURE OF SECOND ORDER FOCUSING SHIMS

Ideal curvature of shims assuming (i) no correction for the effect of fringing fields outside the main magnet (represented by dots) or (ii) a correction applied to account for the fringing fields (represented by crosses). Note the different scales used for the two axes. When Δt and Δz are plotted on the same scale the least squares circles fitting the two sets of points have radii of 6.1 and 7.0 inches respectively (using data for $\alpha = 0, \pm .2, \pm .4, \dots \pm 4.0^\circ$).

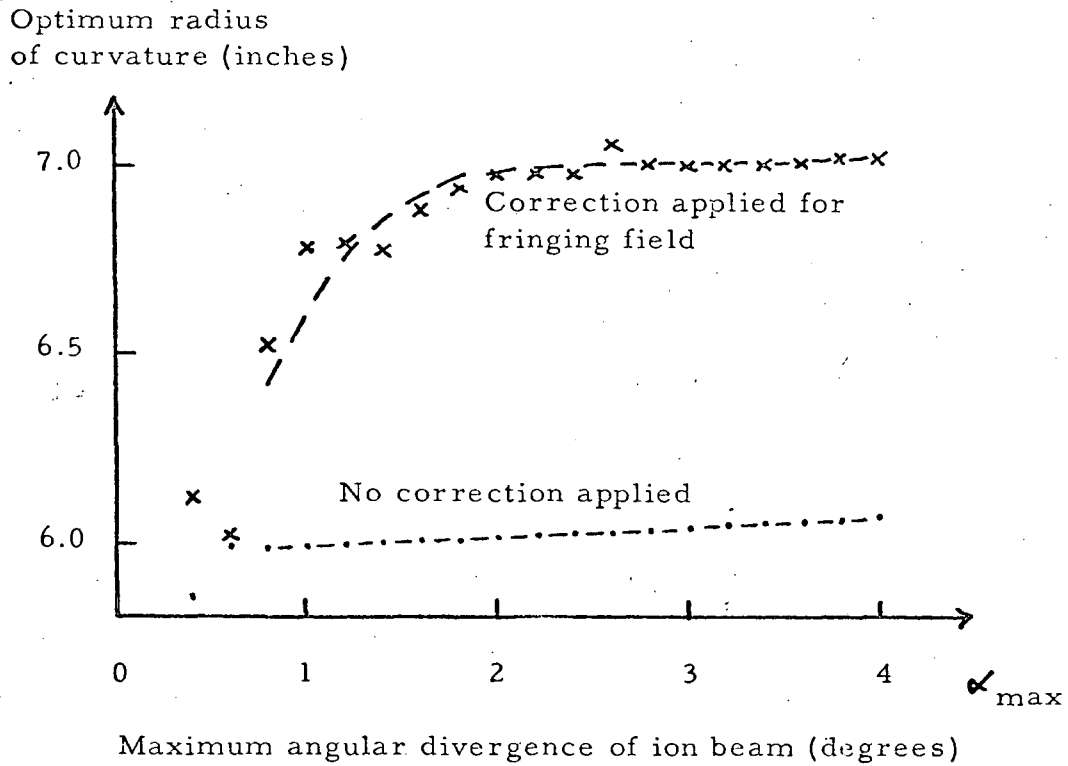
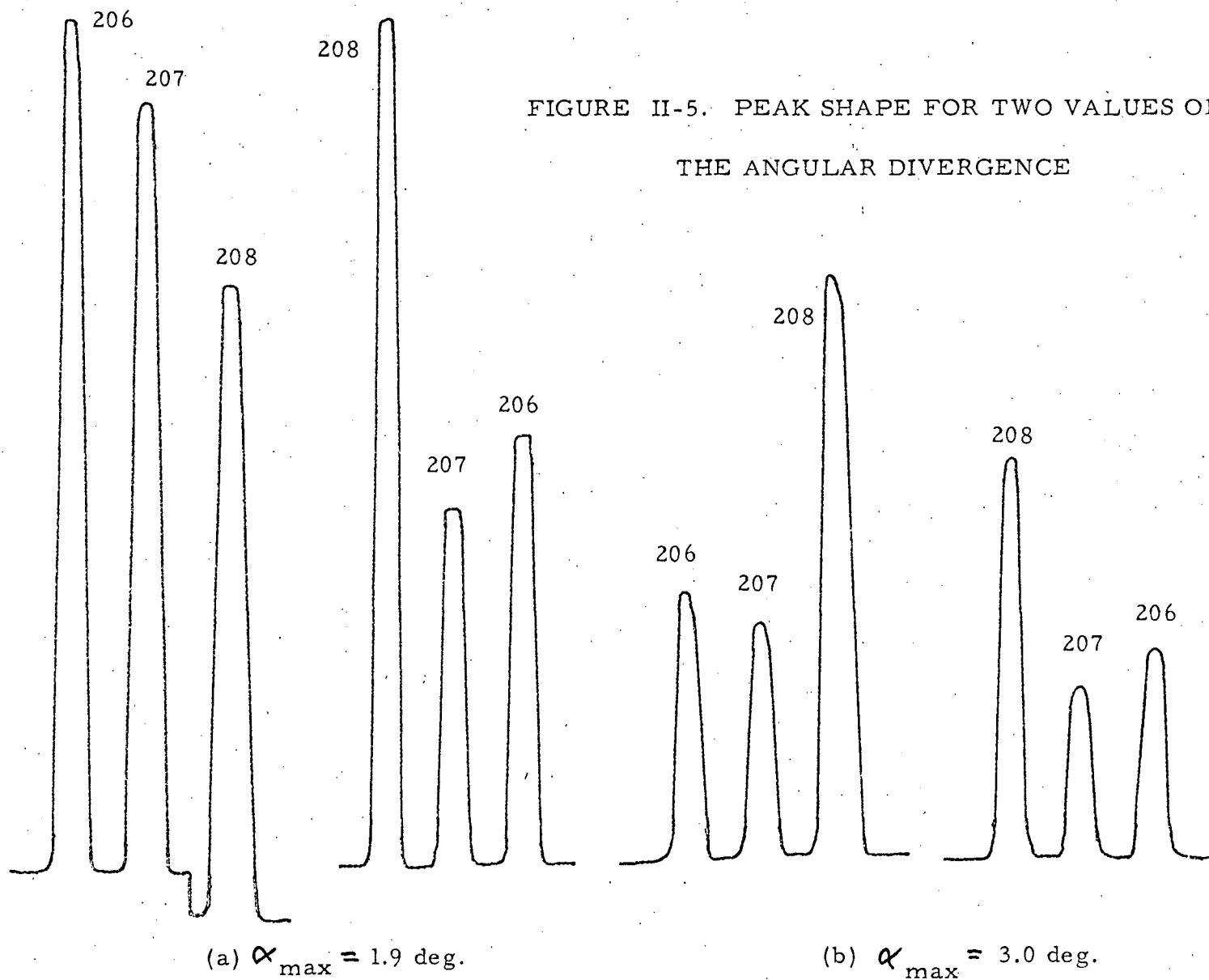


FIGURE II-4. OPTIMUM CURVATURE OF SHIMS AS A FUNCTION
OF BEAM DIVERGENCE

The scatter of the data points is due to truncation errors in the calculations and the use of relatively few trajectories. Each point represents the radius of curvature of the least squares circle fitting through all values of Δt and Δz corresponding to trajectories with initial angles of inclination to the lens axis of $\alpha = 0, \pm 0.2, \pm 0.4, \pm 0.6, \dots, \pm \alpha_{\max}$.

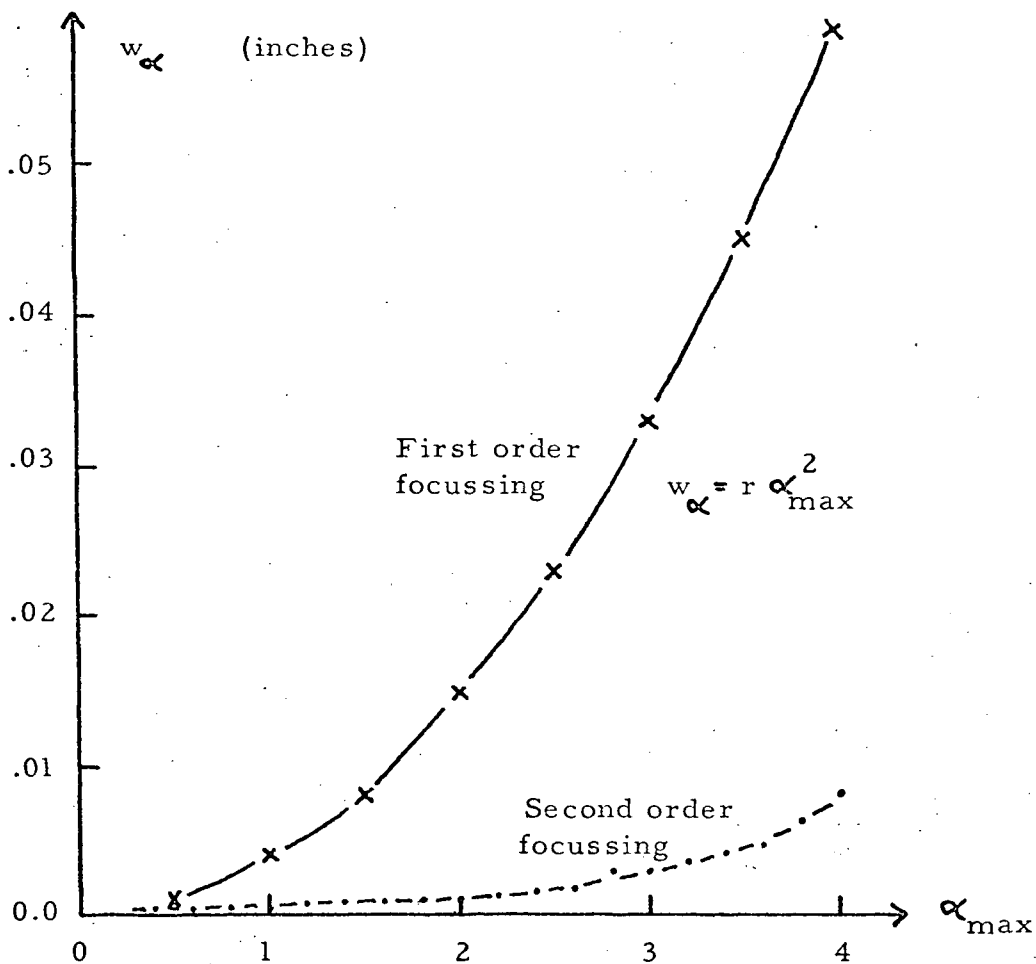


Part of the Pb^+ spectrum is shown for each value of α_{\max} . The second order focussing shims were used to obtain the above spectra.

peak tops and a slight assymetry to the peaks. The lower divergence (corresponding to two 0.010 inch source collimating slits separated by 0.31 inch) was adopted in the present research. This is still a factor of two greater than the divergence used with only first order focussing. The effect of angular divergence on beam width at the collector is shown for first and second order focussing in Figure II-6.

FIGURE II-6. BEAM SPREADING AT THE COLLECTOR FOR
FIRST AND SECOND ORDER FOCUSING

Beam spreading at the
collector due to beam angular
divergence at ion source



Beam divergence at exit slit of ion source (degrees)

The effect of angular divergence (α_{\max}) at the ion source exit slit on the beam width at the collector is shown for both first and second order focussing. The scatter of data points for the case of second order focussing reflects the small number of trajectories used in the calculations ($\alpha = 0, \pm 0.2, \pm 0.4, \dots, \pm \alpha_{\max}$).

APPENDIX III

MEASURED ISOTOPIC RATIOS FOR ALL GADOLINIUM ANALYSES

The experimental values of the isotopic ratios obtained for each set of scans of the Gd^+ (or GdO^+) spectrum are listed in Tables III-1 to III-8. The isotopic ratios Gd^{155}/Gd^{160} , Gd^{157}/Gd^{160} and Gd^{158}/Gd^{160} have all been normalized to $Gd^{156}/Gd^{160} = .9361$ to eliminate the effect of mass discrimination. A correction was made for the isotopic composition of oxygen in all analyses which used the GdO^+ spectrum (Tables III-3, III-4 and III-8). The procedure for making this correction is given in Section 5.5.

The estimated errors in Tables III-1 to III-8 correspond to two standard deviations of the mean. For each set of scans the isotopic ratios and the parameters A and B were computed by the method discussed in Sections 5.3 and 5.4. The weighted mean and its standard deviation were computed for the data in each column of Tables III-1 to III-8 from the equations

$$\mu = \frac{\sum_{i=1,n} \frac{x_i}{\sigma_i^2}}{\sum_{i=1,n} \frac{1}{\sigma_i^2}}$$

$$\sigma_{\mu} = \left\{ \frac{\sum_{i=1,n} \frac{1}{\sigma_i^2} (x_i - \mu)^2}{(n-1) \sum_{i=1,n} \frac{1}{\sigma_i^2}} \right\}^{\frac{1}{2}} \quad (III-1)$$

In these equations, x_i and σ_i represent the mean value of a particular isotopic ratio (or parameter), and the estimated standard deviation of the mean, for set i . These computations were performed using one more significant digit than has been shown in the tables. The entries in the bottom row of each of the Tables III-1 to III-8 are the values of μ and $2\sigma_\mu$ given by equations (III-1). These quantities are the data which appear in Tables 6-1 and 6-2.

TABLE III-1. TRIPLE FILAMENT ANALYSES ON SAMPLE Gd-J

Analysis	Set	No. of scans	$\frac{\text{Gd}^{155}}{\text{Gd}^{160}}$ *	$\frac{\text{Gd}^{157}}{\text{Gd}^{160}}$ *	$\frac{\text{Gd}^{158}}{\text{Gd}^{160}}$ *	A	B
Gd-J1	1	6	.6761 ±.0008	.7161 ±.0009	1.1363 ±.0026	1.3615 ±.0012	1.6916 ±.0038
Gd-J4 #	1	7	.6767 ±.0004	.7162 ±.0003	1.1367 ±.0017	1.3606 ±.0009	1.6922 ±.0034
	2	6	.6764 ±.0007	.7166 ±.0008	1.1358 ±.0014	1.3611 ±.0013	1.6893 ±.0019
	3	6	.6777 ±.0021	.7154 ±.0015	1.1348 ±.0012	1.3586 ±.0042	1.6898 ±.0026
Gd-J5	1	6	.6767 ±.0013	.7161 ±.0010	1.1355 ±.0017	1.3606 ±.0026	1.6898 ±.0032
	2	6	.6769 ±.0002	.7161 ±.0003	1.1364 ±.0005	1.3602 ±.0003	1.6917 ±.0008
	3	6	.6767 ±.0006	.7165 ±.0005	1.1365 ±.0012	1.3606 ±.0013	1.6911 ±.0023
	4	6					1.6902 ±.0010
Average			.67686 ±.00015	.71620 ±.00016	1.13620 ±.00044	1.36030 ±.00027	1.69083 ±.00067

* Fractionation correction corrected to $\text{Gd}^{156}/\text{Gd}^{160} = .9361$

Analyses Gd-J2 and Gd-J3 were rejected because of BaF^+ interference with the Gd^+ spectrum. This was caused by raising the side filament temperature too quickly without allowing sufficient time for Ba to decay at lower temperatures.

The parameters A and B are defined in Table 6-1.

TABLE III-2. TRIPLE FILAMENT ANALYSIS Gd-J6

Analysis	Set	No. of scans	$\frac{\text{Gd}^{155} *}{\text{Gd}^{160}}$	$\frac{\text{Gd}^{157} *}{\text{Gd}^{160}}$	$\frac{\text{Gd}^{158} *}{\text{Gd}^{160}}$	A	B
Gd-J6	1	6	.6782 ±.0011	.7172 ±.0009	1.1361 ±.0004	1.3573 ±.0021	1.6884 ±.0023
	2	5	.6768 ±.0013	.7165 ±.0008	1.1358 ±.0012	1.3603 ±.0025	1.6894 ±.0018
	3	6	.6770 ±.0009	.7165 ±.0006	1.1349 ±.0006	1.3598 ±.0018	1.6873 ±.0024
	4	6	.6758 ±.0011	.7157 ±.0010	1.1356 ±.0007	1.3623 ±.0021	1.6910 ±.0021
	5	6	.6772 ±.0004	.7160 ±.0002	1.1358 ±.0003	1.3596 ±.0008	1.6907 ±.0008
	6	6	.6770 ±.0004	.7159 ±.0004	1.1354 ±.0004	1.3600 ±.0009	1.6899 ±.0010
	7	6	.6769 ±.0003	.7158 ±.0002	1.1355 ±.0006	1.3601 ±.0006	1.6904 ±.0013
	8	6	.6766 ±.0005	.7159 ±.0004	1.1359 ±.0006	1.3608 ±.0010	1.6910 ±.0011
	9	6	.6771 ±.0010	.7156 ±.0006	1.1354 ±.0019	1.3598 ±.0020	1.6906 ±.0029
	10	6	.6763 ±.0004	.7155 ±.0005	1.1355 ±.0005	1.3614 ±.0007	1.6910 ±.0011
Average			.67685 ±.00026	.71593 ±.00014	1.13566 ±.00021	1.36029 ±.00054	1.69038 ±.00054

* Fractionation correction normalized to $\text{Gd}^{156}/\text{Gd}^{160} = .9361$

The parameters A and B are defined in Table 6-1.

Only statistical errors are shown. They correspond to two standard deviations of the mean.

TABLE III-3: SINGLE FILAMENT ANALYSES ON SAMPLE Gd-J

Analysis Set	No. of scans	$\frac{\text{Gd}^{155}}{\text{Gd}^{160}}$ *	$\frac{\text{Gd}^{157}}{\text{Gd}^{160}}$ *	$\frac{\text{Gd}^{158}}{\text{Gd}^{160}}$ *	A	B	
Gd-JS1	1	5	.6770 ±.0008	.7154 ±.0010	1.1343 ±.0018	1.3598 ±.0017	1.6888 ±.0030
Gd-JS2	1	6	.6771 ±.0015	.7158 ±.0006	1.1361 ±.0006	1.3597 ±.0029	1.6915 ±.0013
	2	6	.6767 ±.0010	.7159 ±.0012	1.1359 ±.0008	1.3604 ±.0020	1.6909 ±.0028
Average			.67693 ±.00022	.71575 ±.00029	1.13586 ±.00063	1.36001 ±.00042	1.6910 ±.0013

* Fractionation correction normalized to $\text{Gd}^{156}/\text{Gd}^{160} = .9361$

All analyses were performed using the GdO^+ spectrum. The ratios have been corrected for the isotopic composition of oxygen.

Rhenium having a specified purity of 99.9% was used. Zone-refined rhenium was not used for these two analyses.

The parameters A and B are defined in Table 6-1.

TABLE III-4. SINGLE FILAMENT ANALYSIS Gd-JZ1

Analysis Set	No. of scans	$\frac{\text{Gd}^{155} *}{\text{Gd}^{160}}$	$\frac{\text{Gd}^{157} *}{\text{Gd}^{160}}$	$\frac{\text{Gd}^{158} *}{\text{Gd}^{160}}$	A	B	
Gd-JZ1	1	6	.6774 ±.0005	.7162 ±.0005	1.1351 ±.0015	1.3592 ±.0011	1.6885 ±.0033
	2	6	.6774 ±.0008	.7162 ±.0008	1.1356 ±.0012	1.3592 ±.0016	1.6897 ±.0022
	3	6	.6767 ±.0003	.7153 ±.0007	1.1356 ±.0010	1.3607 ±.0006	1.6917 ±.0024
	4	6	.6768 ±.0012	.7156 ±.0004	1.1360 ±.0008	1.3606 ±.0024	1.6920 ±.0018
	5	5	.6774 ±.0004	.7160 ±.0003	1.1357 ±.0004	1.3593 ±.0007	1.6904 ±.0013
	6	6	.6769 ±.0011	.7162 ±.0007	1.1355 ±.0006	1.3603 ±.0022	1.6895 ±.0020
	7	3	.6772 ±.0010	.7161 ±.0005	1.1361 ±.0018	1.3597 ±.0021	1.6909 ±.0047
	8	5	.6770 ±.0013	.7163 ±.0009	1.1363 ±.0011	1.3601 ±.0026	1.6911 ±.0013
	9	6	.6766 ±.0016	.7150 ±.0010	1.1364 ±.0033	1.3609 ±.0031	1.6942 ±.0079
Average			.67702 ±.00025	.71591 ±.00023	1.13570 ±.00018	1.35999 ±.00050	1.69070 ±.00069

* Fractionation correction normalized to $\text{Gd}^{156}/\text{Gd}^{160} = .9361$

The GdO^+ spectrum was used throughout. The ratios have been corrected for the isotopic composition of oxygen.

High purity zone-refined rhenium was used for this analysis.

The parameters A and B are defined in Table 6-1.

TABLE III-5. TRIPLE FILAMENT ANALYSES ON SAMPLE Gd-US

<u>Analysis</u>	<u>Set</u>	<u>No. of scans</u>	$\frac{\text{Gd}^{155} *}{\text{Gd}^{160}}$	$\frac{\text{Gd}^{157} *}{\text{Gd}^{160}}$	$\frac{\text{Gd}^{158} *}{\text{Gd}^{160}}$	<u>A</u>	<u>B</u>
Gd-US4	1	6	.6764 ±.0009	.7153 ±.0015	1.1347 ±.0011	1.3609 ±.0018	1.6898 ±.0035
	2	8	.6768 ±.0004	.7163 ±.0003	1.1357 ±.0006	1.3603 ±.0007	1.6897 ±.0011
	3	10	.6776 ±.0015	.7160 ±.0009	1.1369 ±.0017	1.3589 ±.0031	1.6931 ±.0028
Gd-US5	1	6	.6768 ±.0003	.7159 ±.0006	1.1363 ±.0004	1.3602 ±.0006	1.6919 ±.0014
Gd-US6	1	6	.6761 ±.0018	.7169 ±.0008	1.1360 ±.0020	1.3618 ±.0036	1.6890 ±.0033
Gd-US7	1	8	.6770 ±.0007	.7176 ±.0007	1.1358 ±.0004	1.3601 ±.0014	1.6868 ±.0019
Average			.67682 ±.00015	.71639 ±.00048	1.13595 ±.00034	1.36026 ±.00027	1.6900 ±.0016

* Fractionation correction normalized to $\text{Gd}^{156}/\text{Gd}^{160} = .9361$

The parameters A and B are defined in Table 6-1.

TABLE III-6. ANALYSIS Eu-AB USING TRIPLE FILAMENTS

Analysis Set	No. of scans	$\frac{\text{Gd}^{155}}{\text{Gd}^{160}}$ *	$\frac{\text{Gd}^{157}}{\text{Gd}^{160}}$ *	$\frac{\text{Gd}^{158}}{\text{Gd}^{160}}$ *	A	B	
Eu-AB	1	6	$.6800^{\#}$ $\pm .0017$	$.7160$ $\pm .0005$	1.1357 $\pm .0013$	$1.3540^{\#}$ $\pm .0034$	1.6903 $\pm .0025$
	2	6	$.6828^{\#}$ $\pm .0010$	$.7162$ $\pm .0010$	1.1362 $\pm .0019$	$1.3486^{\#}$ $\pm .0020$	1.6911 $\pm .0027$
	3	6	$.6816^{\#}$ $\pm .0016$	$.7160$ $\pm .0013$	1.1345 $\pm .0007$	$1.3510^{\#}$ $\pm .0031$	1.6877 $\pm .0041$
	4	6	$.6820^{\#}$ $\pm .0013$	$.7160$ $\pm .0005$	1.1356 $\pm .0005$	$1.3501^{\#}$ $\pm .0026$	1.6901 $\pm .0010$
	5	6	$.6808^{\#}$ $\pm .0008$	$.7161$ $\pm .0007$	1.1361 $\pm .0015$	$1.3525^{\#}$ $\pm .0015$	1.6911 $\pm .0028$
	6	4	$.6808^{\#}$ $\pm .0020$	$.7169$ $\pm .0007$	1.1352 $\pm .0021$	$1.3525^{\#}$ $\pm .0040$	1.6872 $\pm .0052$
	7	6	$.6815^{\#}$ $\pm .0007$	$.7162$ $\pm .0006$	1.1353 $\pm .0005$	$1.3510^{\#}$ $\pm .0014$	1.6892 $\pm .0013$
Average			$.6815^{\#}$ $\pm .0006$	$.71614$ $\pm .00024$	1.13533 $\pm .00035$	$1.3512^{\#}$ $\pm .0012$	1.68987 $\pm .00065$

* Fractionation correction normalized to $\text{Gd}^{156}/\text{Gd}^{160} = .9361$

These ratios show evidence of LaO^+ contamination at mass 155. No correction was possible.

The parameters A and B are defined in Table 6-1.

TABLE III-7. ANALYSIS Gd-AB USING TRIPLE FILAMENTS

Analysis Set	No. of scans	$\frac{\text{Gd}^{155}}{\text{Gd}^{160}}$ *		$\frac{\text{Gd}^{157}}{\text{Gd}^{160}}$ *		$\frac{\text{Gd}^{158}}{\text{Gd}^{160}}$ *		A	B
Gd-AB	1	6	$.6968^{\#}$ $\pm .0078$	$.7160$ $\pm .0005$	1.1355 $\pm .0023$	$1.322^{\#}$ $\pm .015$	1.690 $\pm .005$		
	2	6	$.6867^{\#}$ $\pm .0015$	$.7161$ $\pm .0017$	1.1335 $\pm .0046$	$1.341^{\#}$ $\pm .003$	1.685 $\pm .007$		
	3	6	$.6808^{\#}$ $\pm .0055$	$.7184$ $\pm .0051$	1.1354 $\pm .0083$	$1.352^{\#}$ $\pm .011$	1.684 $\pm .009$		
Average			$.6867^{\#}$ $\pm .0033$	$.71607$ $\pm .00032$	1.1351 $\pm .0011$	$1.341^{\#}$ $\pm .007$	1.6878 $\pm .0036$		

* Fractionation correction normalized to $\text{Gd}^{156}/\text{Gd}^{160} = .9361$

These ratios show evidence of LaO^+ contamination at mass 155. No correction was possible.

The parameters A and B are defined in Table 6-1.

TABLE III-8. ANALYSIS GE-AB USING A ZONE-REFINED
RHENIUM SINGLE FILAMENT

Analysis Set	No. of scans	$\frac{\text{Gd}^{155}}{\text{Gd}^{160}}$ *	$\frac{\text{Gd}^{157}}{\text{Gd}^{160}}$ *	$\frac{\text{Gd}^{158}}{\text{Gd}^{160}}$ *	A	B	
GE-AB	1	6	.6769 ±.0013	.7169 ±.0011	1.1367 ±.0016	1.3601 ±.0026	1.6904 ±.0045
	2	6	.6760 ±.0005	.7161 ±.0007	1.1357 ±.0005	1.3619 ±.0011	1.6900 ±.0019
	3	6	.6766 ±.0006	.7160 ±.0004	1.1351 ±.0005	1.3608 ±.0011	1.6890 ±.0011
	4	6	.6767 ±.0004	.7160 ±.0002	1.1355 ±.0005	1.3606 ±.0009	1.6900 ±.0008
	5	6	.6767 ±.0012	.7160 ±.0004	1.1363 ±.0007	1.3606 ±.0024	1.6918 ±.0017
	6	6	.6766 ±.0010	.7158 ±.0005	1.1352 ±.0010	1.3609 ±.0021	1.6897 ±.0012
	7	6	.6766 ±.0009	.7157 ±.0009	1.1355 ±.0024	1.3608 ±.0018	1.6906 ±.0043
Average			.67652 ±.00024	.71598 ±.00012	1.13557 ±.00031	1.36092 ±.00044	1.68991 ±.00058

* Fractionation correction normalized to $\text{Gd}^{156}/\text{Gd}^{160} = .9361$

All ratios were obtained using the GdO^+ spectrum. The ratios have been corrected for the isotopic composition of oxygen.

The parameters A and B are defined in Table 6-1.

APPENDIX IV

SLOPE OF THEORETICAL CORRELATION LINES FOR NEUTRON
CAPTURE

Let X and Y be the values of the Gd^{157}/Gd^{160} *
and Gd^{158}/Gd^{160} * isotopic ratios when normalized to
 $Gd^{156}/Gd^{160} = .9361$. Then

$$X = \frac{Gd^{157}}{Gd^{160}} \left\{ 1 - .75 \left(\frac{Gd^{156}}{Gd^{160}} - .9361 \right) / \left(\frac{Gd^{156}}{Gd^{160}} \right) \right\}$$

$$Y = \frac{Gd^{158}}{Gd^{160}} \left\{ 1 - .50 \left(\frac{Gd^{156}}{Gd^{160}} - .9361 \right) / \left(\frac{Gd^{156}}{Gd^{160}} \right) \right\} \quad (IV-1)$$

where the isotopic ratios in equations (IV-1) are the measured ratios,
without normalization.

Consideration of the thermal neutron capture processes
leads to the following differential equations

$$\frac{d(Gd^{157}/Gd^{160})}{d(Gd^{158}/Gd^{160})} = -1$$

$$\frac{d(Gd^{156}/Gd^{160})}{d(Gd^{158}/Gd^{160})} = \frac{\sigma_{155}}{\sigma_{157}} \left(\frac{Gd^{155}}{Gd^{157}} \right)$$

(cont. over)

$$\frac{d(\text{Gd}^{155}/\text{Gd}^{160})}{d(\text{Gd}^{158}/\text{Gd}^{160})} = - \frac{\sigma_{155}}{\sigma_{157}} \left(\frac{\text{Gd}^{155}}{\text{Gd}^{157}} \right) \quad (\text{IV-2})$$

From equations (IV-1) and (IV-2) it can be shown that

$$\frac{dY}{dX} = - \frac{\left\{ 1 - .5 \left(\frac{\text{Gd}^{156}}{\text{Gd}^{160}} - .9361 \right) / \frac{\text{Gd}^{156}}{\text{Gd}^{160}} \right\} - .5 \frac{\sigma_{155}}{\sigma_{157}} \left\{ \frac{.9361}{\left(\frac{\text{Gd}^{156}}{\text{Gd}^{160}} \right)} \left(\frac{\text{Gd}^{158}}{\text{Gd}^{157}} \right) \left(\frac{\text{Gd}^{155}}{\text{Gd}^{156}} \right) \right\}}{\left\{ 1 - .75 \left(\frac{\text{Gd}^{156}}{\text{Gd}^{160}} - .9361 \right) / \frac{\text{Gd}^{156}}{\text{Gd}^{160}} \right\} + .75 \frac{\sigma_{155}}{\sigma_{157}} \left\{ \frac{.9361}{\left(\frac{\text{Gd}^{156}}{\text{Gd}^{160}} \right)} \left(\frac{\text{Gd}^{155}}{\text{Gd}^{156}} \right) \right\}} \quad (\text{IV-3})$$

For small changes in isotopic composition we may assume that $\text{Gd}^{156}/\text{Gd}^{160} = .9361$, which greatly simplifies equation (IV-3), and leads to a slope for the correlation line for thermal neutron capture (see Figures 6-1 and 6-3) of $dY/dX = -.763$ near terrestrial Gd (using data from Tables 1-1 and 6-1).

Similarly, the slope of the correlation line for Figures 6-2 and 6-4 is given by

$$\begin{aligned} \frac{dB}{dA} &= \frac{\sigma_{157} B \left\{ 1.5 \left(\frac{\text{Gd}^{157}}{\text{Gd}^{158}} \right) + 1 \right\}}{\sigma_{155} A \left\{ 1.25 \left(\frac{\text{Gd}^{155}}{\text{Gd}^{156}} \right) + 1 \right\}} \\ &= 5.30 \quad (\text{IV-4}) \end{aligned}$$

BIBLIOGRAPHY

- Albee, A. L. , Burnett, D. S. , Chodos, A. A. , Eugster, O. J. , Huneke, J. C. , Papanastassiou, D. A. , Podosek, F. A. , Russ, G. P. , Sanz, H. G. , Tera, F. , and Wasserburg, G. J. (1970). Ages, irradiation history, and chemical composition of lunar rocks from the Sea of Tranquility. *Science* 167, 463-466.
- Anders, E. (1964). Origin, age and composition of meteorites. *Space Sci. Rev.* 3, 583-714.
- Balsiger, H. , Geiss, J. , and Lipschutz, M. E. (1969). Vanadium isotopic composition in meteoritic and terrestrial matter. *Earth Planet. Sci. Lett.* 6, 117-122.
- Barnard, G. P. (1953). Modern Mass Spectrometry, London Institute of Physics.
- Begemann, F. , Geiss, J. , and Hess, D. C. (1957). Radiation age of a meteorite from cosmic-ray-produced He^3 and H^3 . *Phys. Rev.* 107, 540-542.
- Begemann, F. , Eberhardt, P. , and Hess, D. C. (1959). ^3He - ^3H -strahlungsalter eines steinmeteoriten. *Zs. f. Naturforsch.* 14a, 500-503.
- Birch, F. (1964). Density and composition of mantle and core. *J. Geophys. Res.* 69, 4377-4388.
- Burbidge, E. M. , Burbidge, G. R. , Fowler, W. A. , and Hoyle, F. (1957). Synthesis of the elements in the stars. *Rev. Mod. Phys.* 29, 548-650.
- Burnett, D. S. , Fowler, W. A. , and Hoyle, F. (1965). Nucleosynthesis in the early history of the solar system. *Geochim. et Cosmochim. Acta* 29, 1209-1241.
- Burnett, D. S. , Lippolt, H. J. , and Wasserburg, G. J. (1966). The relative isotopic abundance of K^{40} in terrestrial and meteoritic samples. *J. Geophys. Res.* 71, 1249-1269 and 3609.
- Cameron, A. G. W. (1962). The formation of the sun and planets. *Icarus* 1, 13-69.

- Cameron, A. G. W. (1965). Introduction to Space Science, W. N. Hess ed., Gordon and Breach, New York.
- Cameron, A. E., Smith, D. H., and Walker, R. L. (1969). Mass spectrometry of nanogram-size samples of lead. *Anal. Chem.* 41, 525-526.
- Chakraborty, A. K., Stevens, C. M., Rushing, H. C., and Anders, E. (1964). Isotopic composition of silver in iron meteorites. *J. Geophys. Res.* 69, 505-520.
- Chemical Rubber Co. (1970). Handbook of Chemistry and Physics, The Chemical Rubber Co., Cleveland.
- Clarke, W. B., de Laeter, J. R., Schwarcz, H. P., and Shane, K. C. (1970). Aluminum 26-magnesium 26 dating of feldspar in meteorites. *J. Geophys. Res.* 75, 448-462.
- Coggeshall, N. D. (1947). Fringing flux corrections for magnetic focussing devices. *J. Appl. Phys.* 18, 855-861.
- Collins, T. L., Rourke, F. M., and White, F. A. (1956). Mass spectrometric investigation of the rare earth elements for the existence of new stable isotopes. *Phys. Rev.* 101, 196-197.
- Cook, J. L. and Wall, A. L. (1968). The statistical estimation of thermal-neutron cross sections. *Nucl. Sci. Eng.* 31, 234-240.
- Dawson, K. R., Maxwell, J. A. and Parsons, D. E. (1960). A description of the meteorite which fell near Abee, Alberta, Canada. *Geochim. et Cosmochim. Acta* 21, 127-144.
- Eugster, O., Tera, F., and Wasserburg, G. J. (1969). Isotopic analyses of barium in meteorites and in terrestrial samples. *J. Geophys. Res.* 74, 3897-3908.
- Eugster, O., Tera, F., Burnett, D. S., and Wasserburg, G. J. (1970a). Isotopic composition of gadolinium and neutron-capture effects in some meteorites. *J. Geophys. Res.* 75, 2753-2768.
- Eugster, O., Tera, F., Burnett, D. S., and Wasserburg, G. J. (1970b). The isotopic composition of Gd and the neutron capture effects in samples from Apollo 11. *Earth Planet. Sci. Lett.* 8, 20-30.

- Fowler, W. A. , Greenstein, J. L. , and Hoyle, F. (1962). Nucleosynthesis during the early history of the solar system. *Geophys. J. Roy. Astron. Soc.* 6, 148-220.
- Goris, P. (1962). Improved bonding and emission with tantalum surface ionization filaments. ID0-14590, U. S. Atomic Energy Commission Research and Development Report TTD-4500, Ed. 17.
- Hayashi, C. (1966). Evolution of protostars. *Annual Rev. Astron. Astrophys.* 4, 171-192.
- Hoyle, F. , and Wickramasinghe, N. C. (1968). Condensation of the planets. *Nature* 217, 415-418.
- Inghram, M. G. , and Chupka, W. A. (1953). Surface ionization source using multiple filaments. *Rev. Sci. Instr.* 24, 518-520.
- Krankowsky, D., and Muller, O. (1964). Isotopenhaufigkeit und konzentration des lithiums in steinmeteoriten. *Geochim. et Cosmochim. Acta* 28, 1625-1630.
- Krankowsky, D. and Muller, O. (1967). Isotopic composition and abundance of lithium in meteoritic matter. *Geochim. et Cosmochim. Acta* 31, 1833-1842.
- Larimer, J. W. , and Anders, E. (1970). Chemical fractionations in meteorites-III (Major element fractionations in chondrites). *Geochim. et Cosmochim. Acta* 34, 367-387.
- Loveless, A. J. (1967). Ion trajectories in mass spectrometer ion sources. Unpublished M. Sc. thesis, University of Toronto.
- Loveless, A. J. , and Russell, R. D. (1969). A strong-focussing lens for mass spectrometer ion sources. *Int. J. Mass Spectrom. Ion Phys.* 3, 257-266.
- Lugmair, G. W. (1970). Neutron capture effects in lunar material. A paper presented at the eighteenth Annual Conference on Mass Spectrometry and Allied Topics in San Francisco.
- Mason, B. (1962). Meteorites , John Wiley and Sons, New York.

- Mason, B. (1963). Olivine composition in meteorites. *Geochim. et Cosmochim. Acta* 27, 1011-1023.
- Merrihue, C. M. (1963). Excess xenon 129 in chondrules from the Bruderheim meteorite. *J. Geophys. Res.* 68, 325-330.
- Millman, P. M. (1953). A catalogue of Canadian meteorites. *R. A. S. C. Jour.* 47, 29-33.
- Miyashiro, A. (1968). Effect of the high-luminosity stage of the protosun on the composition of planets and meteorites. *Chemie der Erde* 27, 252-259.
- Miyashiro, A. (1967). Origin of planets and meteorites. *Kagaku* 37, 520-527.
- Murthy, V. R. (1960). Isotopic composition of silver in an iron meteorite. *Phys. Rev. Letters* 5, 539-540.
- Murthy, V. R. (1962). Isotopic anomalies of molybdenum in some iron meteorites. *J. Geophys. Res.* 67, 905-907.
- Murthy, V. R., and Schmitt, R. A. (1963). Isotopic abundances of rare-earth elements in meteorites. *J. Geophys. Res.* 68, 911-917.
- Murthy, V. R., Schmitt, R. A., and Rey, P. (1970). Rubidium-strontium age and elemental and isotopic abundances of some trace elements in lunar samples. *Science* 167, 476-479.
- Ozard, J. M., and Russell, R. D. (1970). Discrimination in solid source lead isotope abundance measurement. *Earth Planet. Sci. Lett.* 8, 331-336.
- Reynolds, J. H. (1963). Xenology. *J. Geophys. Res.* 68, 2939-2956.
- Ringwood, A. E. (1966). Chemical evolution of the terrestrial planets. *Geochim. et Cosmochim. Acta* 30, 41-104.
- Umemoto, S. (1962). Isotopic composition of barium and cerium in stone meteorites. *J. Geophys. Res.* 67, 375-379.
- Wood, J. A. (1968). Meteorites and the Origin of Planets, McGraw-Hill Inc., New York.